

Ultra-high voltage, low power and energy recovering electronics for dielectric elastomer actuators

Présentée le 18 août 2022

Faculté des sciences et techniques de l'ingénieur
Laboratoire d'actionneurs intégrés
Programme doctoral en robotique, contrôle et systèmes intelligents

pour l'obtention du grade de Docteur ès Sciences

par

Raphaël Johannes Charles MOTTET

Acceptée sur proposition du jury

Prof. K. Aminian, président du jury
Prof. Y. Perriard, Dr A. Boegli, directeurs de thèse
Prof. C. Giraud-Audine, rapporteur
Prof. A. Sylvestre, rapporteur
Prof. K. Choo, rapporteur

"At some point, everything's gonna go south on you and you're going to say:
This is it. This is how I end...
Now you can either accept that, or you can get to work.
That's all it is. You just begin. You do the math.
You solve one problem and you solve the next one, and then the next.
And If you solve enough problems, you get to come home."
— *Mark Watney*

"Il faut agir aussi vite que possible, mais aussi lentement que nécessaire."
— *Alain Berset*

À la mémoire de mon père...

Remerciements

Bien qu'un seul nom ne soit crédité comme auteur de cette thèse, le travail présenté ici n'aurait pas été possible sans l'implication de nombreuses personnes auxquelles je tiens, au travers de ces quelques lignes, à exprimer ma reconnaissance.

Tout d'abord, je souhaiterais vivement remercier Yves qui, au détour d'un repas partagé en Chine lors de mon projet de master à Shanghai, m'avait pour la première fois proposé d'entreprendre une thèse de doctorat dans son laboratoire. Offre que je ne regrette absolument pas d'avoir accepté. De plus, sa confiance et son leadership furent inestimables et indispensables à la réussite de ce projet.

Je suis également très reconnaissant du soutien apporté par Alexis, mon co-directeur, tout au long de cette thèse au travers de nombreuses discussions et partages de connaissances, mais aussi de sa patience et du temps qu'il a consacré à relire mes travaux auxquels il a toujours su apporter des commentaires pertinents.

Je tiens aussi à remercier les professeurs Aminian, Choo, Giraud-Audine et Sylvestre d'avoir accepté de faire partie de mon jury de thèse ainsi que d'avoir donné de leur temps pour relire et évaluer mon travail.

Un grand merci aussi aux autres membres du CAM et du LAI, passés et présents. En particulier à Morgan qui, grâce à sa pédagogie inégalable, son écoute et ses conseils, a su, tôt, me mettre sur les bons rails que je suivis jusqu'à la fin. À Yoan pour son management exemplaire du CAM ainsi que son soutien et confiance en toute l'équipe. À Paolo pour sa disponibilité à aider quel que soit le projet mais surtout pour sa gestion sans égale de l'inventaire sans laquelle tout ne serait que chaos. À Thomas qui su être une oreille attentive et de bon conseil lorsque je faisais face aux nombreux problèmes liés à mon électronique. À Sean, Camilo, Adrien et Pato: la OG team présente la majeure partie de ma thèse et qui à toujours été là pour célébrer les réussites comme pour soutenir dans les coups durs. Mais le reste des doctorants, post-doc et permanents du LAI et du CAM ont, bien entendu, aussi été des éléments essentiels à la création de l'ambiance géniale du labo pendant ces quatre ans et demi de thèse : Aline, Amine, Armando, Bhawnath, Christian, Florian, Francesco, Guillaume, Guzman, Jasha, Kenny, Louis, Marjane, Ning, Pooneh, Quentin, Silje, Simon, Sofia, Stefania, Trung, Xiaotao et Xinchang. Finalement, un grand merci à ma famille et à mes amis. En particulier à ma mère pour son soutien inébranlable et grâce à qui mes parcours académique et de vie ont été possible; à Magali, mon amour, pour son soutien et sa loyauté à toute épreuve pendant ces 10 années passées ensemble; et à toute l'équipe de la G&B pour toutes ces années d'amitié :) .

Neuchâtel, July 20, 2022

Raphaël Mottet

Abstract

Heart failure is a cardiovascular disease affecting between 1 and 2 % of the population of developed countries alone – more than 10 million people – with this number bound to increase due to the ageing of the population. This condition starts to develop itself when the heart is not capable to properly pump the blood in the circulatory system anymore, and it can be due to other cardiovascular diseases, hypertension, heart attacks, etc. When cases become very severe, surgical procedures are then necessary to install cardiac assist devices to help reduce the stress experienced by the heart and allow it to potentially heal itself. However, the devices currently used are bulky and very invasive with risks of infections and rejections.

As such, EPFL's Center for Artificial Muscles (CAM) was tasked to investigate and develop a new kind of cardiac assist devices which would be much less invasive to install. To do so, the idea envisioned consisted of working with Dielectric Elastomer Actuators (DEAs) which are often nicknamed artificial muscles due to their close resemblance with the natural ones as they are, amongst other things, light, thin and can deform themselves significantly. One of the main challenges of working with this technology, however, comes from the fact that DEAs have very uncommon needs concerning the driving electronics. Indeed, to operate to the maximum of their abilities, DEAs require voltages of several thousands of volts – between 5 and 20 kV depending on the actuator – to be applied to them.

Currently, these actuators are powered using extremely large and impractical laboratory power supplies which is unacceptable for portable and medical applications. It was therefore critical to investigate and uncover a solution for the electronics so that the DEAs' needs could be met with a system as compact and efficient as possible.

Thus, this thesis presents the investigating process followed to obtain in the end an electronics system capable of supplying at least 8 kV to a DEA and recover unused electrical energy stored in the actuator. Process which consists at first of an investigation of power electronics topologies capable of amplifying a given input voltage to a higher level in order to determine the most suitable one. It concludes that the DC/DC flyback converter was the best candidate for the job.

This is followed by an in-depth analysis of the working principle of this converter topology to determine the limiting factors regarding the supply of high voltages. This analysis is confirmed through the development of an analytical model depicting the behavior of the converter when it charges the actuator to the required voltage. Thanks to this, a list of solutions to overcome

Abstract

these factors could be given.

Then, due to the voltage levels worked with and the necessity to recover the unused electrical energy stored in the actuator, it was revealed that commercially available solutions were scarce to nonexistent to properly control the electronics. As such, control strategies and custom devices conceived to resolve this problem are presented.

In the end, the final ultra-high voltage bidirectional flyback converter prototype is used to operate a DEA pump placed in a test bench recreating the pressure conditions and blood flow which are expected to be found in a living body. These tests show that the electronics performs very well and manages to operate without major issues the new cardiac assist device created by the CAM.

Keywords: Cardiac Assist Device, Artificial Muscles, Dielectric Elastomer Actuators, High Voltage, Flyback Converter, Energy Recovery, Parasitic Elements, Pulsed Transformer Gate Drive Topology

Résumé

L'insuffisance cardiaque est une maladie cardiovasculaire affectant entre 1 et 2 % de la population rien que dans les pays développés – soit plus de 10 millions de personnes – avec une inexorable tendance à augmenter avec le vieillissement de la population. Cet état de santé se développe lorsque le coeur n'est plus capable de pomper le sang avec suffisamment de force dans le système sanguin. Cette situation peut être due à plusieurs facteurs tels que d'autres maladies cardiovasculaires, de l'hypertension, des arrêts cardiaques, etc. Lorsqu'un cas devient particulièrement sévère, il est alors nécessaire de procéder à un traitement chirurgical pour installer un dispositif d'assistance cardiaque pour réduire le stress éprouvé par le coeur de façon à ce qu'il puisse tenter de se guérir. Cependant, les dispositifs utilisés actuellement sont encombrants et très invasifs avec des risques d'infections et de rejets.

C'est pour cela que le Centre du Muscle Artificiel (CAM) de l'EPFL s'est donné pour tâche de trouver et de développer un nouveau type de dispositif d'assistance cardiaque qui serait beaucoup moins invasif à installer. Pour cela, la décision a été prise d'utiliser des Actionneurs à Élastomère Diélectrique (DEA). Ces derniers sont fréquemment surnommés muscles artificiels en raison de leur grande ressemblance avec leurs versions naturelles, car ils sont, entre autres, légers, fins et capables de beaucoup se déformer. Un des principaux défis, quand il s'agit de travailler avec cette technologie, est que les DEA ont des besoins très particuliers en ce qui concerne l'électronique devant les piloter. En effet, pour qu'ils fonctionnent au meilleur de leurs capacités, les DEA ont besoin de sources de tension capables de fournir entre 5 et 20 kV selon l'actionneur.

Actuellement, ces actionneurs sont alimentés par des sources de laboratoire particulièrement grandes et encombrantes, ce qui est inacceptable pour une application médicale devant être portable et compacte. Il était alors critique d'enquêter sur une possible solution qui soit capable de satisfaire les besoins des DEA tout en étant aussi compacte et efficiente que possible.

Cette thèse présente le processus d'investigation qui a, au final, mené à la conception d'une électronique capable de fournir une tension d'au moins 8 kV à un DEA tout en récupérant l'énergie électrique inutilisée et stockée dans l'actionneur. Un processus qui a, en premier lieu, consisté à étudier les topologies d'électronique de puissance capables d'amplifier une quelconque tension d'entrée vers un plus haut niveau. Cela dans le but de déterminer la plus à même de répondre aux besoins de l'actionneur. Il a été conclu que la topologie de convertisseur DC/DC de type flyback était la meilleure candidate.

Il en suit une analyse détaillée du principe de fonctionnement de cette topologie pour déterminer les facteurs limitant sa capacité à amplifier une tension aux niveaux désirés. Cette analyse est confirmée par un modèle analytique décrivant le comportement du convertisseur lorsque celui-ci charge l'actionneur à la tension souhaitée. Grâce à cela, une liste de solutions pouvant aider à outrepasser ces limites a pu être dressée.

Ensuite, les niveaux de tension manipulés couplés à la nécessité de récupérer l'énergie inutilisée et stockée dans l'actionneur ont pour conséquence que des solutions préexistantes pour contrôler cette électronique sont rares, voire inexistantes. Ainsi, des stratégies de contrôle et des composants sur mesure ont été conçus pour résoudre ce problème.

Finalement, un prototype de convertisseur flyback bidirectionnelle à ultra-haute tension est utilisé pour piloter une pompe DEA placée dans un banc de test recréant les conditions de pression et de flux sanguin que trouve dans un corps humain. Ces tests ont montré que l'électronique fonctionne bien et qu'elle est capable de piloter sans trop de difficultés le nouveau dispositif d'assistance cardiaque du CAM.

Mots-clés : Dispositif d'Assistance Cardiaque, Muscles Artificiels, Actionneur à Élastomère Diélectrique, Haute Tension, Convertisseur Flyback, Récupération d'Énergie, Éléments Parasites, Commande de Grille de Transformateur d'Impulsion

Contents

Remerciements	i
Abstract (English/Français)	iii
1 Introduction	1
1.1 Context	1
1.2 Thesis goals	3
1.3 Thesis outline	4
2 State of the art	7
2.1 Introduction	7
2.2 Dielectric elastomer actuators	7
2.2.1 Manufacture of a DEA	7
2.2.2 Capacitive nature and energy recovery	8
2.2.3 High voltages	9
2.2.4 Design requirements summary	10
2.3 High voltage power electronics	11
2.3.1 Amplifiers	11
2.3.2 Charge pumps	12
2.3.3 Voltage multipliers	13
2.3.4 Marx generators and series-parallel topologies	14
2.3.5 Transformer topologies	15
2.3.6 Switch-mode power supplies	16
2.4 Conclusion	19
3 Ultra-high voltage generation with a flyback DC/DC converter	21
3.1 Introduction	21
3.2 Working principle	21
3.3 Charge phase	23
3.3.1 Intrinsic voltage limitation due to parasitic elements	24
3.3.2 Flyback model with parasitic elements	26
3.3.3 Influence of capacitive parasitic elements	27
3.3.4 Simulations	29
3.4 Design considerations to improve high voltage capabilities	31

Contents

3.4.1	Reduction of the parasitic capacitances of the coupled inductor	31
3.4.2	Coupled inductor cores	33
3.4.3	Upgraded coupled inductor	35
3.4.4	Secondary diode	36
3.5	Experimental results	36
3.5.1	General measurements	37
3.5.2	Energy calculation procedure	39
3.5.3	Efficiency estimation	42
3.6	Conclusion	43
4	Analytical model of the charge phase	45
4.1	Introduction	45
4.2	Model schematic and procedure	45
4.3	Step 1 - Primary current	47
4.3.1	Analytical solution	47
4.4	Step 2 - Secondary current	48
4.4.1	Analytical solution	49
4.5	Step 3 - Reverse output current	49
4.5.1	Analytical solution	50
4.6	Step 4 - Induced primary current	51
4.6.1	Analytical solution	52
4.7	Comparison with measurements	53
4.7.1	Estimation of the maximum output voltage reachable	54
4.8	Conclusion	55
5	High voltage manipulation and energy recovery	57
5.1	Introduction	57
5.2	Integrated ultra-high impedance high voltage probe	57
5.2.1	Voltage divider design considerations	58
5.3	Pulsed transformer gate drive switch	61
5.3.1	Working principle	63
5.3.2	The 13.5 kV switch	64
5.3.3	PTGD switch upgrades	65
5.4	Discharge control strategies	66
5.4.1	ADC-based control strategy	67
5.4.2	Schmitt trigger-based control strategy	71
5.4.3	Pros and cons	74
5.5	Experimental results	75
5.5.1	General measurements	76
5.5.2	Energy calculation procedure	77
5.5.3	Efficiency estimation	79
5.6	Conclusion	81

6	Bidirectional flyback converter with dielectric elastomer actuators	83
6.1	Introduction	83
6.2	Large and variable access resistance capacitive loads	83
6.3	Pressurized DEA tubes	88
6.4	DEA tubes under dynamic pressure	90
6.5	Conclusion	95
7	Conclusion, contributions & outlook	97
7.1	Conclusion	97
7.2	Contributions	99
7.3	Outlook	100
A	Bill of materials	103
B	Electronics schematics	107
C	Exploded view of the flyback converter	113
	Bibliography	115
	Curriculum Vitae	

1 Introduction

1.1 Context

Cardiovascular diseases (CVDs) are the leading cause of death globally according to the World Health Organization (WHO) [1] with more than 18 million people losing their lives in 2019 and close to 49 million people living with CVDs in Europe alone. CVD is an umbrella term for several disorders linked to the heart and the blood vessels around it. Disorders such as the coronary heart disease which is due to a reduction of the blood supplied to the heart from its arteries; the congenital heart disease which is due to birth defects affecting the normal development of the heart; and heart failure (HF) which is caused by an inability of the heart to properly pump to support the blood flow throughout the body, to list a few. The latter of which is estimated to affect between 1 to 2 % of the population – or more than 10 million people – in developed countries and is set to increase with the ageing of the population [2].

Heart failure starts to develop itself when the heart becomes either unable to properly fill back up with enough blood (diastolic heart failure) or unable to pump hard enough to eject all of the blood from the ventricle into the circulatory system (systolic heart failure). HF can be the result of other CVDs, hypertension, heart attacks, etc. This pathology can lead to a wide range of consequences from mild discomforts like shortness of breath or fatigue to more severe symptoms like fluid build-up throughout the body or blood accumulation in the lungs or eventually to the death of the patient as it has an overall tendency to worsen if left untreated.

While a large portion of heart failure cases can be managed and treated through medical and lifestyle changes when detected early. When cases evolve and become more severe ventricular assist devices (VADs) can be considered while on some rare occasions for end stage heart failures a full heart transplant is the only remaining option. However, these two treatments remain absolute last resorts because VADs require complex operation procedures and are extremely invasive, whereas heart transplants require adequate donors which are scarcely available, and both are not immune to complications further down the line with infections and rejections.

Introduction

Currently the most common VADs generally consist of bulky systems implanted into the body with tubes directly connected to the heart through holes cut into the problematic ventricle as shown in Fig. 1.1 and with a laminar blood flow – as opposed to the natural pulsatile flow – generated by a pump composed of a propeller rotating directly in the bloodstream [4]. This direct contact with the blood can often lead to bleeding, blood clotting or hemolysis (the destruction of red cells). Meaning that the patient is dependent of medication such as anticoagulants for the entire duration of the device's use [5]. In addition to that, the system is powered via wires going through the skin which can lead to more infections and general discomforts to the patient.

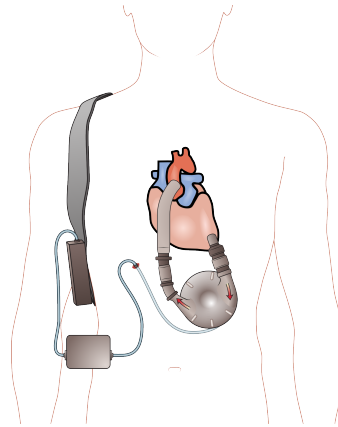


Figure 1.1: Example of a conventional Ventricular Assist Device placed in a human body [3].

It is with the shortcomings of current VADs in mind that the Center for Artificial Muscles (CAM) was opened and tasked to investigate potential solutions to improve upon the existing systems. It was decided that the new generation of heart pumps designed within the CAM would be centered around Dielectric Elastomer Actuators (DEAs) because of numerous advantages discussed in more details in Chapter 2 but mainly due to their close resemblance to natural muscles.

The idea that is devised for the CAM heart pump consists of a tubular DEA which will be placed around the aorta as shown in Fig. 1.2 to use the aortic counterpulsation (ACP) principle. Meaning that the actuator will be operated in such a way that it will alternatively expand and contract itself in sync with the beats of the heart. Indeed, by making sure that it contracts itself when the aortic valve is closed, the blood in the aorta can be pushed farther into the circulatory system which will, consequently, help reduce the pressures sensed by the heart by several percents and increase the coronary flow [6]. These physical improvements have the potential to help stop the progression of heart failures or even lead to the healing of the heart [7].

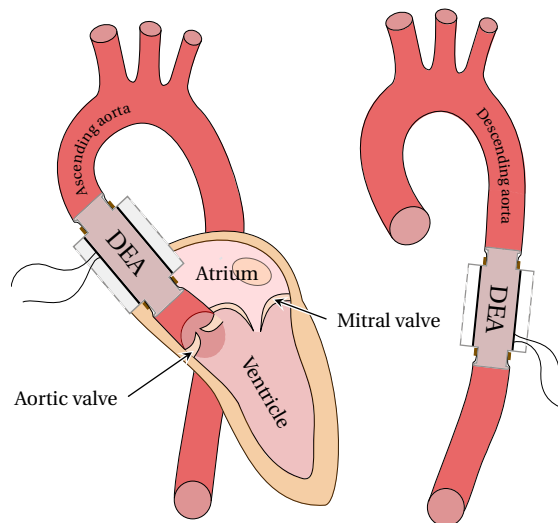


Figure 1.2: The DEA heart pump is destined to be placed after the heart either around the ascending aorta or the descending aorta.

1.2 Thesis goals

Whenever dielectric elastomer actuators are talked about, the discussion is most often centered around their mechanical characteristics and the overall performances regarding deformations, displacements, etc. that they can achieve which are obviously critical aspects to investigate for the systems they are destined to be used with. Unfortunately, this is generally done to the detriment of the electronics necessary to drive them which is often left aside as an afterthought. Indeed, many brilliant projects promise to make good use of the advantageous characteristics of DEAs such as their lightness, compactness and high flexibility in applications where the final product must be compact, portable and efficient. However, when one starts to look towards the electronics used to operate them, one will often notice that very large, heavy and generally impractical laboratory devices are used.

This is due to two main reasons. First, this technology is quite young as it only started to be seriously studied in the early 2000s beginning with the works of Pelrine [8][9] and its popularity significantly grew over the past decade. And, second, it is due to the fact that DEAs have very particular and challenging needs for them to operate at the maximum of their abilities. As discussed in more details in the next chapter, more than just having a small size not to spoil the DEAs' advantages of portability and compactness, the electronics must be capable to quickly supply extremely high voltages in the order of several thousands of volts to the actuators (between 5 kV to 20 kV depending on the actuator). In addition to that, it must also be capable to bring the voltage back down to 0 V, ideally as efficiently as possible which is rarely the case with current devices. Indeed, the most common way to bring this voltage down consists of dissipating energy through resistive elements in the form of heat thus greatly reducing the overall efficiency of the system.

As such, dedicated electronics systems have only recently started to be investigated and developed for DEA-based applications. This shows that there are opportunities for studies to take place within the field of power electronics aimed at dielectric elastomer actuators.

The goals of this thesis are thus to explore the current state of power electronics with an eye towards high voltage amplification to determine which topologies have the highest potential to answer DEAs' needs; to study the behavior of these actuators from an electronics' point of view to better understand their needs and define what kind of limitations they impose on the electronics; to lay the groundwork for optimization processes to take place in the future to further miniaturize the driving system and open the door for opportunities to make it more efficient; to investigate solutions to work with and manipulate the high voltages generated so that DEAs can be safely and reliably operated; and ultimately to show that a dedicated electronics tailored to the application and made as compact as possible can operate DEAs in the most challenging conditions.

1.3 Thesis outline

The way these goals were achieved is presented within this thesis according to the following structure.

CHAPTER 2: State of the art

This chapter provides a more detailed presentation of dielectric elastomer actuators to understand the needs and limitations of the technology in order to choose the most suitable electronics topology to power them. To do so, a brief description of the manufacturing process of DEAs is first given as it explains some of the electrical characteristics of this type of load – e.g. its capacitive nature – which will lead to the first selection criterion. As for the second criterion, it is obtained through the investigation of the working principle of DEAs which indicates the voltage levels required for them to operate to the best of their abilities.

With these two criteria defined, an in-depth review of power electronics topologies is presented in which all possible solutions even remotely capable to amplify an input voltage to a higher level are considered. Through this process it is revealed that several candidates have a great potential to power DEAs with respective pros and cons. However, the most suitable topology – the flyback converter – was ultimately selected.

CHAPTER 3: Ultra-high voltage generation with a flyback DC/DC converter

With the topology selected, its working principle is explained in great details in this chapter. By doing so, the critical design parameters and factors limiting the amplification of the voltage are revealed. Several strategies and design considerations are then proposed to maximize the performances of the electronics, and are subsequently implemented.

Ultimately, the manufactured electronics combining all those elements is thoroughly tested and its performance is evaluated through an energy efficiency analysis. Analysis which revealed new parameters and design aspects worth investigating further for later iterations of the electronics.

CHAPTER 4: Analytical model of the charge phase

In Chapter 4, the mathematical development followed to obtain the analytical model of the electronics is detailed. This model describes the behavior of the currents flowing throughout the flyback converter during the phase when the voltage increases across a capacitive load. From this model, several pieces of information are deduced such as the maximum theoretical output voltage a given converter is capable to reach, and the confirmation of an earlier assumption that parasitic capacitive elements found in the converter are the main limiting factors regarding the output voltage increase.

CHAPTER 5: High voltage manipulation and energy recovery

Due to their capacitive nature, DEAs end up storing a lot of electrical energy when fully charged and deformed. Thus, in order to have the highest overall efficiency possible, it is critical to investigate solutions to recover this stored energy when the time comes to bring the actuator back to its original shape. Thankfully, the flyback converter can easily be modified to work bidirectionally so that the energy can flow from the power supply towards the load and back to the power supply.

However, because of the voltage levels that must be manipulated, there are currently no already made solutions available especially regarding adequate high voltage switches. As such, this chapter presents the investigation process leading to the enabling of the bidirectional capabilities of the ultra-high voltage flyback converter. Indeed, by implementing the pulsed transformer drive topology, several high voltage MOSFETs could be put in series to spread the voltage stress between them. In addition to that, several control strategies are studied in order to safely and reliably drive the discharging of the load.

In the end, an efficiency analysis is also conducted to evaluate the performances of the flyback converter during this discharge phase. It reveals that while the solution consisting of MOSFETs put in series works well, it is the source of a significant amount of losses which will require further development to reduce them.

CHAPTER 6: Bidirectional flyback converter with dielectric elastomer actuators

In this chapter, the ultra-high voltage flyback converter is put to the ultimate test by gradually pushing it to its limits. Indeed, here, the converter is used to power DEA tubes which are themselves put in increasingly challenging environments.

The first series of experiments simply consist of supplying power to DEAs. It was a critical step as it showcased peculiar behaviors of DEAs when faced with the impulsive nature of the currents generated by the flyback converter. Behaviors which had a high potential of fatally damaging the tubes themselves and the electronics but which was ultimately managed through the implementation of a clever and simple solution.

For the second series of experiments, an actuator is put under constant pressure thanks to a custom-made water column test bench in order to simulate the pressures a DEA pump is expected to experience inside a living body. This pressure is gradually increased to study the effects of this parameter on the tube and the electronics.

And in the last experiments, the DEA tube is implemented in a *flow-loop* test bench which is designed to accurately model the circulatory system of the human body using water, a series of pressure chambers, valves, and a pump pushing the water around. Thanks to this system the dynamic pressure and flow changes of the blood can be simulated. In the end, this experiment proves that the electronics is capable to supply the voltages necessary to operate the DEA

Introduction

pump. As an added bonus, it even shows that this pump is capable to reduce the pressure in the circulatory system as hoped.

CHAPTER 7: Conclusion, contributions & outlook

Finally, this chapter concludes this thesis by highlighting the main achievements realized as well as the resulting contributions. Additionally, the outlook for further investigations and studies is presented and described.

2 State of the art

2.1 Introduction

The purpose of this chapter is twofold. First, it is to present in detail the actuator that we wish to operate to show some of the challenges of the particular technology used and to subsequently define the design specifications for the driving electronics. And second, with these specifications in mind, it is to give a list of potential solutions and present the selection process that led to the choice of the topology studied throughout this thesis.

2.2 Dielectric elastomer actuators

The actuator used belongs to the family of Dielectric Elastomer Actuators (DEAs). The popularity of these types of actuators has been steadily growing over the past few decades due to their extremely advantageous characteristics such as lightness, compactness, flexibility, and large deformations which can reach 100 % when DEAs are pre-stretched [9–11].

The range of applications for DEAs is virtually endless; researchers have managed to use them in pick-and-place robots with soft grippers to manipulate delicate objects [12], in wind turbines to control the flaps along their wings [13], in soft pumps [14], and obviously in biomedical applications due to their close resemblance to biological tissues [15].

2.2.1 Manufacture of a DEA

In their most basic form, DEAs are made out of a flexible dielectric layer sandwiched between two compliant electrodes. For the former, it is common to use sheets of silicone of various thicknesses that are available in the market. For our application, *Wacker's* 100 μm Elastosil® 2030 sheets [16] were used. As for the electrodes, they consist of a carbon powder mixed with liquid silicone to form a so-called carbon ink which is then spread on both sides of the dielectric layer as shown in Fig. 2.1 below.

However, regarding the actuator built in the Center for Artificial Muscles (CAM) and ultimately used as part of this thesis, the process is slightly more complicated as it involves a few more steps: several silicone sheets on each of which only a single electrode was deposited (also called modules) are glued on each other as depicted in Fig. 2.2. The resulting stack is then rolled into a tube such as the one presented in Fig. 2.3. This stacking process allows this new DEA to provide more force to its environment. In addition to that, to facilitate the flow of electrical charges in the electrodes and to connect the device to the electronics, access lines made out of a silver ink are integrated into the electrodes.

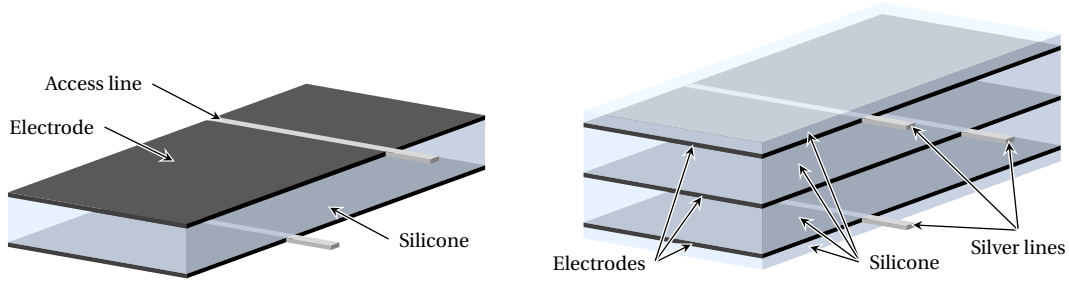


Figure 2.1: Most basic DEA possible. Only one dielectric layer with electrodes on both sides. The access lines can be made of any conductive material: copper, silver, carbon, etc.

Figure 2.2: Typical multi-layer DEA used in the CAM. Three electrodes sandwich two silicone layers. To insulate the device, two thinner silicone layers are added on the outside. Access lines are made out of silver.

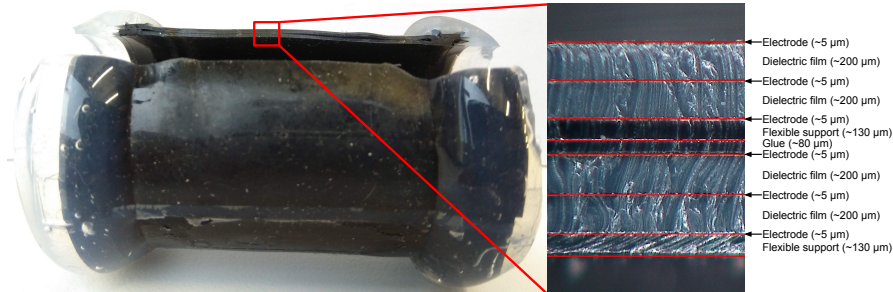


Figure 2.3: Early prototype of a rolled DEA tube with a cross section showing its internal structure of multiple active layers. An active layer consists of two electrodes (highlighted in red) and a dielectric film.

2.2.2 Capacitive nature and energy recovery

Consequently, from an electrical point of view, because of this layered structure DEAs are extremely capacitive loads [17]. The electrical models commonly considered can vary greatly in complexity from the basic ideal capacitor to the fully variable and voltage dependent capacitor with variable resistors in series and parallel (Fig. 2.4). In the work presented here, models (a) and (b) were mainly used as they represented well enough the behavior of the load for our needs.

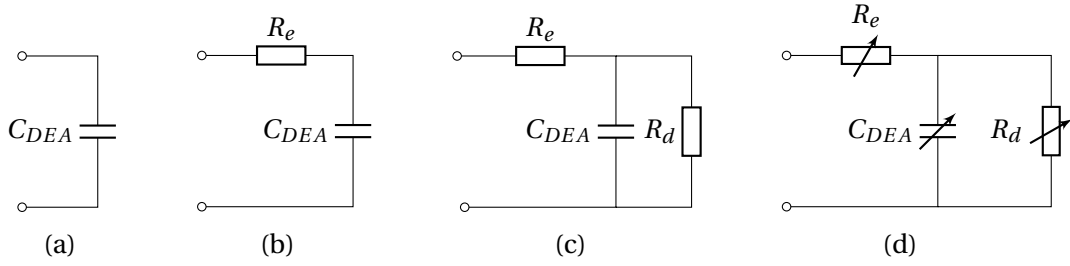


Figure 2.4: Typical models of DEAs. (a) The most basic with only the actuator's capacitance considered. (b) The model takes into account the access resistance of the electrodes of the DEA. (c) The leakage resistance of the dielectric layer is considered. (d) Most complete and complex model with all of the parameters variable to take into account the deformation experienced by a DEA.

This capacitive nature is the origin of one of the main challenges and selection criteria for the design of the electronics: when fully charged and deformed, DEAs end up storing a significant amount of electrical energy in themselves because only a small fraction of this energy is converted into mechanical deformations [18]. This means that, to bring back the actuator to its original shape, this electrical energy must be removed somehow. Currently, this is most commonly achieved by simply dissipating this energy through a resistive element in the form of heat. This strategy, however, is absolutely not adequate for applications aimed to be located inside a living body where temperature is critical as is the case with our application.

Therefore, the electronics must integrate a strategy that allows this energy to be recovered from the load to reduce losses and improve overall efficiency.

2.2.3 High voltages

The other characteristic and major challenge that stems from working with DEAs is the voltage levels they require to operate. Indeed, the motion of the actuator happens when a high enough voltage is applied across the two electrodes so that the electrostatic force becomes large enough for the electrodes to move towards one another. This will thus compress the dielectric layer vertically which will then expand laterally as depicted in Fig. 2.5.

To maximize this electrostatic force and thus the deformations and displacements of an actuator, one must aim to work close to the breakdown limit of the dielectric material. In our case, as mentioned earlier, the material used is the Elastosil® 2030 which has a dielectric strength of approximately $100 \text{ V}/\mu\text{m}$. Meaning that, since we are working with $100 \mu\text{m}$ thick sheets, the voltages required can reach up to 10 kV .

An option to reduce the voltages required would be to work with thinner sheets which are also available in the market. However, one must then be aware of two new significant drawbacks. First, the overall manufacturing process becomes increasingly more difficult and more

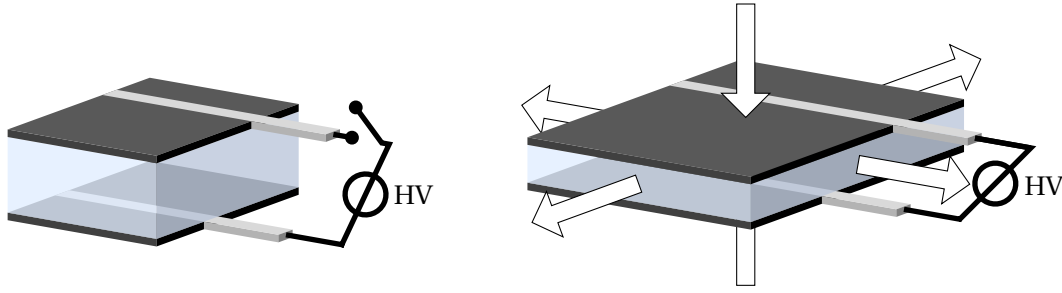


Figure 2.5: Basic working principle of a DEA. On the left, the actuator is not connected to the power supply. On the right, a high voltage is applied to the DEA; the electrodes squeeze vertically the dielectric layer which expands laterally.

expensive especially with $50\mu\text{m}$ sheets or thinner [19]. And second, the electrodes must also become thinner so as not to stiffen too much the actuator and consequently be detrimental to its attractive characteristics of flexibility and large displacements. In addition to making more difficult an already challenging manufacturing process, reducing the thickness of the electrodes will drastically increase their resistance and thus Joule losses as is the case in [20] where a $1.4\mu\text{m}$ thick DEA was designed with massively resistive electrodes ranging from $20\text{ M}\Omega$ to $5\text{ G}\Omega$ compared to the approximately $100\text{ k}\Omega$ we obtained.

It was therefore decided that the targeted output voltage that the electronics must be capable to supply was of 8 kV . This includes a safety margin to avoid any risks of voltage breakdown in the load.

2.2.4 Design requirements summary

In addition to the parameters imposed by the load itself, other requirements were also set according the needs of the application itself such as the maximal time allowed for the voltage to increase from 0 kV to 8 kV , the duration during which the voltage had to be kept up, etc. Table 2.1 below gives a summary of all of the design requirements imposed by the load used as well as by the application itself. The time durations listed essentially represent the beating frequency of an adult's heart at rest of approximately 1 Hz or $60\text{ beats per second}$.

Parameters	Specifications
Load capacitance	$2 - 5\text{ nF}$
Electrode access resistance	$\sim 100\text{ k}\Omega$
Input voltage	12 V
Output voltage	$0 - 8\text{ kV}$
Charging time from 0 V to 8 kV	$< 100\text{ ms}$
Duration at 8 kV	500 ms
Discharging time from 8 kV to 0 V	$< 100\text{ ms}$
Duration at 0 V	500 ms

Table 2.1: Design specifications and requirements for the high voltage power supply.

2.3 High voltage power electronics

With the design requirements set, a selection process can now be undertaken to determine which electronics topology is the most suitable to meet those specifications. Additionally, they bring forward the fact that the voltage levels to manipulate find themselves in a difficult spot between two major fields of electronics: the power grid with voltages of several hundreds of kilovolts and more "usual" high voltages of around 400 V to 800 V found in e.g. electric cars [21] to 1.5 kV in e.g. photovoltaic power systems [22][23]. It is difficult because it means that very few electronic components that exist are designed to operate in the voltage range DEAs require while offering adequate performances. The prime example of this is the fact that there exists currently in the market only one range of MOSFETs capable to withstand "only" up to 4.5 kV: IXYS' IXTxxxN450 product range [24]. For higher voltages, relays are used but their characteristics are poor with slow reaction times and bulky packaging. This specific problematic is discussed in further details in Section 5.3 but this fact influenced the final choice of topology.

In the following sections, the topologies commonly used to amplify an input voltage are explored and judged according to their ability to meet the design requirements.

2.3.1 Amplifiers

Amplifier-based circuits can be a very interesting solution to supply high voltages and custom voltage waveforms to a load. It is the currently preferred method of the CAM to test and actuate DEAs. The model used is the very capable Trek 20/20C-HS high speed and high voltage amplifier shown in Fig. 2.6 which can supply up to 20 kV with a large slew rate of at least 800 V/ μ s [25].

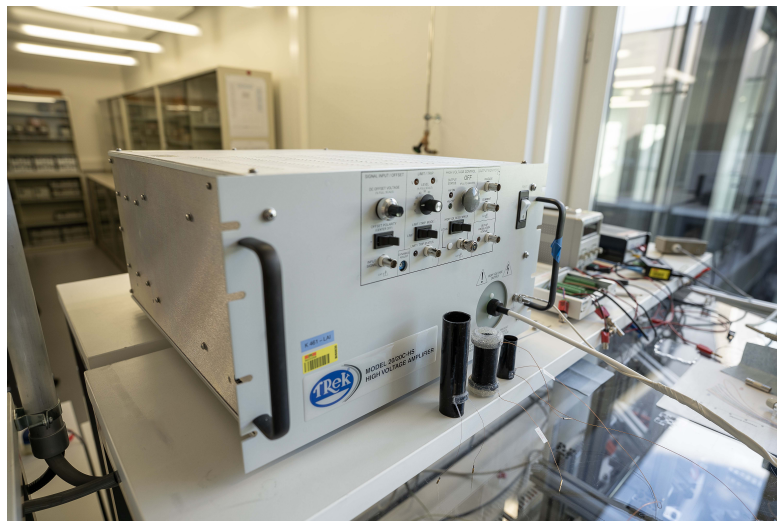


Figure 2.6: Photography of the Trek 20/20C-HS high voltage amplifier used in the Center for Artificial Muscles. Three DEA tubes can be seen at the front for scale.

While the existence of this device proves that this topology is more than capable to supply the voltages required, one must be aware of several downsides that come with it in regards to portable DEA applications. Such as the fact that this topology actually needs internal power supplies which themselves supply the high rail-to-rail voltages as shown in Fig. 2.7 which presents an overview of the working principle of the Trek 20/20C-HS. Meaning that, no matter what, such a system will have to include one of the other topologies mentioned in this chapter thus adding to its overall size and complexity.

Additionally, amplifier circuits appear to be unable to work bidirectionally as energy can only flow from the input to the output.

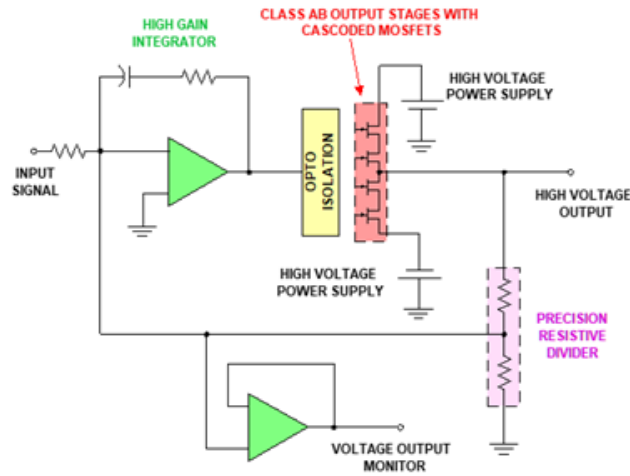


Figure 2.7: Overview of the internal circuit of the Trek 20/20C-HS amplifier [25].

2.3.2 Charge pumps

Charge Pumps are centered around capacitors which they use to gradually increase the voltage throughout the system mainly through the use of active switches. A significant advantage of these topologies is the possibility to completely integrate them on silicon wafers since they are not inductor-based like the DC-DC converters presented hereafter which allows to have extremely compact electronics.

The circuit at the basis of this category is the N-Stage Charge Pump shown in Fig. 2.8 and extensively discussed in [26] where numerous variations of this charge pump are presented. This topology works by alternatively opening and closing every other switch in synchronization with a clock signal V_{Ck} that has an amplitude equal to the input voltage ($V_{Ck} = V_{in}$). When the switch S_1 is closed, the following switch S_2 is open, $V_{Ck} = 0V$, and $\overline{V_{Ck}} = V_{in}$ to charge the capacitor from the source. Then S_1 is opened, S_2 is closed, $V_{Ck} = V_{in}$, and $\overline{V_{Ck}} = 0V$ which shifts up the potential across the first capacitor to $V_{in} + V_{Ck}$. This capacitor then discharges itself into the following one. This process is then repeated, shifting up the voltage at each step by V_{Ck} until the targeted output voltage is reached.

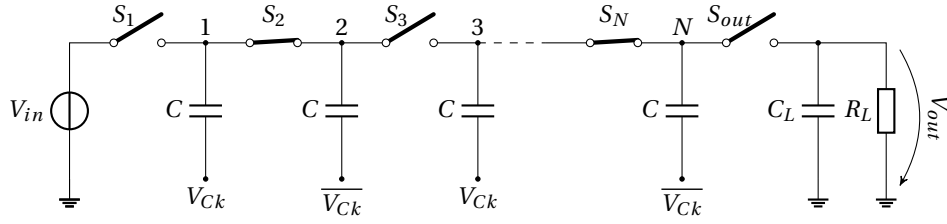


Figure 2.8: Ideal N-Stage Charge Pump.

In ideal conditions and with enough stages, charge pump topologies could in theory be able to supply extremely high voltages from a low input power supply. However, several hundreds of stages would be necessary and thus an enormous amount of semiconductor elements to control and an equally large amount of losses through each component due to their parasitic elements.

For the energy recovery, bidirectional solutions for the N-stage charge pump have been studied e.g. in the works of Qian [27] and Chan [28] but are aimed towards low voltage and mid-to-high power applications. These works also reveal that these structures become extremely convoluted with numerous additional switches necessary.

2.3.3 Voltage multipliers

Voltage multipliers are another type of voltage amplifying electronics centered around the use of capacitors with, however, no active components. The main member of this family is the Cockcroft-Watlon Cascade shown in Fig. 2.9 of which many variations exist but have the same working principle. This particular topology requires an alternating input voltage to operate but generates a DC voltage at the output. An important feature of this system to note is that none of the components used must be able to survive the total final output voltage but they must rather be only rated for two times the peak input voltage. Additionally, it is really easy to control as no switches are required for the system to operate. However, here again, to obtain an extreme voltage gain the system would need hundreds of stages which would each add more parasitic elements and thus generate evermore losses along the way.

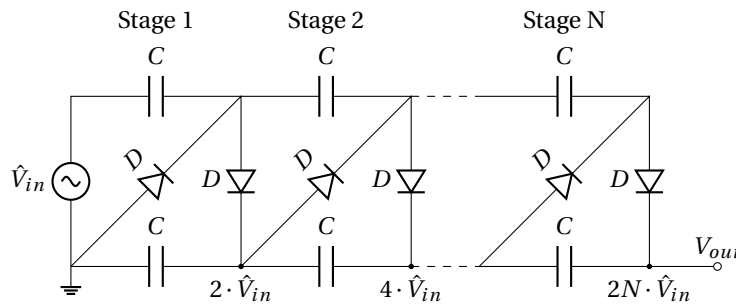


Figure 2.9: Cockcroft-Watlon Cascade.

Regarding its ability to amplify an input voltage, while it is theoretically capable to have gains necessary for our application, by itself it is greatly limited at amplifying a low input voltage to several kilovolts due to the increasing amount of parasitic elements that dissipate the input power with each additional stage. This limitation can be seen in commercially available devices such as the VM1566 integrated voltage multiplier from *Voltage Multipliers Inc.* [29] which has one of the largest gains in the market for HV applications of barely 5.8 with 14 consecutive stages for an input voltage of 1.2 kV and output voltage of 7 kV. A concept was proposed in [30] which allows such a system to work with low input voltages by connecting the voltage multiplier in series with a transformer circuit to achieve the first voltage step up necessary but to the detriment of size and dynamic.

As for the recovery of energy, voltage multipliers work exclusively unidirectionally. Therefore an additional circuit would be necessary to recuperate the energy in the actuator.

2.3.4 Marx generators and series-parallel topologies

A Marx generator such as the one of Fig. 2.10 is a circuit designed to generate extremely high voltage pulses by putting in series capacitors which were first charged while in parallel to each other. The pulse is generated by applying a voltage large enough across the leftmost spark gap switch such that a spark can happen which triggers an avalanche of sparks as each subsequent switch breaks down up to the last one connected to the load. The sparks effectively short circuit the resistors by allowing the current to flow through the gaps. Once the energy stored in the capacitors drops low enough, the sparks stop and the capacitors can be automatically refilled. Here, the resistors R_c are a critical part of the system as they prevent the charges from flowing back to the input power supply when the sparks are triggered. Not only must their resistance be large (in the $M\Omega$ range) to limit the back flow of current but their physical size as well (depending on the input voltage) to avoid electric arcs across them.

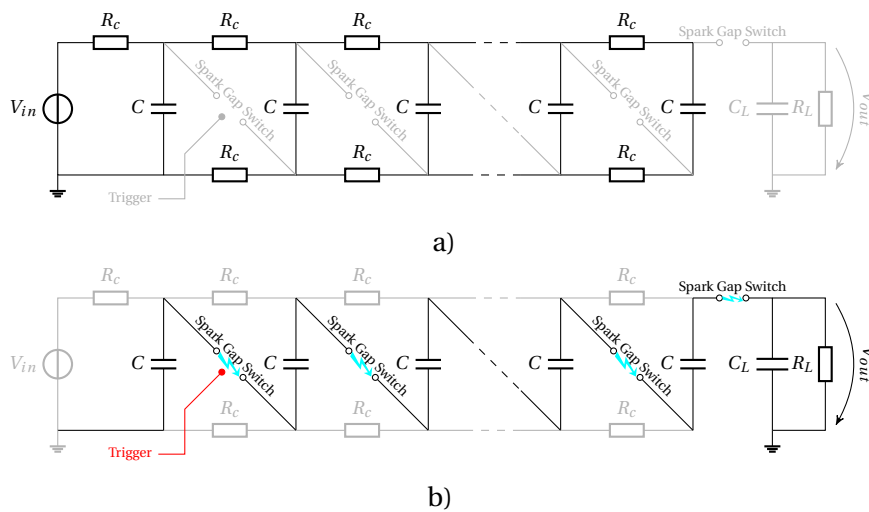


Figure 2.10: Marx generator a) when charging and b) when discharging its capacitors.

A more controllable variation of such a circuit exists in the form of the Series-Parallel Charge Pump (SPCP) shown in Fig. 2.11. The working principle is essentially the same as for the Marx generator and consists of alternatively putting capacitors in parallel to charge them by closing the switches P and P' and opening the switches S , and then in series to add their voltage to one another by reversing the state of the switches. While this topology is also theoretically able to generate high voltages, it is particularly sensitive to the parasitic capacitance of the components used especially when working with a high amount of stages. The complexity is further increased due to the larger number of switches necessary to commute. Voltage balance is also critical between the stages when the capacitors are in series to ensure that the switches do not risk to have voltages above their breakdown threshold.

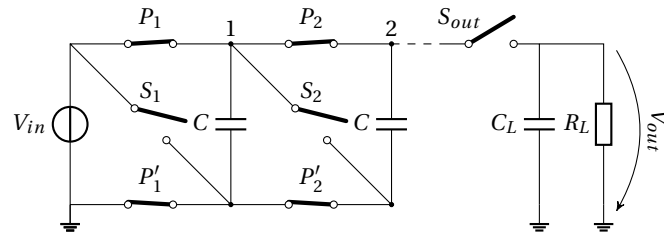


Figure 2.11: Series-Parallel Charge Pump.

While the Marx generator is not designed to be able to recover energy, the SPCP has the potential to do so with some modifications to the switching procedure. Potential which is explored in depth in the work of Almanza in [31] in which he designed a modified Solid State Marx Modulator (S^2M^2). In this new version of the circuit, the final switch S_{out} is replaced by an inductor to enable a reverse flow of current which will allow for the leftover energy in the load to go back to the capacitors of the S^2M^2 when they are put back in parallel. The charging voltage as well as the control signals for switches are supplied through wireless power transfer to allow for a precise and synchronous commutation of the switches during operation.

This system remains, however, quite complex as each stage requires its own microcontroller to manage the synchronization of the switches. In addition to that, in its current state, the voltage control is highly inflexible as the charging and discharging sequences must be hardcoded in advance in the controllers.

2.3.5 Transformer topologies

The full bridge converter is a classic topology which has been in use for several decades already in mid-to-high-voltage high-power conversion applications [32][33] e.g. to connect photovoltaic power systems to the grid [34] or to charge and discharge batteries [35]. The output voltage supplied is mainly a factor of the turns ratio $N_p : N_s$ of the transformer windings.

This topology works by controlling a four MOSFETs bridge to generate an alternating voltage across the transformer. Voltage which is amplified thanks to the turns ratio of the inductors and rectified on the secondary side, commonly by diodes.

This topology can also be modified to work bidirectionally by replacing the diode-based rectifier with an active MOSFET-based rectifier as shown in Fig. 2.12. With such a modification, this converter becomes perfectly symmetrical and can thus be driven in such a way that the secondary active rectifier becomes the main bridge during the discharge phase and with the primary bridge acting as a rectifier.

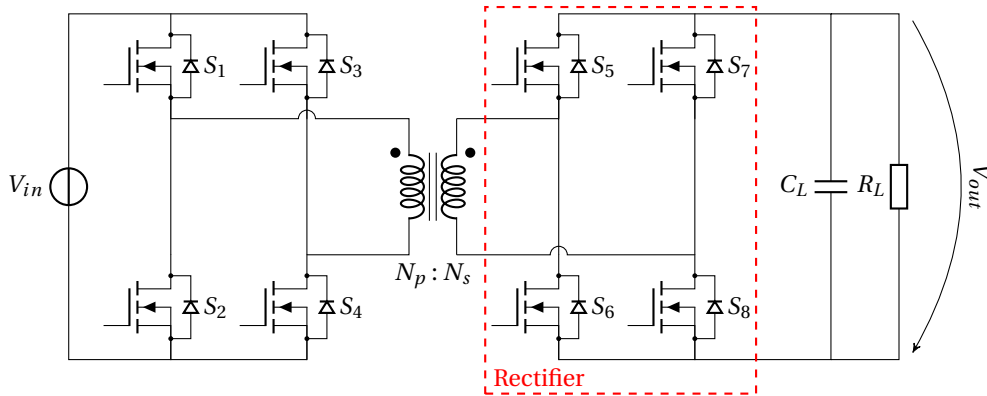


Figure 2.12: Full bridge bidirectional converter.

The main and major inconvenient of this system is not only the number of switches required to operate but the fact that each of the four switches on the high voltage side must be capable to withstand the full output voltage of several kilovolts thus taking a significant amount of space. This in itself, as mentioned earlier, would be a significant challenge.

2.3.6 Switch-mode power supplies

Switch-mode power supplies are one of the most common ways to step-up (or down) an input voltage. Their mode of operation is centered around a switch which is continuously turned ON and OFF to send pulses of energy towards the load. The sequential nature of the energy flow implies that at some point during the operation the energy must be briefly stored in a component. This is commonly achieved by using inductors but also occasionally capacitors as shown further below.

This type of power supplies can be classified into two families: isolated and non-isolated converters.

Non-isolated converters

Non-isolated converters include the most common and basic converters such as the Boost, Buck, and Buck-boost shown in Fig. 2.13. These converters work by exclusively storing their pulses of energy in an inductor and the output voltage is directly related to the duty cycle imposed during operation.

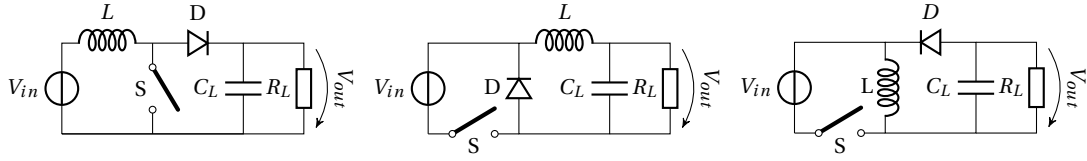


Figure 2.13: Non-isolated converters. Left, the boost. Middle, the buck. Right, the buck-boost.

Regarding the converters which also use capacitive temporary energy storage, one can find the famous Ćuk Converter and the Single-Ended Primary-Inductor Converter (SEPIC) topologies of Fig. 2.14. The main advantage of having integrated capacitive storage is smoother input and output currents in the system. Additionally, the SEPIC also provides an output voltage with the same polarity as the input voltage. However, these topologies are mainly designed for low voltage applications in which the input voltage varies slightly between being higher or lower than the output voltage while needing a constant output voltage.

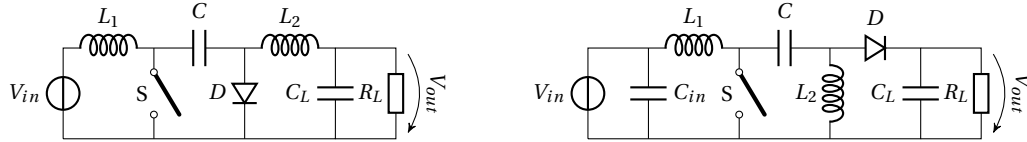


Figure 2.14: Left, the Ćuk Converter. Right, the Single-Ended Primary-Inductor Converter (SEPIC).

These basic circuits have already been the subject to advanced research to further improve their reliability, efficiency and overall performances. For example, Tofoli presents in [36] an extensive list of various adaptations of the Boost Converter designed to improve numerous aspects of this topology. Ultimately, the author concludes that non-isolated boost-based converters are not well adapted to achieve high-voltage step-up due to their parasitic elements. Some notable solutions to increase the gain are listed – such as the Cascade Boost or the quadratic three-level boost – but they only allow for a limited increase of gain.

As for the energy recovery, some of the circuits presented can be modified to work bidirectionally by replacing their diode with a switch as was done in [37] where a bidirectional buck-boost was designed. However, all of the components must be able to support the final output voltage compared to other topologies further below. Meaning that several HV switches would be necessary.

Isolated converters

In his publication [36], Tofoli also mentions the use of coupled inductors to increase the energy possible to transfer towards the load, to offer galvanic isolation as well as to permit higher voltage step-up by adjusting the turns ratio of the windings. One of the great classics making use of this feature is the flyback converter shown in Fig. 2.15 which itself is a modified version of the buck-boost converter shown earlier.

While other couple inductor-based topologies exist such as the Tapped-inductor boost (TIB) of Fig. 2.16, the flyback has the great benefit of having a total isolation between the primary and secondary side. Meaning that if components or the load are damaged and shortcut, the rest of the circuit remains safe compared to the TIB which can still allow a current to flow from the input power supply to the load.

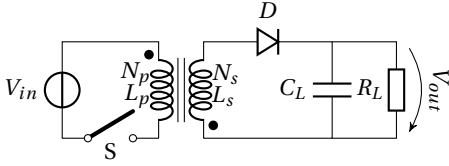


Figure 2.15: The Flyback converter.

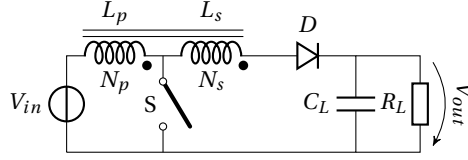


Figure 2.16: The Tapped-inductor boost.

The Flyback topology has already proven itself capable to supply ultra-high voltages in applications such as Cathode Ray Tubes (CRT) displays or more importantly in DEA based systems as shown further below. Additionally, this topology can be easily modified to allow a bidirectional flow of energy by integrating a switch in parallel to the diode on the secondary side. Due to the isolation provided by the coupled inductor, only this secondary switch must be capable to withstand the full output voltage targeted which is greatly advantageous. This modification allows the system to remain extremely simple with a very low amount of components.

The potential of this structure was revealed in the work of Thummala [38][39] in which he presents the first designs of a high voltage bidirectional flyback DC-DC converter such as the one shown in Fig. 2.17. With this system, he managed to amplify an input voltage of 24 V up to 2.5 kV across a capacitive load with an efficiency of 89%, and to discharge and recuperate 84% the energy through the same system. He also laid the groundwork for the design of the coupled inductor which is the core component of the flyback structure.

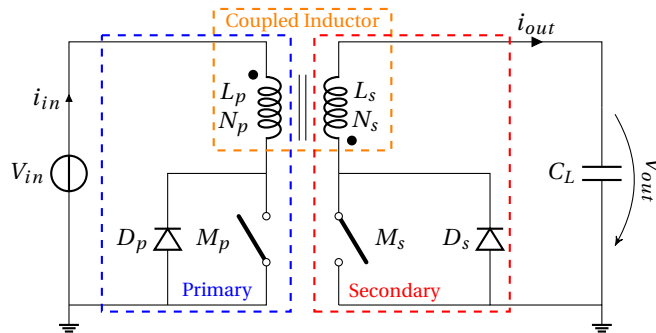


Figure 2.17: Basic schematic of a bidirectional DC-DC flyback converter. L_P is the primary and L_S the secondary inductance combined as a coupled inductor (orange) of N_P and N_S turns respectively. C_L represents an ideal Dielectric Elastomer Actuator.

2.4 Conclusion

Ultimately, Table 2.2 summarizes some of the most important characteristics of the previously discussed topologies. In this table, a tick mark ✓ is assigned to the characteristics which are clearly within the design requirements, a dash – indicates that the corresponding characteristic may require careful attention but is not eliminatory, and a cross X means that the corresponding characteristic renders the topology unable to meet the design requirements.

Topology	Voltage amplification	Bidirectionality	Physical volume	Circuit complexity
Amplifiers	✓	X	X	–
Charge pumps	–	✓	✓	X
Voltage multipliers	X	X	✓	✓
Marx generators	✓	✓	–	–
Transformers	✓	✓	X	–
Non-isolated converters	X	✓	–	✓
Isolated converters	✓	✓	–	✓

Table 2.2: Comparison summary of voltage amplifying topologies.

While several of them are capable of supplying the high voltages necessary, few combine this feature with an ability to recover the energy from the load. And even fewer are as simple as the Flyback Converter from the isolated converters family.

Indeed, its potential to generate high voltages and to allow a bidirectional flow of energy, combined with a very simple circuit using a low amount of components makes the Flyback the most promising topology to work with to power DEAs. This claim was also confirmed by Hoffstadt in [40] where he presents a detailed comparison of the benefits brought by a bidirectional flyback compared to other unidirectional converters with active discharging circuit when working with output voltages of around 2.5 kV.

This topology thus became the centerpiece of the following work.

3 Ultra-high voltage generation with a flyback DC/DC converter

3.1 Introduction

The flyback DC/DC converter is a well-known power converter topology with some of the earliest mentions in the 1970s for space-related applications [41][42]. Since then, the flyback has been used in numerous and various applications typically requiring high voltages such as Cathode Ray Tube (CRT) imaging [43], xenon flashlights [44], lasers, etc. And now, over the last decade, the interest in the flyback converter has significantly grown for DEA-based applications due to its advantageous characteristics of simplicity and efficiency.

In this chapter, the discussion is focused on the ability and limitations of the flyback to generate the high voltages necessary to operate DEAs.

3.2 Working principle

As mentioned in the previous chapter, the bidirectional flyback converter shown in Fig. 3.1 belongs to the family of switch-mode power supplies. This means that its behavior is highly dependent of the conduction state of its various switches and diodes. One can therefore analyze its behavior by segmenting it in several phases and steps.

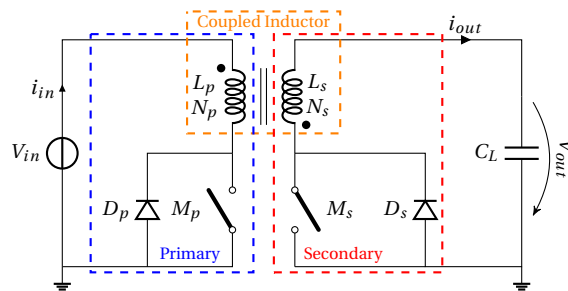


Figure 3.1: Basic schematic of a bidirectional DC-DC flyback converter. M_p and M_s are the primary and secondary switches respectively. C_L represents an ideal Dielectric Elastomer Actuator.

In the case of the bidirectional flyback, the first way to partition its working principle is by separating its charge and discharge phases as shown in Fig. 3.2. It is interesting the study both phases independently because, while they work essentially identically, crucial differences can be observed such as the influence of parasitic elements being more critical during the charge phase or the variation of the output voltage being more critical during the discharge phase as shown further below.

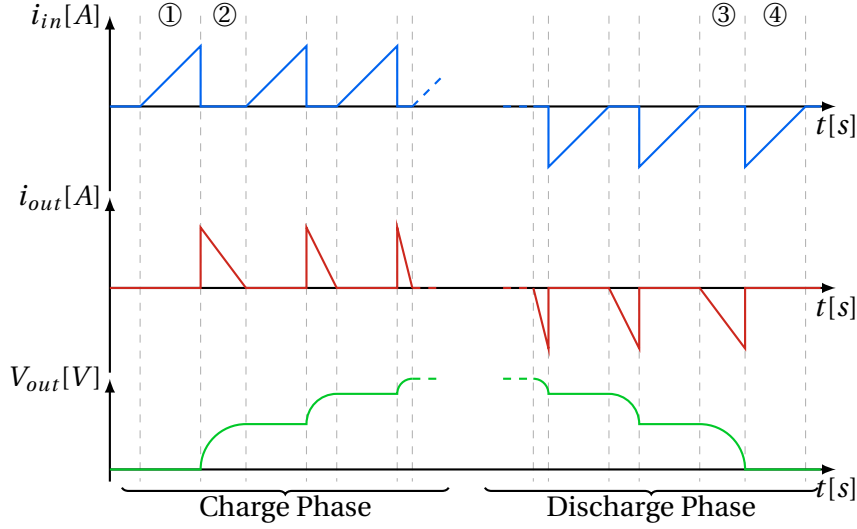


Figure 3.2: Ideal input current i_{in} , output current i_{out} and output voltage V_{out} in a bi-directional flyback converter. The slope of i_{out} varies during the charge and discharge phases because of the rise and following drop of V_{out} .

Regarding the aforementioned phases, they can be further decomposed in steps as follows. During the charge (discharge) phase, the switch M_p (M_s) alternates between closed ① and open ② states (③ and ④). While in the former state, a current i_{in} (i_{out}) flowing through the inductance L_p (L_s) linearly increases. This generates a magnetic flux in the core of the coupled inductor effectively storing energy in it. Since the core is not in saturation, the energy stored during the charge and discharge phases is given respectively by

$$\mathcal{E}_{mag} = \frac{1}{2} L_p i_{in}^2 \quad (3.1)$$

$$\mathcal{E}_{mag} = \frac{1}{2} L_s i_{out}^2 \quad (3.2)$$

The amount of energy that can be stored in the coupled inductor is however limited by the geometry and the material of the core used. Indeed, the magnetic flux generated by i_{in} (i_{out}) must not exceed the core's saturation value B_{sat} to avoid unnecessary losses. The maximum amount of energy $\mathcal{E}_{mag,max}$ that can be stored during each commutation in any given core can be found through

$$\mathcal{E}_{mag,max} = \frac{1}{2} A_L \left(\frac{B_{sat} \cdot l_e}{\mu_e \cdot \mu_0} \right)^2 \quad (3.3)$$

with A_L the inductance factor, B_{sat} the saturation magnetic flux density, l_e the magnetic path length, and μ_e the relative effective permeability. To reach the highest output voltage as fast as possible, one must seek to work at the limit of the saturation of the core and to do so, the switch M_p (M_s) must be closed long enough for i_{in} (i_{out}) to increase so that (3.1) (respectively (3.2)) is equal to (3.3).

When the switch is subsequently reopened, the current i_{in} (i_{out}) stops flowing and the energy stored is released from the core through the generation of a current i_{out} (i_{in}) that flows towards the capacitive load (towards the power supply).

During the charge phase, the output voltage increases from $V_{out}[i]$ of period i , to $V_{out}[i + 1]$ at the end of period $i + 1$ such that

$$\mathcal{E}_{mag} = \frac{1}{2} C V_{out}^2[i + 1] - \frac{1}{2} C V_{out}^2[i] \quad (3.4)$$

Theoretically, with enough commutations of M_p any output voltage could be reached. However, as shown further below, this is unfortunately not the case with real applications.

3.3 Charge phase

As highlighted by the works referenced in the previous chapter, high voltage applications of the bidirectional flyback have all in common the characteristic of never operating with voltages higher than 2.5 kV. This can be attributed to two main factors: the first being that a flyback is intrinsically limited in its ability to supply high voltages because of parasitic elements which can be found throughout the system; and the second being that, currently in the market, high voltage-rated switches with the required performances are rare to non-existent. The former factor will be discussed extensively in this chapter while the latter will be the subject of Chapter ??.

For the purpose of clarity and simplicity, since only the charge phase will be considered in this section, the following analyses and explanations are conducted on a manufactured unidirectional flyback (Fig. 3.3) inherently limited to 4.2kV as it best displays the studied behavior.

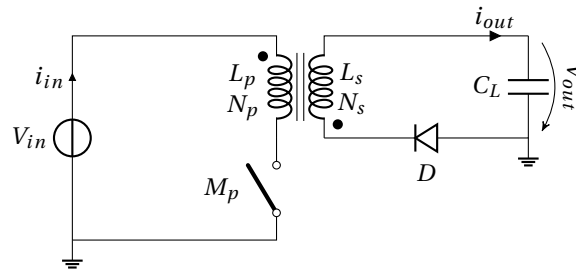


Figure 3.3: Basic model of the unidirectional flyback converter

All of its control specifications and components used can be found in Tables 3.1 and 3.2. The analyses done hereafter remain applicable to the bidirectional case as integrating a secondary switch M_s into the system will simply require adding the value of its parasitic capacitance to the value of C_D (the parasitic capacitance of the diode) in the following models.

Parameters	Value
Input voltage V_{in}	12 V
Output voltage V_{out}	0 - 4.2 kV
Max input current \hat{I}_{in}	6 A
Load capacitance C_{load}	1.5 nF
Primary MOSFET on time t_{on}	37 μ s
Driving frequency f_d	10 kHz
Control strategy	Fixed frequency
Charging time T_{ch}	6 ms

Components	Characteristics
Primary MOSFET M_p	500 V, 20 A [IRFP460]
Secondary diode D	5 kV, 0.2 A, $C_D = 30$ pF [R5000F]
Coupled inductor	See Table 3.2

Table 3.1: Specifications and components of the 4.2 kV unidirectional flyback converter

Parameters	Value
Material	Ferrite N87
Geometry	E 25/13/7
Air gap	0.25 mm
Max energy stored in core $\mathcal{E}_{mag,max}$	1.3 mJ
Winding method	Un-segmented Continuous Overlapping
Primary inductance L_p	72.5 μ H
Primary leakage inductance L_{lp}	1.6 μ H
Primary winding capacitance C_p	12.6 nF
Primary winding resistance R_p	0.5 Ω
Secondary inductance L_s	31.7 mH
Secondary leakage inductance L_{ls}	774.2 μ H
Secondary winding capacitance C_s	28.5 pF
Secondary winding resistance R_s	16 Ω
Inter-winding capacitance C_W	51.6 pF

Table 3.2: Characteristics of the 4.2kV flyback's coupled inductor

3.3.1 Intrinsic voltage limitation due to parasitic elements

As mentioned earlier, in an ideal scenario, a flyback converter is capable to supply any output voltage with enough commutations of the primary switch M_p . However, as always, experiments show that that is not the case and the output voltage is actually limited and reaches a plateau that no amount of additional pulses of energy will make possible to overtake as presented in Fig. 3.4.

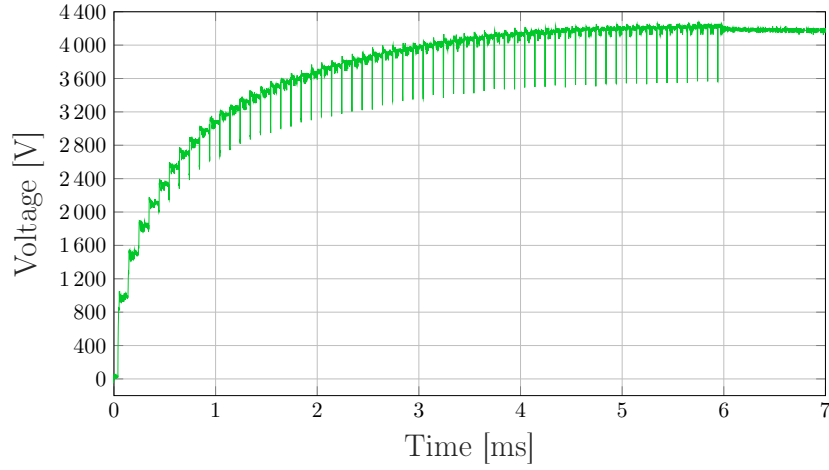


Figure 3.4: Output voltage across a 1.5 nF capacitive load measured on a unidirectional flyback intrinsically limited to ~ 4.2 kV. After 6 ms, M_p stops being commutated [45].

To find clues as to why the converter behaves this way, one must undertake a detailed observation of the currents flowing throughout the system. In Fig. 3.5 are displayed the waveforms of the primary and secondary currents in two different situations: first when the output voltage is still reasonably low and then when the output voltage reached its plateau.

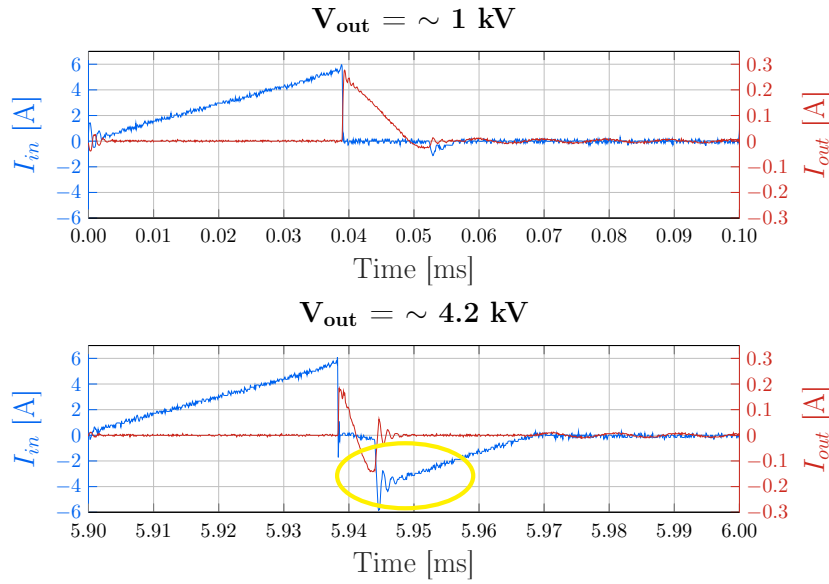


Figure 3.5: Upper graph, the current waveforms when the output voltage is still increasing. The currents behave nearly identically to those presented in Fig. 3.2. Small negative currents can however already be observed. Lower graph, the flyback reached its intrinsic plateau of 4.2 kV and significant negative currents (circled) are now clearly visible. For both graphs, the scaling factor for the right axis is equal to the turns ratio N_r of the coupled inductor.

One can note that, in the first case, the measured current waveforms behave nearly identically to the ideal current of Fig. 3.2. With, however, first signs of discrepancies in the form of small negative i_{in} and i_{out} currents. Negative currents which increase significantly and are clearly visible in the bottom graph of Fig. 3.5.

It was observed that the output voltage kept increasing as long as the negative peak value of the output current i_{out} was smaller than its positive peak value. Whereas when both peak values are equal, the flyback reached its output voltage plateau and all of the subsequent pulses of energy do not end up in the load but are effectively wasted. The implication of this behavior is that, upon reaching this state, all of the energy stored in the coupled inductor only ends up being stored or dissipated in parasitic elements of the circuit.

A first assumption one could make would be that this behavior is solely due to the diode on the secondary side and that its slow reverse recovery allows for some current to leave the load. This, however, is only partially correct. Indeed, if the amount of energy flowing throughout the unidirectional flyback is calculated using (3.1) and $\mathcal{E} = \frac{1}{2} C_D V_{out}^2$ as well as the information of Tables 3.1 and 3.2, one will find that approximately 1.3 mJ of energy is stored in the coupled inductor at each commutation of M_p while only 0.26 mJ of this energy ends up being stored in the junction capacitance C_D of the diode when the output voltage is at 4.2 kV. This thus leaves a significant portion of the energy originating from the coupled inductor that needs to be stored somewhere else in the structure, namely in the capacitive parasitic elements of the coupled inductor.

3.3.2 Flyback model with parasitic elements

From this deduction, a more precise electrical model of the flyback can be defined which takes into account the critical parasitic elements of all the components of the converter and mainly those of the coupled inductor as shown in Fig 3.6.

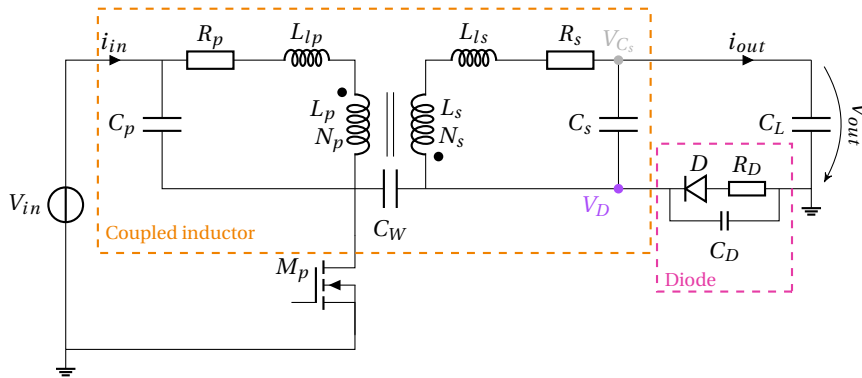


Figure 3.6: Schematic of the flyback converter with additional parasitic elements. C_p , R_p and L_{lp} are respectively the primary parasitic winding capacitance, wire resistance and leakage inductance. C_s , R_s and L_{ls} are the equivalent for the secondary side of the coupled inductor. C_D is the junction capacitance of the diode and R_D its forward resistance.

This model adds to the basic schematic of Fig 3.3 the parasitic capacitances C_p and C_s of both the primary and secondary windings as well as their respective leakage inductances L_{lp} and L_{ls} , and resistances R_p and R_s . Importantly, the inter-winding capacitance C_W is also taken into account as well as the resistance R_D and the junction capacitance C_D of the diode.

3.3.3 Influence of capacitive parasitic elements

With this improved model defined, one can now focus one's attention on a particular electrical potential found in the circuit to understand the influence of each parasitic element: the potential V_D shown in Fig 3.6. Indeed, V_D has the particularity of experiencing very large variations during a commutation cycle depending on the state of the semiconductor components. Fig. 3.7 displays the waveform of V_D in relation to the currents during one typical commutation cycle. Six major different steps were identified and analyzed hereafter.

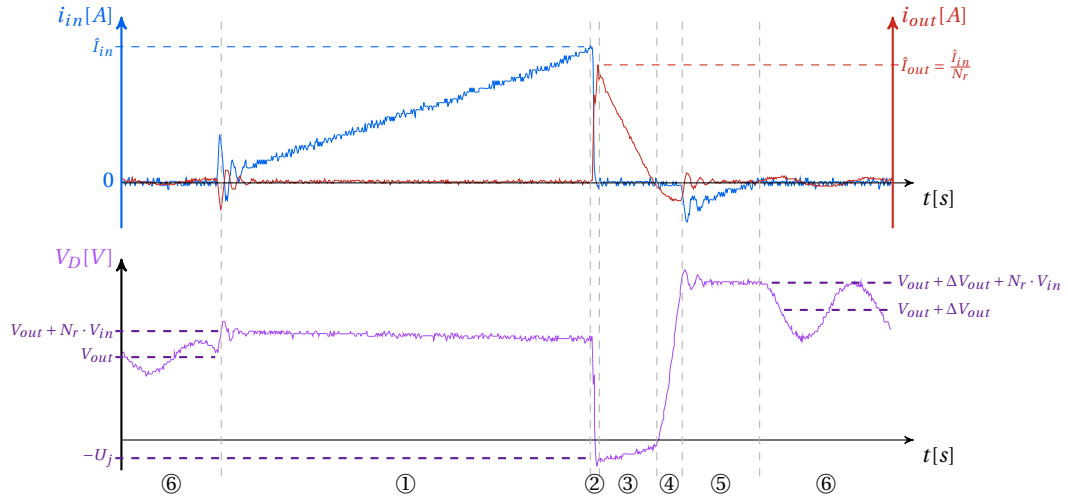


Figure 3.7: Measured evolution of the potential V_D put in relation to the currents during one commutation cycle of the flyback. 6 steps of significant importance were identified during said cycle.

Step ①: As soon as the primary switch is closed, the input current linearly rises. During this phase, the coupled inductor briefly behaves like a transformer and thus V_D rises to $V_{out} + N_r \cdot V_{in}$ with N_r the winding ratio of the coupled inductor. Depending on the design of the coupled inductor, a significant amount of losses can happen during this phase due to the large current flowing through M_p 's ON-resistance, the winding's resistance R_p and the primary leakage inductance L_{lp} .

Step ②: This phase starts as soon as the input current stops growing after the opening of the switch. It is during this time that the energy stored as a magnetic flux in the core starts to generate a current on the secondary side. This part of i_{out} represents the flow of charges removed from the parasitic capacitances C_W , and C_D and sent towards the potential V_{Cs} to charge C_s and C_L . This current rises until the potential V_D drops low enough for the diode to start conducting.

Step ③: As soon as the diode enters in conduction mode, all the energy left in the coupled inductor flows towards the load capacitor which effectively increases the output voltage by an amount of ΔV_{out} . During this phase, a portion of this energy is lost in the resistive elements such as the winding's secondary resistance R_s and the diode's forward resistance R_D .

Step ④: This step is the crucial one where the parasitic elements influence the most the system. Indeed, when the current i_{out} falls below 0A, some of the charges stored in the load capacitor C_L and all the ones stored in C_s start leaving which opens the diode. This should theoretically stop any more charges from leaving. However, as shown in Fig. 3.5, a negative current continues to flow. This current exists because of the need for the potential V_D to rise back up to $V_{out} + \Delta V_{out}$ to balance the voltage across the coupled inductor. This equilibrium is only reached when the parasitic capacitances C_W and C_D store enough charges to raise the voltage across them to the new output voltage. As the output voltage gradually increases with each pulse, so does the negative current which also, consequently, sends back energy towards the primary side through L_s with some more losses due to the leakage L_{ls} .

Step ⑤: Once this equilibrium is reached, the negative i_{out} current falls to 0A and a negative i_{in} current is generated on the primary side as a sort of reverse flyback. The latter current is allowed to flow thanks to the body diode of the MOSFET which starts conducting. Similarly to Step ①, the potential V_D is further increased to $V_{out} + \Delta V_{out} + N_r \cdot V_{in}$ while this input current flows.

Step ⑥: Finally, once all the currents have stopped, the potential V_D drops back to the new value of the output voltage $V_{out} + \Delta V_{out}$ until a new commutation cycle starts.

Regarding the energy flow, it is now possible to better estimate how much of the energy coming from the coupled inductor ends up stored in the parasitic elements. To continue with the example of Subsection 3.3.1 and Fig. 3.5, this means that when the output voltage is at 4.2kV, from the 1.3mJ stored in the coupled inductor, approximately 0.26mJ end up being stored in C_D , 0.25mJ in C_s , and 0.46mJ in C_W . Additionally, this reverse flow of current implies that 0.31mJ (with a peak negative current of 140mA) are transferred back in the coupled inductor through L_s which generates the current mentioned in Step ⑤. Thus, 1.28mJ end up stored in the parasitic capacitances or sent back due to the reverse current, with the small rest being dissipated through the various resistances.

This example shows how critical the parasitic capacitances of the coupled inductor and the diode are in limiting the maximum output voltage reachable with this structure. The reason why they have such a significant and increasing influence at high voltages is because the energy they store is directly proportional to V_D^2 which is essentially equal to V_{out}^2 . Therefore, at high voltages, it becomes essential to minimize the parasitic capacitive elements (C_s , C_W and C_D) through a careful choice diode and secondary switch for the case of a bidirectional flyback – which can help reduce C_D – and a meticulous design process for the coupled inductor.

3.3.4 Simulations

This more detailed model was subsequently implemented in the SPICE simulator *LTSpice* to test the aforementioned theory and to confirm that it allows to describe adequately and sufficiently the behavior of the flyback during its charge phase. Figure 3.8 displays the model in the simulator with the varying parameters highlighted in red, namely the inter-winding capacitance C_W , the secondary inter-layer capacitance C_s and the diode capacitance C_D .

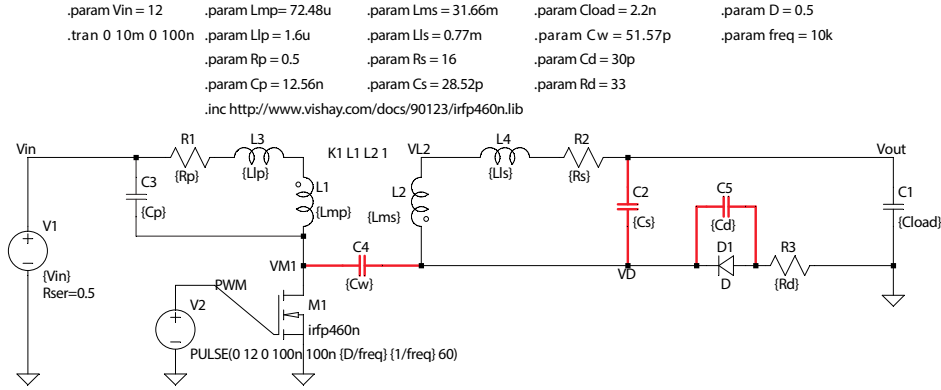


Figure 3.8: Model considered for the SPICE simulations. The parasitic capacitances highlighted in red are first set to 0 F, then set to be equal to the values of Table 3.2, and finally set to three times the value of the same table.

Then, the following procedure was put in place. Three runs of simulations were conducted for each of which the values of the highlighted capacitances were different. During the first run, the capacitances were completely removed (set to 0 F) thus effectively creating an ideal flyback; during the second run, their values were set to the ones of Tables 3.1 and 3.2; and during the last run, the capacitances were tripled in value compared to the previous run.

Figures 3.9 and 3.10 present the resulting simulated input and output current waveforms respectively for the three cases. These simulation runs are also compared to actual measurements obtained with the manufactured flyback. From these graphs, one can clearly see that, after the addition of the capacitive elements in the model, the negative currents do appear in a similar way as in the real flyback and they grow larger with larger capacitances. The consequence of such a behavior can then be observed on the output voltage in Fig. 3.11 where it is drastically reduced after the introduction of the parasitic capacitances. Especially when their values are high.

These results thus confirm that the parasitic capacitances found on the secondary side of the flyback converter are the main culprits behind the negative currents observed on the real device and thus are a major factor limiting the output voltage possible to reach with such a structure.

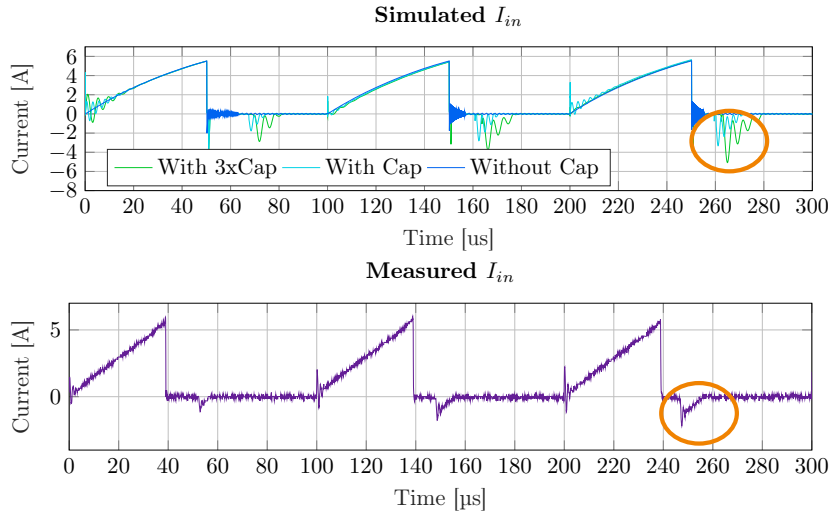


Figure 3.9: Top, simulated input current waveforms of three successive pulses obtained using a model without and with parasitic capacitances, and with parasitic capacitances three times larger. Bottom, the input current measured on a real flyback. Circled are the negative currents due to the parasitic capacitances.

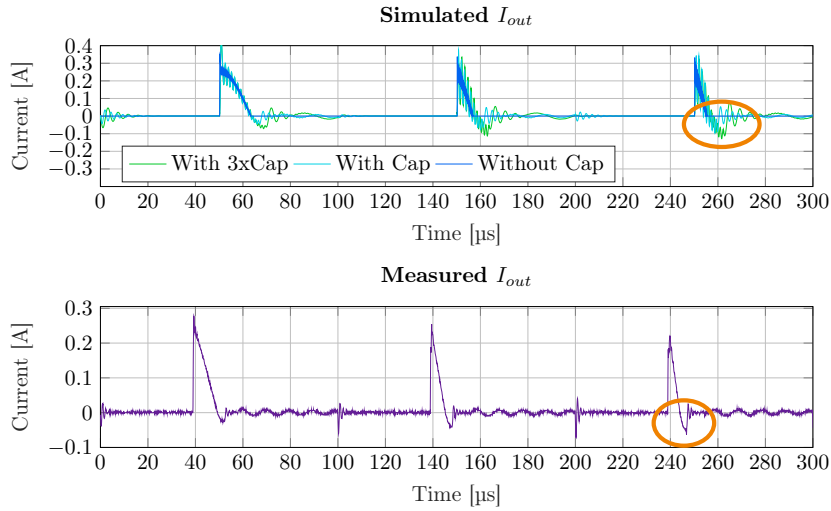


Figure 3.10: Top, resulting simulated output current waveforms obtained using a model without and with parasitic capacitances, and with parasitic capacitances three times larger. Bottom, the output current measured on a real flyback. The negative currents due to the parasitic capacitances are circled.

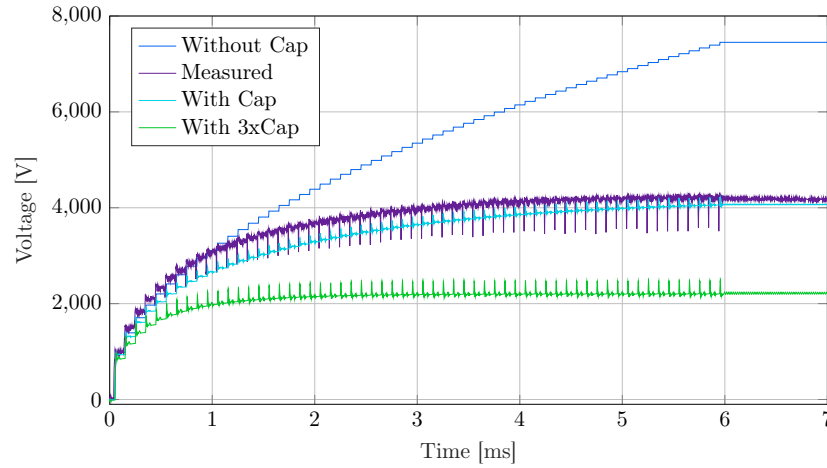


Figure 3.11: Output voltage simulated without and with parasitic capacitances, with parasitic capacitances three times larger, and output voltage measured on a real flyback converter.

3.4 Design considerations to improve high voltage capabilities

On the basis of those facts, one can now look towards finding strategies to improve the overall performances of the system.

In this section, the three main and most influential design considerations are presented.

3.4.1 Reduction of the parasitic capacitances of the coupled inductor

The first and most obvious one consists of implementing strategies to reduce the parasitic capacitances due to the winding of the coupled inductor of the flyback converter.

The winding of transformers and thus also of coupled inductors has been the subject of numerous in-depth research over the years such as [46] and [47] in which several winding strategies shown in Fig. 3.12 are analyzed and compared.

In both of those research studies, it was shown that by upgrading a continuous winding for a discontinuous winding the parasitic inter-layer capacitance can be reduced by at least 25 % with an equal amount of turns and layers. This gain is mainly due to the difference in voltage distribution across each layer. Indeed, in the discontinuous case, the voltage between two layers is constant all along the layers whereas in the continuous case the voltage between two opposing wires increases along the layers as shown in Fig. 3.13.

Thus, implementing the discontinuous topology is a first step towards reducing the inter-layer capacitances C_p and C_s . The main but nowadays negligible disadvantage of this winding method is that it is slightly more complex to manufacture because of the wire crossing back the layers which requires special arrangements for it to be held in place during the winding process.

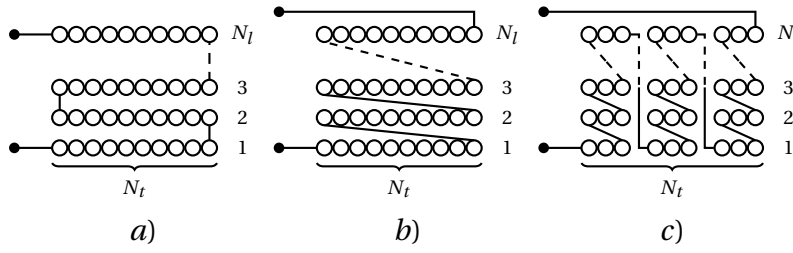


Figure 3.12: a) The continuous winding method. b) The discontinuous winding method. c) Segmented discontinuous winding method. Because of the voltage distribution, the inter-layer capacitance of the discontinuous winding can be expected to be at least 25% smaller than of the continuous winding. The segmented winding further helps reducing the capacitance at the cost of manufacturing complexity. N_l is the number of layers and N_t is the number of turns.

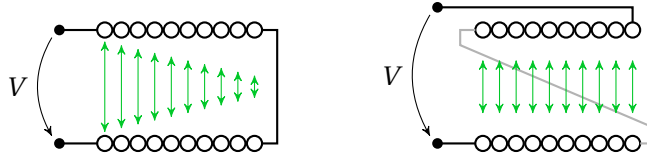


Figure 3.13: Evolution of the electrical potential in green between two layers of winding in a coupled inductor.

However, in the former study, the author also shows that the inter-layer parasitic capacitance could be further reduced if the winding is not only discontinuous but also segmented as shown in Fig. 3.12-c). These strategies were implemented on various cores for comparison. Their respective parasitic secondary capacitances were measured and are listed in Table 3.3. The last method – segmented discontinuous – presented extremely good results as demonstrated by the fact that with nearly two times the amount of turns – 720 compared to 380 for the others – the winding capacitance remains nearly three times smaller than the simple discontinuous method.

Parameter	Winding method	Capacitance	Nb. of turns
C_s	Continuous	28.5 pF	$N_s = 380$
C_s	Discontinuous	16.3 pF	$N_s = 380$
C_s	Segmented Disc.	5.8 pF	$N_s = 720$

Table 3.3: Measured inter-layer parasitic capacitance of different three winding topologies: continuous, discontinuous and segmented discontinuous .

Finally, to reduce the inter-winding capacitance C_W of the coupled inductor, a simple strategy exists and consists of separating the primary winding from the secondary by putting them side-by-side rather than overlapping one another as shown in Fig. 3.14-a) and b) respectively. Table 3.4 shows a comparison of the parasitic capacitances measured with both strategies. It was observed that the resulting capacitance was more than three times smaller with the Side-by-side topology.

3.4 Design considerations to improve high voltage capabilities

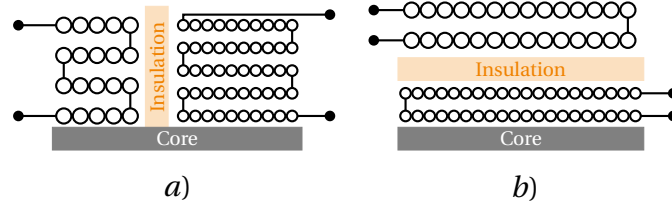


Figure 3.14: a) and b) show the side-by-side and overlapping winding methods respectively.

Parameter	Winding method	Capacitance	Nb. of turns
C_W	Overlapping	44.8 pF	$N_p = 18, N_s = 380$
C_W	Side-by-side	12.5 pF	$N_p = 18, N_s = 720$

Table 3.4: Measured inter-winding parasitic capacitance of different winding topologies: Overlapping and Side-by-side.

One should note, however, that the implementation of the aforementioned techniques to reduce the parasitic capacitances is done to the detriment of the leakage inductance which will increase, thus subsequently increasing the voltage stress on the primary MOSFET as well as reducing the overall efficiency of the system as shown further below. It will however not influence the ability of the flyback to increase its output voltage.

3.4.2 Coupled inductor cores

Another parameter that can also be modified to improve the performances of a flyback converter is the core of the coupled inductor itself. Indeed, since the voltage increase limitation comes from the fact that all the energy stored in the core ends up in the parasitic capacitances, an alternative strategy can be to increase the amount of energy stored in the coupled inductor's core during each commutation. To do so, one has three options according to equation (3.3): seek to increase the maximum saturation flux density B_{sat} , reduce the relative effective permeability μ_e , or look for a larger core with a bigger magnetic path length l_e .

A larger maximum saturation flux density can be achieved by changing the core material. In the case of ferrites, a wide range of different materials exist with as many different performances and targeted applications as shown in [48]. In our case, the ones considered would be the ones destined for switch-mode power supplies (or power transformers) as they offer low core losses and higher than average saturation flux densities (~ 0.5 T compared to ~ 0.45 T). Additionally, most of the standard cores found in the market have the option to have an integrated air gap to reduce the permeability. One can also be manually added by placing a spacing material between two core sides. For this latter case, the new relative permeability with air gap μ_g can be calculated using the following equation:

$$\mu_g = \frac{\mu_e \cdot l_e}{l_e + g \cdot \mu_e} \quad (3.5)$$

with μ_e the original relative permeability, l_e the magnetic path length and g the air gap length.

Other than ferrites, there exists powder cores which are manufactured by compressing into shape alloy powders of e.g. nickel, iron and molybdenum for Molypermalloy Powder (MPP) cores, nickel and iron for *Magnetics'* High Flux cores, or iron and silicon for XFlux cores. These cores combine the first two options listed above in one because not only does the material change but this compacted powder directly integrates a so-called distributed air gap in the core which greatly reduces the permeability. The three aforementioned core respectively have saturation flux densities of 0.8T, 1.5T and 1.6T.

However, two major downsides plague these distributed air gaps cores. The first being that their permeability value can be so low that this results in an increased peak saturation current. The consequence of this increase is the subsequent need for a large amount of winding turns to limit the peak current drawn from the power supply and thus bigger parasitic capacitances are to be expected. A selection of cores is listed in Table 3.5 for comparison to show the necessary amount of turn to reach the same peak saturation current.

Core type [A]	I_{sat} [A]	B_{sat} [T]	l_e [mm]	μ_e [-]	N [-]	Datasheet
MPP	6	0.8	63.5	550	~ 12	[49]
High Flux	6	1.5	63.5	160	~ 79	[50]
XFlux	6	1.6	63.5	125	~ 108	[51]

Table 3.5: Comparison of the amount of winding turns N necessary to reach the same peak saturation current I_{sat} for various distributed air gap cores with similar volumes.

The values were calculated with:

$$I_{sat} = \frac{B_{sat} \cdot l_e}{\mu_e \cdot \mu_0 \cdot N} \quad (3.6)$$

where B_{sat} is the saturation flux density, l_e is the magnetic path length, μ_e is the relative effective permeability, and N is the number of winding turns.

Consequently, from the distributed air gap category, the most suitable cores are the MPP ones as they offer a good trade-off between a relatively low permeability and a high saturation flux density.

The second major downside is that MPP cores are almost exclusively found in toroidal shapes which significantly complicates the winding process especially when the topologies of the previous section must be integrated. This ultimately essentially negates their aforementioned advantages.

In the end, the solution that was considered to improve upon the performances of the flyback discussed in Section 3.3 is the following one. The material remained a ferrite with the N87 material as it provides some of the best performances for our application. The core geometry was upgraded from an E core E25/13/7 ($A_e = 52 \text{ mm}^2$, $A_n = 61 \text{ mm}^2$, $V_e = 3020 \text{ mm}^3$) to an RM14 core ($A_e = 200 \text{ mm}^2$, $A_n = 107 \text{ mm}^2$, $V_e = 14000 \text{ mm}^3$) shown in Fig. 3.15. The volume increase was necessary as it allowed to not only increase the magnetic path length and thus the energy stored but also to more easily implement the discontinuous segmented and side-by-side winding topologies thanks to its larger winding window.

3.4 Design considerations to improve high voltage capabilities

Additionally, a custom air gap of 0.15 mm was integrated to further increase the energy stored.

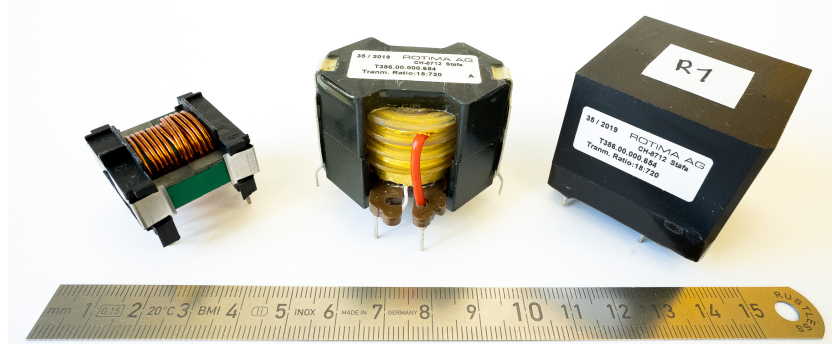


Figure 3.15: First E core coupled inductor prototype (left) and final RM core prototypes: bare, with visible segmented coil former (center) and encased in insulating plastic (right).

3.4.3 Upgraded coupled inductor

As hinted above, with the implementation of these design parameters, the new coupled inductor now presents significantly improved characteristics compared to the one used in Section 3.3 as shown in Table 3.6 below. The major relevant improvements are highlighted in green. Figure 3.16 shows a schematic representation of a cross section of the final coupled inductor.

Parameters	Value
Material	Ferrite N87
Geometry	RM14
Air gap	0.15 mm
Max energy stored in core $\mathcal{E}_{mag,max}$	6.3 mJ
Winding method	Segmented Discontinuous Side-by-side
Primary number of segments	1
Primary number of turns N_p	18
Primary inductance L_p	240.5 μ H
Primary leakage inductance L_{lp}	19.7 μ H
Primary winding capacitance C_p	8.6 nF
Primary winding resistance R_p	281 m Ω
Secondary number of segments	3
Secondary number of turns N_s	720
Secondary inductance L_s	420.9 mH
Secondary leakage inductance L_{ls}	34.7 mH
Secondary winding capacitance C_s	5.8 pF
Secondary winding resistance R_s	111.5 Ω
Inter-winding capacitance C_W	12.5 pF

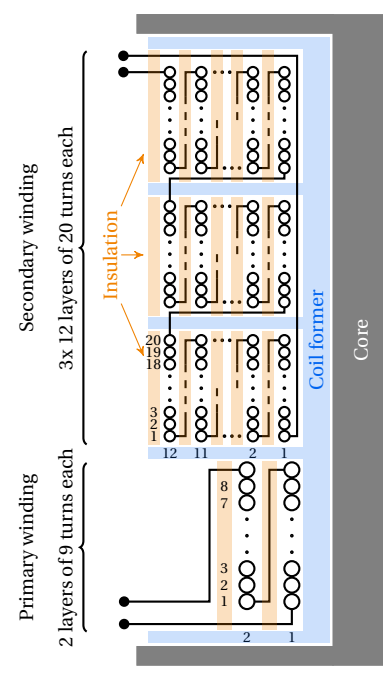


Table 3.6: Characteristics of the 8 kV flyback's coupled inductor.

Figure 3.16: Schematic of the cross section of the final coupled inductor manufactured showing the windings with the design recommendations listed previously.

3.4.4 Secondary diode

Finally, the last element to modify is the diode located on the secondary side of the system as its junction capacitance also influences the performances of the system when it starts blocking again during Step ④.

In our case, the diode was upgraded from a 5 kV diode R5000F from *Rectron Semiconductor* with a junction capacitance of 30 pF to a 12 kV diode HVEF12P from *Dean Technology* with a capacitance of 0.25 pF. Their respective relevant parameters are summarized in Table 3.7 below.

Name	V_{RRM} [V]	C_D [pF]	I_F [mA]	V_F [V]	Datasheet
R5000F	5 000	30	200	6.5	[52]
HVEF12P	12 000	0.25	20	27	[53]

Table 3.7: Specifications of the diodes used in the first and the improved flyback prototypes

3.5 Experimental results

With the aforementioned improvements made to the coupled inductor and the flyback in general, the performances of the system were significantly improved to allow the major achievement of being able to reliably provide voltages of at least 8 kV to a capacitive load.

Hereafter are presented various measurements obtained during the charge phase with the upgraded converter shown in Fig. 3.17 of which the specifications and components are listed in Table 3.8, and with a ceramic disc capacitor of a measured capacitance of 2.4 nF as a load.

Additionally, thanks to these measurements, an estimation of the overall efficiency could be undertaken.

Parameters	Value
Input voltage V_{in}	12 V
Output voltage V_{out}	0 - 8 kV
Load capacitance C_L	2.4 nF
Control strategy	Fixed frequency
M_p ON time $t_{p,on}$	130 μ s
Driving frequency f_{ch}	4 kHz
Charge time T_{ch}	8.75 ms

Components	Characteristics	Name
Primary MOSFET M_p	650 V, 30 A, $R_{DS,on} = 80$ m Ω	UJ3C065080T3S
Secondary diode D	12 kV, 0.2 A, $C_D = 0.25$ pF	HVEF12P
Coupled inductor	See Table 3.6	

Table 3.8: Specifications and main components of the 8 kV unidirectional flyback converter. The exact bill of materials and schematics can be found in Annexes A and B respectively.

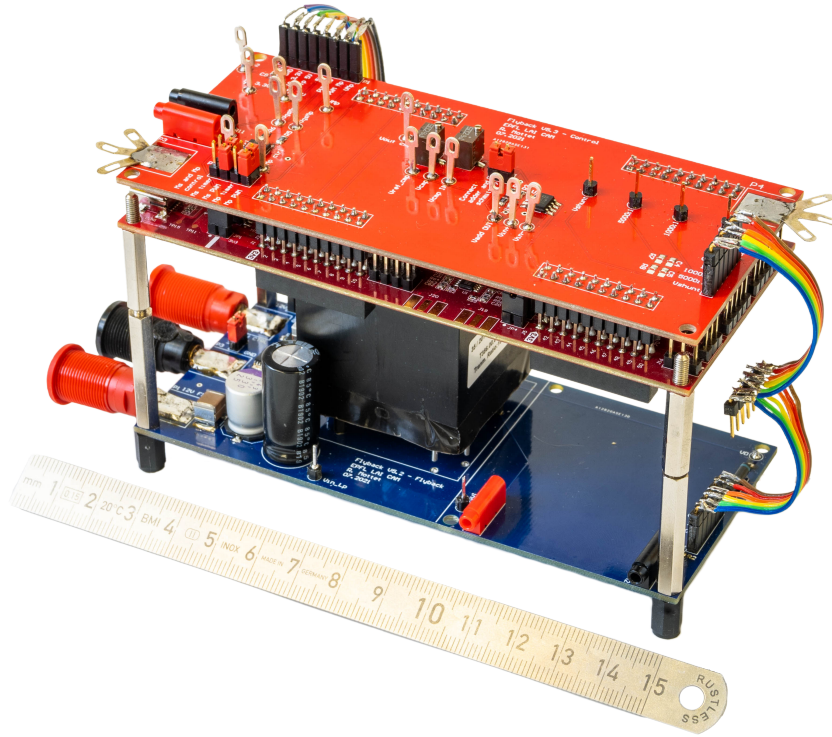


Figure 3.17: Photography of the manufactured 8kV unidirectional flyback converter.

3.5.1 General measurements

Figure 3.18 displays a schematic of the unidirectional flyback converter with the location of the measurement points and the devices used to obtain the various waveforms necessary to estimate the energy efficiency of the system and which are presented hereafter.

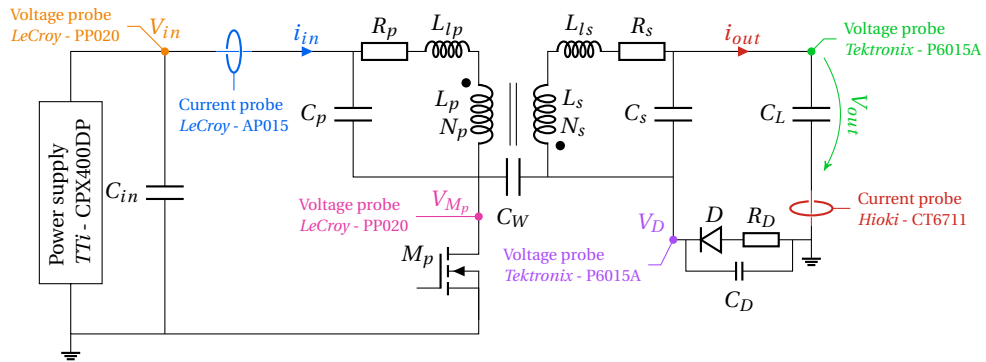


Figure 3.18: Schematic showing the location and devices used to measure the voltages and currents necessary to estimate the energy efficiency of the system.

Figure 3.19 displays the incremental increase of the output voltage across the capacitive load to 8kV. Additionally, the input voltage is also presented and is shown to be reasonably stable and constant throughout the charge phase despite the impulsive nature of the current drawn.

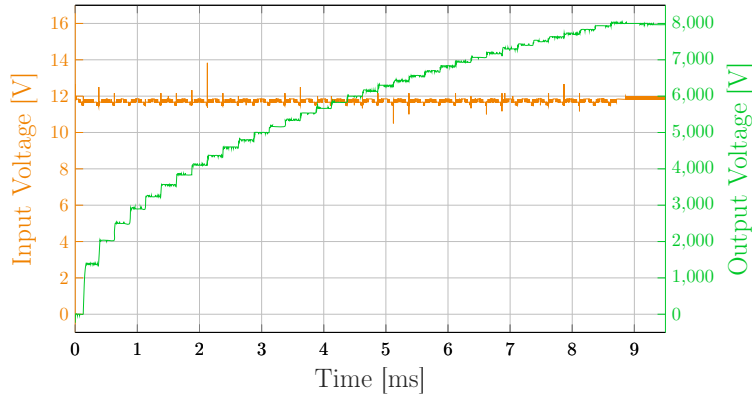


Figure 3.19: Measure of the input and output voltages during the operation of the unidirectional flyback converter. The output voltage was measured across a 2.4 nF ceramic disc capacitor and reaches 8 kV after 8.75 ms or 35 commutations of the primary switch.

Figure 3.20 presents the currents during the beginning and the end of the charge phase. The upper graph shows a great example of the change of the slope of the output current due to the increasing output voltage. In the lower one, one can observe, circled in orange, the first signs of the behavior discussed in Section 3.3 which are the negative current flows due to the parasitic capacitances of the components. They however remain very low considering the voltage levels at which they were measured when compared to the currents of Fig. 3.5. This tells us that the design considerations listed previously have been successful at improving the performances of the flyback and that the latter has far from reached its output voltage plateau. Meaning that the electronics has the potential to supply even higher voltages than currently achieved as shown in the following chapter.

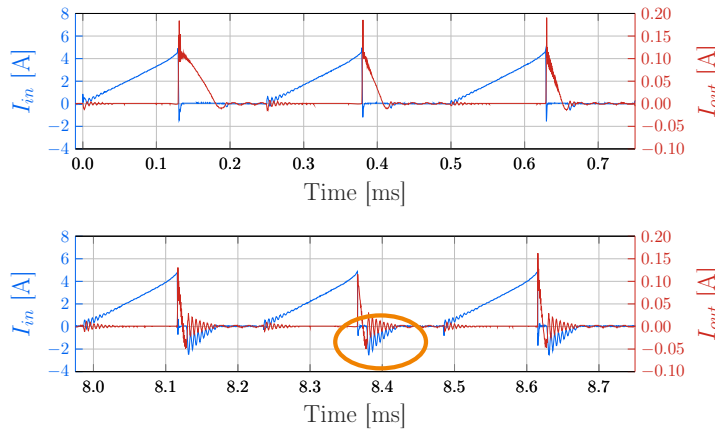


Figure 3.20: The top graph shows the waveforms of the input and output currents measured during the first 3 pulses of the charging phase. It also shows well the change of the output current's slope mentioned in Fig. 3.2. The bottom graph shows the same currents during the last 3 pulses. Circled are the first signs of parasitic negative currents. Behavior discussed in Section 3.3.1

Finally, Fig. 3.21 shows measurements of V_{M_p} the voltage across the primary MOSFET and V_D the voltage across the secondary diode. One can observe quite well on the first graph the voltage spikes across the primary MOSFET due to the leakage inductance of the coupled inductor. Also clearly visible is the increasing voltage across the switch while the secondary current flows which is due to the "transformer effect" of the coupled inductor which, in this case, mirrors the voltage across the secondary side to the primary side divided by the winding ratio. As for V_D , one can see the extreme variations that the related potential experiences as discussed in Section 3.3.3.

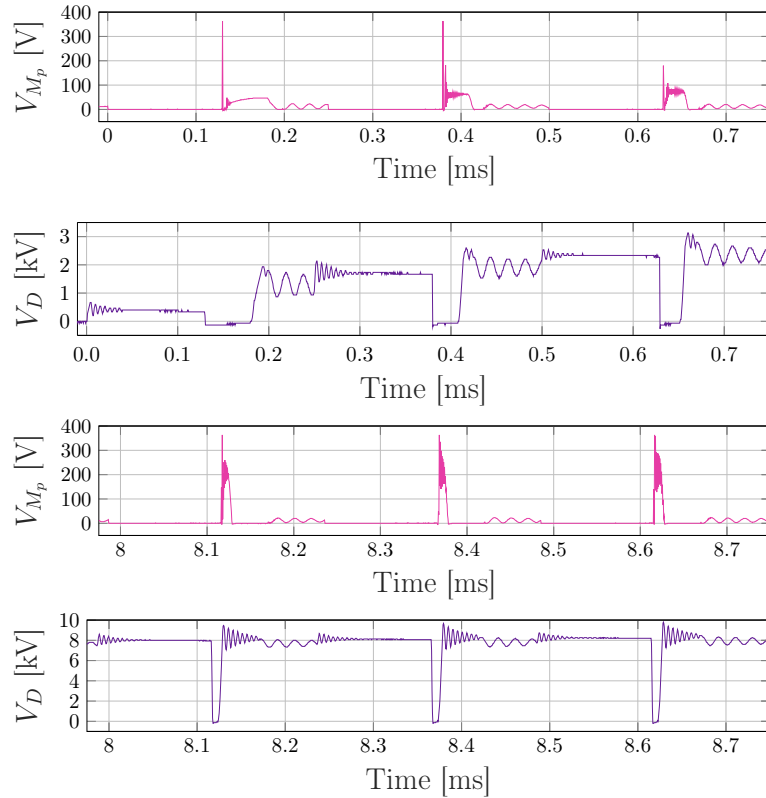


Figure 3.21: The first and second graphs show the waveforms of the voltage across the primary MOSFET and the diode respectively measured during the first 3 pulses of the charge phase. The third and fourth are the same voltages for the last 3 pulses.

3.5.2 Energy calculation procedure

To obtain the efficiency of the system, the energy absorbed or dissipated by each one of the major components and parasitic elements was calculated using the measurements presented in the previous section. Since these elements are not all actively absorbing or dissipating energy during the complete duration of a pulse, their respective influence was determined by calculating the difference of energy between the beginning and the end of each one of the steps defined in Section 3.3.3 for the relevant components.

For Step ①, the energy input into the system was obtained by computing the integral of the input current multiplied by the input voltage $\mathcal{E}_{in} = \int V_{in} \cdot I_{in} dt$. A portion of this energy is then dissipated by the resistance R_p of the primary winding of the coupled inductor as well as the ON-resistance R_{M_p} of the primary MOSFET. This energy dissipated was calculated using the integral of the respective resistance values multiplied by the input current squared i.e. $\mathcal{E}_{R_p} = \int R_p \cdot I_{in}^2 dt$ and $\mathcal{E}_{R_{M_p}} = \int R_{M_p} \cdot I_{in}^2 dt$. The energy lost due to the leakage inductance is obtained thanks to the energy equation $\mathcal{E}_{L_{lp}} = \frac{1}{2} L_{lp} \hat{I}_{in}^2$ with \hat{I}_{in} being the value of the current at its peak right at the end of the step.

During Step ② most of the energy dissipated is due to the commutation losses of the primary MOSFET. The value used was the one provided in the datasheet of the manufacturer.

Since Step ③ is the phase during which the current can finally flow freely through the diode, most of the energy lost during this phase is due to the resistive elements R_s – the secondary winding resistance – and R_D – the diode's forward resistance – for which the energy was calculated using $\mathcal{E}_{R_s} = \int R_s \cdot I_{out}^2 dt$ and $\mathcal{E}_{R_D} = \int R_D \cdot I_{out}^2 dt$ respectively. Additionally, it is also during this phase that the secondary parasitic capacitance C_s steals a portion of the energy destined to the load and is obtained with $\mathcal{E}_{C_s} = \frac{1}{2} C_s (V_{out} - V_D)^2$.

During Step ④, the parasitic capacitances C_W and C_D steal back a portion of the energy stored in the load, thus creating the negative current flow. This stolen energy is calculated with $\mathcal{E}_{C_W} = \frac{1}{2} C_W (V_D - V_{M_p})^2$ and $\mathcal{E}_{C_D} = \frac{1}{2} C_D V_D^2$. The resulting negative current flow implies that energy is sent back through the coupled inductor and which can be computed using $\mathcal{E}_{L_s} = \frac{1}{2} L_s \hat{I}_{out}^2$ and with $\mathcal{E}_{L_{ls}} = \frac{1}{2} L_{ls} \hat{I}_{out}^2$ for the accompanying leakage losses where \hat{I}_{out} is the peak value of the negative current.

As for Step ⑤, a part of the induced primary current is further dissipated through the primary resistances and the rest is recovered by the input power supply. The latter reduces the overall energy consumed by the system.

Finally, with Step ⑥ and the system achieving equilibrium, it is possible to determine how much energy ultimately ends up in the load by using $\mathcal{E}_{C_L} = \frac{1}{2} C_L V_{out}^2$.

Figures 3.22 and 3.23 present the evolution of the aforementioned energies during the first and last pulses of the charge phase respectively. In Fig 3.23 one can clearly see the partial energy recovery due to the induced primary current of Step ⑤.

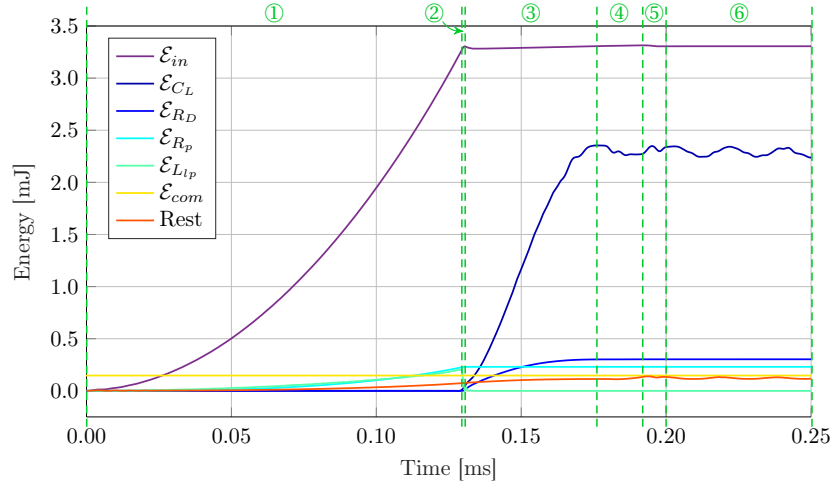


Figure 3.22: Evolution of the energy stored or dissipated by the various elements of the flyback during the first pulse of the charge phase. The rest is the sum of the energy stored or dissipated in C_s , C_D , C_W , R_{Mp} , R_s , L_{ls} and the core losses.

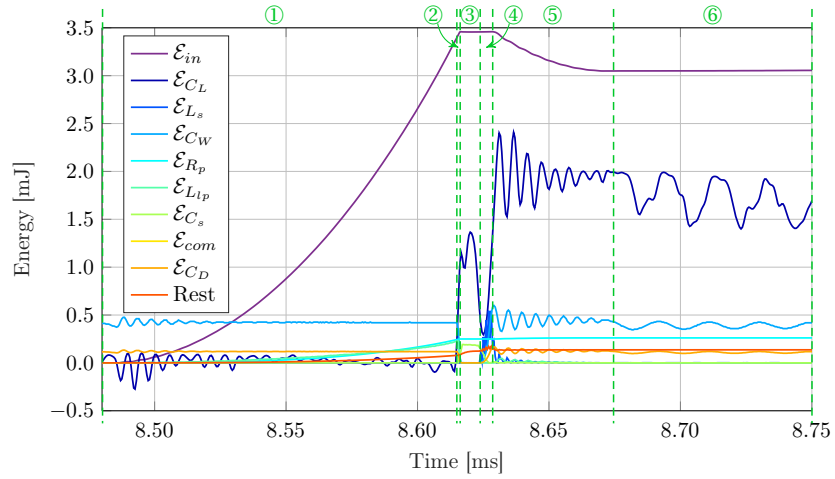


Figure 3.23: Evolution of the energy stored or dissipated by the various elements of the flyback during the last pulse of the charge phase. The rest is the sum of the energy stored or dissipated in R_{Mp} , R_D , L_{LS} and the core losses.

3.5.3 Efficiency estimation

Figures 3.24 and 3.25 present the evolution of the distribution of the energy throughout the system during the first and last – at 8 kV – pulses of energy during the charge phase.

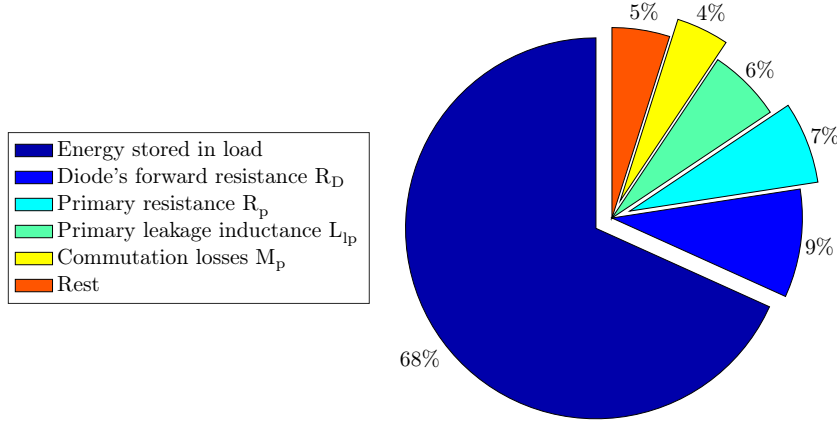


Figure 3.24: Distribution of the energy originating from the power supply throughout the system during the first pulse of the charge phase. The rest includes the energy stored or dissipated in C_s , C_D , C_W , R_{M_p} , R_s , L_s , L_{ls} and the core losses.

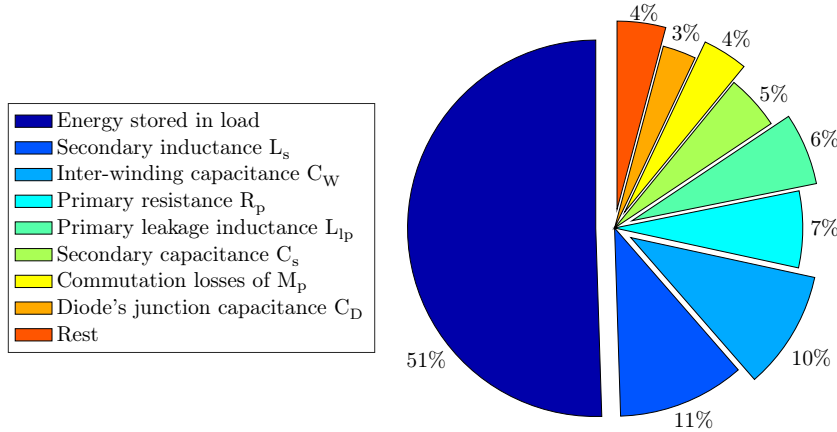


Figure 3.25: Distribution of the energy throughout the system during the last pulse of the charge phase with an output voltage of 8 kV. The rest includes the energy stored or dissipated in R_{M_p} , R_D , L_{LS} and the core losses.

One can observe that, during the charge phase and regardless of the output voltage, 17% of the energy coming from V_{in} is already lost on the primary side due to the commutation losses of M_p , the resistance of the winding and the leakage inductance. Additionally, on the secondary side, while the output voltage remains low as is the case for Fig. 3.24, the losses are also essentially due the resistive elements – here mainly the diode's forward resistance – because of the larger output current density as shown in the top graph of Fig. 3.20.

Conversely, when the output voltage is high (Fig. 3.25), the losses due to the capacitive parasitic elements and resulting back-flow current become more and more important as expected. This data shows that, while reducing the parasitic capacitances greatly improves the ability of the flyback to supply higher voltages, improvements shall be made on the primary side – on the leakage inductance in particular – in order to further improve the overall efficiency of the system.

In the end, over the 8.75 ms of the charge phase an average of approximately 60% of the energy originating from the power supply ends in the capacitive load. While this efficiency may seem low when compared to the 89% obtained in [38], one has to remember the fact that the voltage levels manipulated in Thummala's work are significantly lower and that the design of his coupled inductor was not as drastically oriented towards minimizing its parasitic capacitances, which was done to the detriment of the inductor's leakage and thus to some of the efficiency.

3.6 Conclusion

In this chapter, it was demonstrated that a design reducing key parasitic capacitances of the coupled inductor allowed the flyback converter to supply 8 kV to a capacitive load – more than three times what was previously achieved in the literature – from a 12 V power supply. The load, a capacitor of 2.4 nF, was charged in less than 9 ms.

Design considerations such as a segmented discontinuous winding method to reduce the inter-layer capacitance and of a side-by-side method to reduce the inter-winding capacitance have been implemented. Additionally, options to increase the amount of energy stored in the coupled inductor through the use of cores with distributed air gaps are proposed with the caveat that, although such cores may possess more attracting magnetic properties, they make the winding manufacture significantly more complex due to their toroid geometry.

The parasitic capacitances have been reduced through the control of the winding in a conventional RM core. With this improved design, parasitic capacitances no longer limit the output voltage and their effect on the efficiency reduction is limited, giving access to an average charge efficiency of 60%.

Nonetheless, the results obtained here also revealed opportunities for further improvements. Regarding the physical size of the system, further reducing the size of the coupled inductor will be critical to make the heart pump system more portable. However, this parameter is highly dependent of the characteristics of the load itself and of the voltage rise time required. Indeed, the capacitance of the load dictates how much energy is required to reach a certain voltage, thus how many pulses are necessary and consequently of fast the output voltage will rise. Furthermore, the access resistance of a DEA will dissipate additional energy, worsening the energy efficiency and thus limiting how high the voltage will be able to go.

Ultimately, to find the smallest size possible, an optimization of the complete system should be undertaken which maximizes the energy stored in the coupled inductor and minimizes its size while taking into account the capacitance and access resistance of the load as well as the maximal output voltage rise time tolerated.

As for the efficiency of the system, the resistive elements and the leakage inductance of the primary side revealed themselves to be the source of a large amount of losses. The latter being inversely related to the parasitic capacitances, a topology optimization procedure could be undertaken over the winding topology as well as the core geometry to find the optimal balance between these two parasitic elements. This could also help reduce the size of the coupled inductor.

Publications related to this chapter :

R. Mottet, M. Almanza, L. Pniak, A. Boegli and Y. Perriard, "*Ultra-High-Voltage (7-kV) Bidirectional Flyback Converter Used to Drive Capacitive Actuators*," in IEEE Transactions on Industry Applications, vol. 57, no. 5, pp. 5145-5156, Sept.-Oct. 2021, doi: 10.1109/TIA.2021.3094460.

R. Mottet, M. Almanza, A. Boegli and Y. Perriard, "*Critical Parasitic Elements of Coupled Inductors for Ultra-High Voltage Flyback Converters Used to Drive Capacitive Actuators*," in 2019 22nd IEEE International Conference on Electrical Machines and Systems (ICEMS), 2019, pp. 1-5, doi: 10.1109/ICEMS.2019.8921772. **Awarded best paper at the conference.**

4 Analytical model of the charge phase

4.1 Introduction

In order to provide a first building block for the implementation of the optimization processes recommended at the end of Chapter 3, an analytical model was elaborated to represent the working principles of the electronics during the charge phase.

Other than its potential for optimization purposes, this model already helped reveal and confirm how influential each of the parasitic capacitances were regarding the performances of the system. Thus, thanks to this model, an estimation of the absolute maximal output voltage theoretically reachable with the latest prototype could be obtained.

4.2 Model schematic and procedure

In this chapter, the focus is solely on the charge phase during which the output voltage increases across a basic capacitive load by considering the unidirectional flyback presented in Fig. 4.1.

As mentioned previously, this charge phase is characterized by a succession of pulses of energy sent from an input power supply $u_{in}(t)$ towards the load C_L through a coupled inductor which gradually increase the voltage $u_{out}(t)$. Similarly to what was done in Section 3.3, each pulse was further divided into only 5 major steps (compared to 6 previously, for the sake of simplicity as one of them is negligible) which are linked to the existence of currents (or absence thereof) in parts of the circuit as well as their direction. Fig. 4.2 showcases actual measurements of the currents obtained with the 8 kV flyback and displays the aforementioned steps.

During step ①, M_p is closed which allows the primary current i_{in} to flow and gradually increase as it loads the coupled inductor with magnetic energy.

Step ② starts as soon as M_p reopens. Consequently, the energy stored is released in the form of a current i_{out} flowing towards the load which will increase the voltage across it.

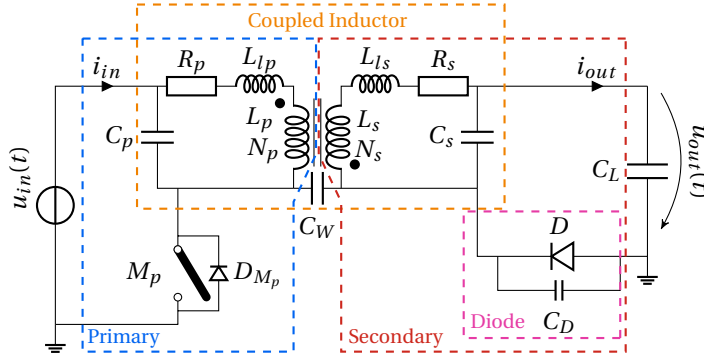


Figure 4.1: Schematic of the circuit considered for the analytical model. The switch M_p is considered ideal as well as the diode D . However, for the former, its body diode D_{M_p} is also included and considered ideal, as for the latter, its junction capacitance C_D is included. C_p represents the inter-layer capacitance of the winding, R_p the wire resistance, L_{lp} the leakage inductance, and N_p the number of turns of the primary side of the coupled inductor. The same elements are considered for the secondary side. C_w is the inter-winding parasitic capacitance.

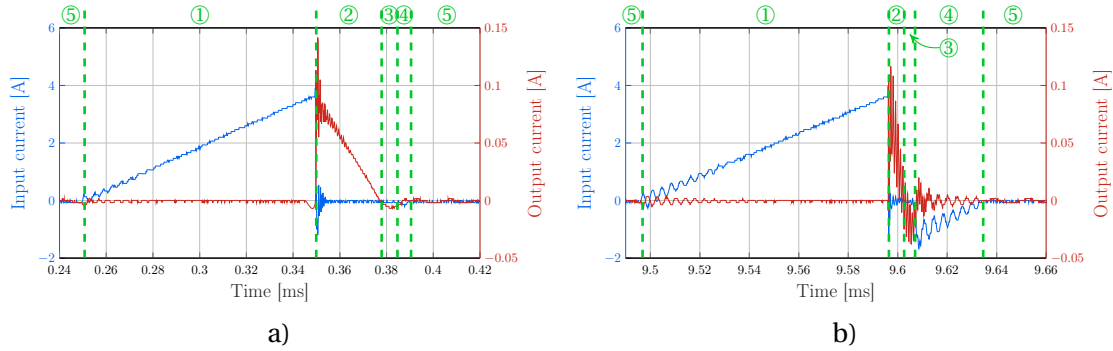


Figure 4.2: Primary and secondary currents flowing during a) a pulse of energy when $V_{o,1} = 1.1 \text{ kV}$ and b) a pulse when $V_{o,1} = 6.9 \text{ kV}$. The 5 steps described are identified for both a) and b). One can notice that the output current varies with the output voltage as shown further below.

Step ③ begins when i_{out} crosses the 0 A line. This step is the most critical one regarding the influence of the parasitic capacitive elements. Indeed, as soon as i_{out} becomes negative, the diode starts blocking which should stop the current. However, it was observed that a negative current continues to flow regardless. As a side consequence, this negative current charges the coupled inductor with magnetic energy.

Step ④ exists because this magnetic energy stored in the coupled inductor is released back towards the power supply as soon as the body diode of M_p starts conducting which happens when the slope of $i_{out}(t)$ changes in polarity thus inverting the voltage across the coupled inductor. This behavior is very similar to what happens between steps 1 and 2.

Step ⑤ is simply the resting state where no current is flowing in the converter until the start of the next pulse.

4.3 Step 1 - Primary current

During this step, the current of interest is the current i_L as it is the one effectively charging with energy the coupled inductor. This current starts to flow when M_p closes and increases while charging the inductance. During this time, no secondary current is flowing. In Fig. 4.3, the relevant components considered to determine the analytical equation of i_L during this step are highlighted. Underneath, the equations in the time domain for each highlighted component are given as well as their Laplace equivalent. Since M_p is considered as ideal, the act of closing it creates a step function of amplitude V_{in} across the RLC circuit. It is represented as such by (4.1).

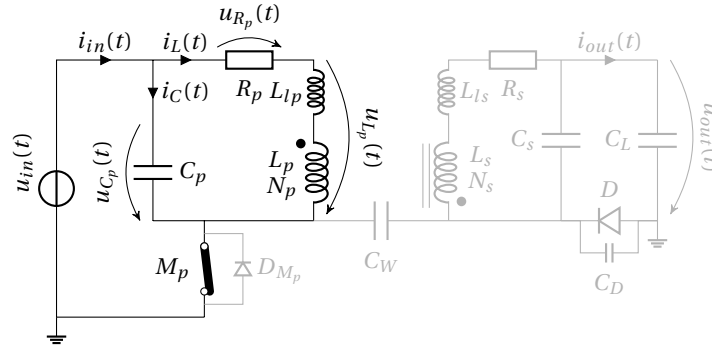


Figure 4.3: Highlighted are the elements considered to obtain the analytical equation of the primary current.

$$u_{in}(t) = V_{in} \quad \circ \bullet U_{in}(s) = \frac{V_{in}}{s} \quad (4.1)$$

$$u_{C_p}(t) = \frac{1}{C_p} \int_0^t i_C(\tau) d\tau \quad \circ \bullet U_{C_p}(s) = \frac{1}{sC_p} I_C(s) \quad (4.2)$$

$$u_{R_p}(t) = R_p i_L(t) \quad \circ \bullet U_{R_p}(s) = R_p I_L(s) \quad (4.3)$$

$$u_{L_p}(t) = (L_p + L_{lp}) \frac{di_L(t)}{dt} \quad \circ \bullet U_{L_p}(s) = (L_p + L_{lp})(sI_L(s) - i_L(0)) \quad (4.4)$$

$$i_{in}(t) = i_C(t) + i_L(t) \quad \circ \bullet I_{in}(s) = I_C(s) + I_L(s) \quad (4.5)$$

4.3.1 Analytical solution

Let us first define the initial conditions of the system. Regarding C_p , we consider it to be empty and thus it has an initial voltage of 0V. Similarly for the $i_L(0)$ in (4.4), no current is flowing in the converter thus $i_L(0) = 0$.

Solving the equation system using Kirchhoff's law, we have at the end

$$\begin{aligned} I_L(s) &= V_{in} \frac{1}{s(R_p + s(L_p + L_{lp}))} \\ &= \frac{V_{in}}{R_p} \frac{R_p / (L_p + L_{lp})}{s(s + R_p / (L_p + L_{lp}))} \end{aligned} \quad (4.6)$$

Chapter 4. Analytical model of the charge phase

It can be observed that $I_L(s)$ is in the form $F(s) = \frac{\alpha}{s(s+\alpha)}$ with $\alpha = \frac{R_p}{L_p+L_{lp}}$ which is the Laplace transform of the function $f(t) = (1 - e^{-\alpha t})$. Thus, we can obtain $i_L(t)$, the inverse Laplace function of $I_L(s)$ such that:

$$i_L(t) = \frac{V_{in}}{R_p} (1 - e^{-\frac{R_p}{L_p+L_{lp}} t}) \quad (4.7)$$

4.4 Step 2 - Secondary current

As mentioned above, this step starts when M_p reopens and the energy stored in the coupled inductor is released through the generation of the secondary current $i_{out}(t)$. Fig. 4.4 shows the relevant components considered for this step and on the right the equations in the time and Laplace domains. Here, C_W and C_D are not considered because the voltage $u_D(t)$ is equal to 0V since the diode is considered as ideal.

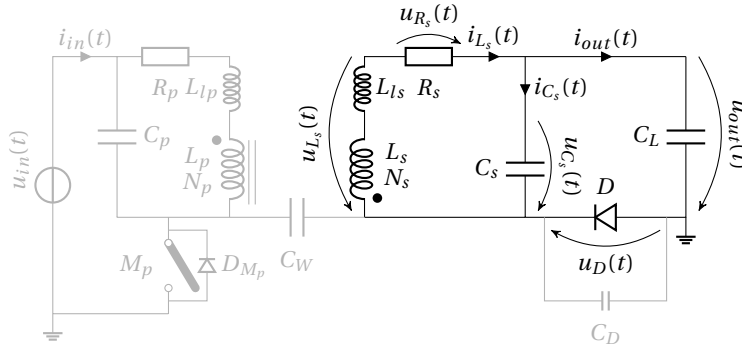


Figure 4.4: Highlighted are the elements considered to obtain the analytical equation of the secondary current $i_{out}(t)$.

$$u_{out}(t) = V_{o,1} + \frac{1}{C_L} \int_0^t i_{out}(\tau) d\tau \quad \longleftrightarrow \quad U_{out}(s) = \frac{V_{o,1}}{s} + \frac{1}{sC_L} I_{out}(s) \quad (4.8)$$

$$u_{C_s}(t) = V_{o,1} + \frac{1}{C_s} \int_0^t i_{C_s}(\tau) d\tau \quad \longleftrightarrow \quad U_{C_s}(s) = \frac{V_{o,1}}{s} + \frac{1}{sC_s} I_{C_s}(s) \quad (4.9)$$

$$u_{R_s}(t) = R_s i_{L_s}(t) \quad \longleftrightarrow \quad U_{R_s}(s) = R_s I_{L_s}(s) \quad (4.10)$$

$$u_{L_s}(t) = -(L_s + L_{ls}) \frac{di_{L_s}(t)}{dt} \quad \longleftrightarrow \quad U_{L_s}(s) = -(L_s + L_{ls})(sI_{L_s}(s) - i_{L_s}(0)) \quad (4.11)$$

$$i_{L_s}(t) = i_{out}(t) + i_{C_s}(t) \quad \longleftrightarrow \quad I_{L_s}(s) = I_{out}(s) + I_{C_s}(s) \quad (4.12)$$

$$u_D(t) = 0 \quad \longleftrightarrow \quad U_D(s) = 0 \quad (4.13)$$

4.4.1 Analytical solution

Regarding the initial conditions, in (4.8) and (4.9), $V_{o,1}$ is the value of the output voltage at the end of Step 1. Similarly for (4.11), $i_{L_s}(0) = \hat{i}_{in,1}/N_r$ where $\hat{i}_{in,1}$ is the peak value of the primary current at the end of Step 1 and $N_r = N_s/N_p$ is the turns ratio of the coupled inductor. Additionally, since $U_D(s) = 0$, we can consider that C_s and C_L are in parallel to one another.

Solving the equations system, we get

$$I_{out}(s) = \frac{i_{L_s}(0)(L_s + L_{ls})C_L}{(L_s + L_{ls})(C_s + C_L)} \cdot s \cdot \frac{1}{\frac{1}{(L_s + L_{ls})(C_s + C_L)} + s \frac{R_s}{(L_s + L_{ls})} + s^2} - \frac{V_{o,1}C_L}{(L_s + L_{ls})(C_s + C_L)} \frac{1}{\frac{1}{(L_s + L_{ls})(C_s + C_L)} + s \frac{R_s}{(L_s + L_{ls})} + s^2} \quad (4.14)$$

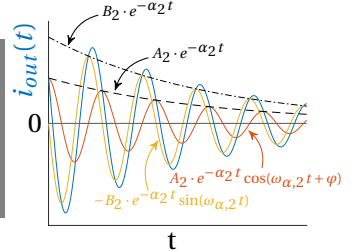
Let us now say that $\omega_{0,2} = \frac{1}{\sqrt{(L_s + L_{ls})(C_L + C_s)}}$, $\alpha_2 = \frac{R_s}{2(L_s + L_{ls})}$, and $\omega_{\alpha,2} = \sqrt{\omega_{0,2}^2 - \alpha_2^2}$.

Therefore

$$I_{out}(s) = \frac{i_{L_s}(0)C_L}{\omega_{\alpha,2}(C_s + C_L)} \cdot s \cdot \frac{\omega_{\alpha,2}}{\omega_{\alpha,2}^2 + (s + \alpha_2)^2} - \frac{V_{o,1}C_L}{\omega_{\alpha,2}(L_s + L_{ls})(C_s + C_L)} \cdot \frac{\omega_{\alpha,2}}{\omega_{\alpha,2}^2 + (s + \alpha_2)^2} \quad (4.15)$$

•
○

$$i_{out}(t) = A_2 \cdot e^{-\alpha_2 t} \cos(\omega_{\alpha,2} t + \varphi) - B_2 \cdot e^{-\alpha_2 t} \sin(\omega_{\alpha,2} t) \quad (4.16)$$



where $A_2 = \sqrt{\omega_{\alpha,2}^2 + (-\alpha_2)^2} \cdot \frac{C_L}{(C_L + C_s)} \frac{i_{L_s}(0)}{\omega_{\alpha,2}}$, $B_2 = \frac{V_{o,1}C_L}{(L_s + L_{ls})(C_L + C_s)\omega_{\alpha,2}}$ and $\varphi = \arctan\left(\frac{\alpha_2}{\omega_{\alpha,2}}\right)$.

4.5 Step 3 - Reverse output current

As soon as the output current drops below 0 A, the current should be blocked by the diode. However, experiments showed that a current continues to flow regardless. This is due to the fact that the parasitic capacitances C_D and C_W must store enough energy for the voltage across them to rise to the same level as the output voltage. The solution of the following equation system confirms that the existence of these capacitances explains this reverse flow of current.

Fig. 4.5 once again shows the circuit with the relevant elements and on the right the corresponding equations in the time and Laplace domains.

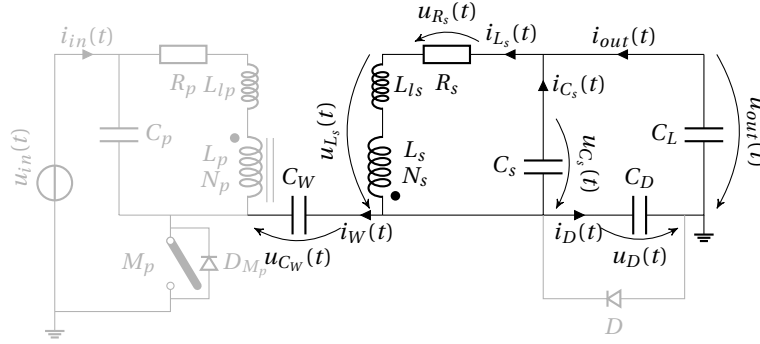


Figure 4.5: Highlighted are the elements considered to obtain the analytical equation of the reversing secondary current $i_{out}(t)$.

$$u_{out}(t) = V_{o,2} - \frac{1}{C_L} \int_0^t i_{out}(\tau) d\tau \quad \circ \bullet U_{out}(s) = \frac{V_{o,2}}{s} - \frac{1}{sC_L} I_{out}(s) \quad (4.17)$$

$$u_{C_s}(t) = V_{o,2} - \frac{1}{C_s} \int_0^t i_{C_s}(\tau) d\tau \quad \circ \bullet U_{C_s}(s) = \frac{V_{o,2}}{s} - \frac{1}{sC_s} I_{C_s}(s) \quad (4.18)$$

$$u_{R_s}(t) = R_s i_{L_s}(t) \quad \circ \bullet U_{R_s}(s) = R_s I_{L_s}(s) \quad (4.19)$$

$$u_{L_s}(t) = (L_s + L_{ls}) \frac{di_{L_s}(t)}{dt} \quad \circ \bullet U_{L_s}(s) = (L_s + L_{ls})(sI_{L_s}(s) - i_{L_s}(0)) \quad (4.20)$$

$$u_{C_D}(t) = \frac{1}{C_D} \int_0^t i_D(\tau) d\tau \quad \circ \bullet U_{C_D}(s) = \frac{1}{sC_D} I_D(s) \quad (4.21)$$

$$u_{C_W}(t) = \frac{1}{C_W} \int_0^t i_W(\tau) d\tau \quad \circ \bullet U_{C_W}(s) = \frac{1}{sC_W} I_W(s) \quad (4.22)$$

$$i_{L_s}(t) = i_{out}(t) + i_{C_s}(t) \quad \circ \bullet I_{L_s}(s) = I_{out}(s) + I_{C_s}(s) \quad (4.23)$$

$$i_{out}(t) = i_W(t) + i_D(t) \quad \circ \bullet I_{out}(s) = I_W(s) + I_D(s) \quad (4.24)$$

4.5.1 Analytical solution

For this step, the initial conditions are $V_{o,2}$ the voltage across the load at the end of Step 2. Whereas $i_{L_s}(0) = 0$ since the step start precisely when the current is equal to 0 A.

Let us first consider that C_W and C_D are parallel to one another. This simplification was done because the voltage $u_{in}(t)$ is constant and its amplitude is negligible compared to that of $u_{C_W}(t)$ and $u_{C_D}(t)$.

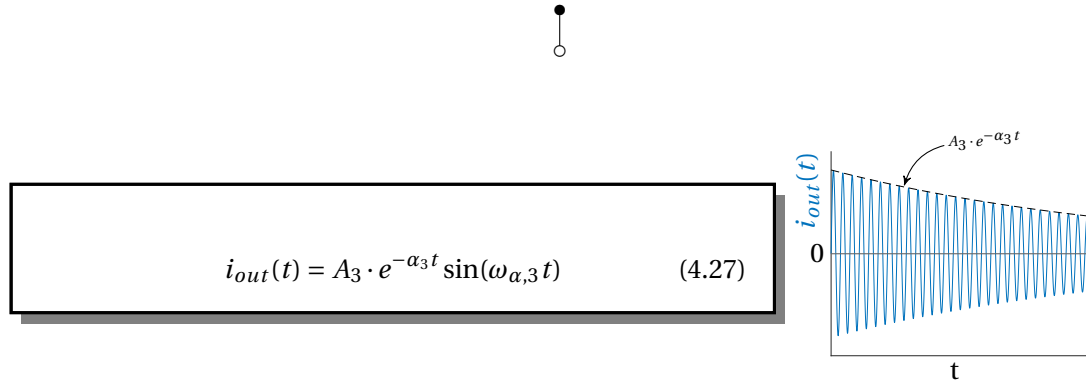
With this simplification, the solution of the equation system becomes

$$I_{out}(s) = \frac{V_{o,2} C_L (C_W + C_D)}{(L_s + L_{ls}) (C_L C_s + C_L (C_W + C_D) + C_s (C_W + C_D))} \cdot \frac{1}{s^2 + s \frac{R_s}{L_s + L_{ls}} + \frac{C_L + C_W + C_D}{(L_s + L_{ls}) (C_L C_s + C_L (C_W + C_D) + C_s (C_W + C_D))}} \quad (4.25)$$

4.6 Step 4 - Induced primary current

Rearranging the terms such that $\omega_{\alpha,3} = \sqrt{\frac{C_L + C_W + C_D}{(L_s + L_{ls})(C_L C_s + C_L(C_W + C_D) + C_s(C_W + C_D))} - \alpha_3^2}$ and $\alpha_3 = \frac{R_s}{2(L_s + L_{ls})}$, we get

$$I_{out}(s) = \frac{V_{o,2} C_L (C_W + C_D)}{(L_s + L_{ls})(C_L C_s + C_L(C_W + C_D) + C_s(C_W + C_D))} \cdot \frac{1}{\omega_{\alpha,3}} \cdot \frac{\omega_{\alpha,3}}{(s + \alpha_3)^2 + \omega_{\alpha,3}^2} \quad (4.26)$$



with $A_3 = \frac{C_L(C_W + C_D)}{(L_s + L_{ls})(C_L C_s + C_L(C_W + C_D) + C_s(C_W + C_D))} \cdot \frac{V_{o,2}}{\omega_{\alpha,3}}$.

4.6 Step 4 - Induced primary current

Due to the reverse output current of Step 3, the coupled inductor is loaded with magnetic energy by said output current in a similar way as during the first step. This energy is subsequently released back towards the input power supply through the generation of an input current.

The circuit of the relevant elements considered is shown in Fig. 4.6 and on the right the equations in the time and Laplace domains.

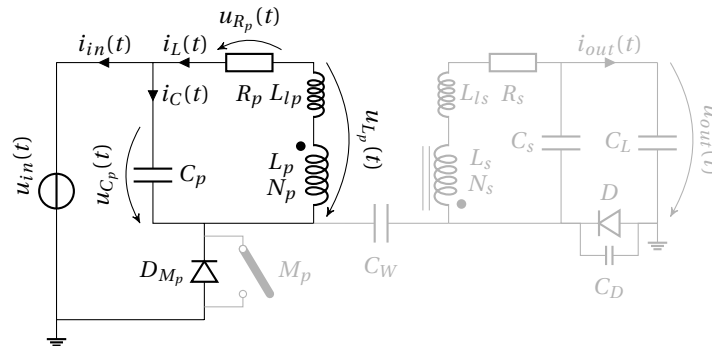


Figure 4.6: Highlighted are the elements considered to obtain the analytical equation of the induced primary current.

$$u_{in}(t) = V_{in} \quad \circ \text{---} \bullet U_{in}(s) = \frac{V_{in}}{s} \quad (4.28)$$

$$u_{C_p}(t) = \frac{1}{C_p} \int_0^t i_C(\tau) d\tau \quad \circ \text{---} \bullet U_{C_p}(s) = \frac{1}{sC_p} I_C(s) \quad (4.29)$$

$$u_{R_p}(t) = R_p i_L(t) \quad \circ \text{---} \bullet U_{R_p}(s) = R_p I_L(s) \quad (4.30)$$

$$u_{L_p}(t) = -(L_p + L_{lp}) \frac{di_L(t)}{dt} \quad \circ \text{---} \bullet U_{L_p}(s) = -(L_p + L_{lp})(sI_L(s) - i_L(0)) \quad (4.31)$$

$$i_{in}(t) = i_L(t) - i_C(t) \quad \circ \text{---} \bullet I_{in}(s) = I_L(s) - I_C(s) \quad (4.32)$$

4.6.1 Analytical solution

The initial conditions of the step only concern the current $i_L(t)$ for which $i_L(0) = \hat{i}_{out,3} \cdot N_r$ with $\hat{i}_{out,3}$ the peak value of the reverse output current of Step 3.

To solve this equation system, we can say that

$$U_{in}(s) = U_{L_p}(s) - U_{R_p}(s) \quad (4.33)$$

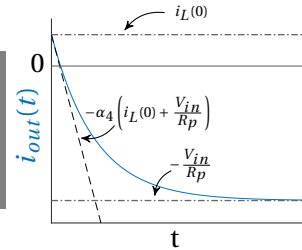
$$\Rightarrow \frac{V_{in}}{s} = -(L_p + L_{lp})(sI_L(s) - i_L(0)) - R_p I_L(s) \quad (4.34)$$

From there, we can find the equation for the primary current $I_L(s)$

$$I_L(s) = i_L(0) \frac{1}{s + \frac{R_p}{L_p + L_{lp}}} - \frac{V_{in}}{R_p} \cdot \frac{\frac{R_p}{L_p + L_{lp}}}{s(s + \frac{R_p}{L_p + L_{lp}})} \quad (4.35)$$



$$i_L(t) = i_L(0) \cdot e^{-\alpha_4 t} - \frac{V_{in}}{R_p} (1 - e^{-\alpha_4 t}) \quad (4.36)$$



with $\alpha_4 = \frac{R_p}{L_p + L_{lp}}$.

4.7 Comparison with measurements

To validate the analytical model for each step, the measurements presented in Fig. 4.2 were superimposed with the equations of each step and shown in Fig. 4.7. The values of the various parameters of the equations correspond to the ones of the manufactured flyback, the HV diode and the load used to obtain said measurements and can be found in Table 3.6.

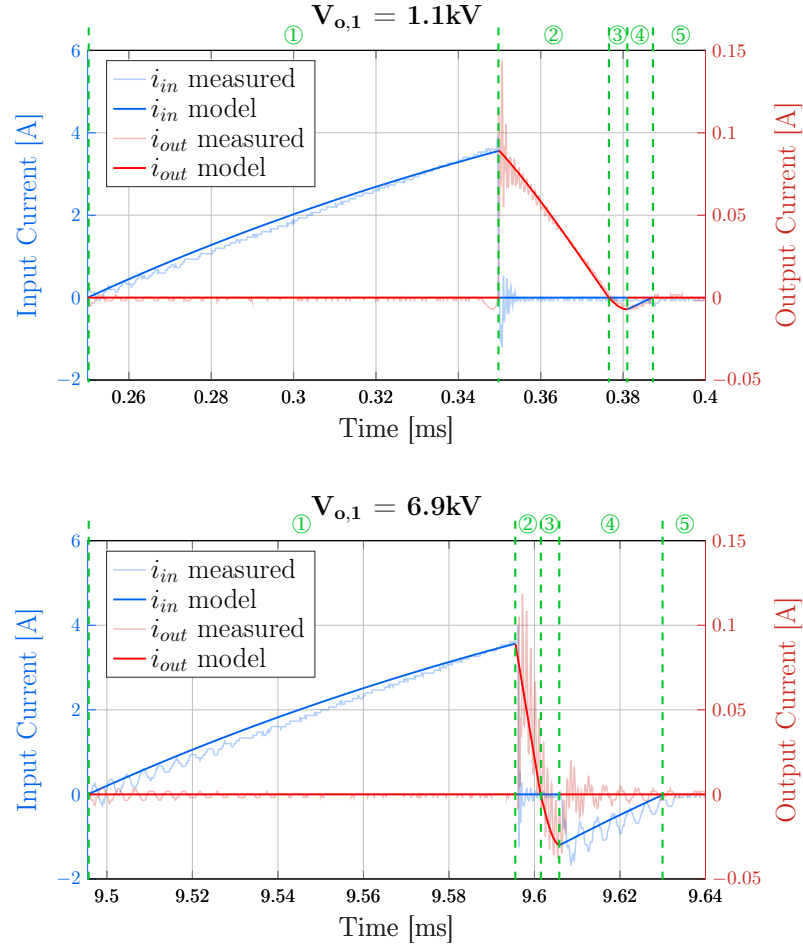


Figure 4.7: Superimposition of the analytical equations over measurements obtained with a homemade flyback converter during two different pulses of energy. On the top, $V_{o,1} = 1.1\text{kV}$ and, on the bottom, $V_{o,1} = 6.9\text{kV}$. The characteristics of the components are given in Table 3.6.

We can observe that the obtained equations fit very well the measurements and thus describe well the behavior of the currents during a single pulse of energy, regardless of the output voltage currently existing across the capacitive load.

However, certain discrepancies can be seen such as the high frequency oscillations measured on both the input and output currents. Those oscillations originate most certainly from the semiconductor components (M_p and D) when they are commutating as they were considered ideal.

4.7.1 Estimation of the maximum output voltage reachable

With the equations of the currents now defined, it is possible to evaluate how much the output voltage varies with each pulse as well as the theoretical absolute maximum a given flyback should be capable to reach.

This evaluation can be done by working with equations (4.8) and (4.17) and computing sequentially for each pulse the output voltage while adding each result to the previous one. Fig 4.8 presents the result of such a process after hundreds of pulses clearly showing the asymptotic nature of the output voltage plateauing at nearly 12 kV in our case. Fig. 4.9 displays a zoom where the evaluated model is superimposed with measurement confirming the good fitting of the model.

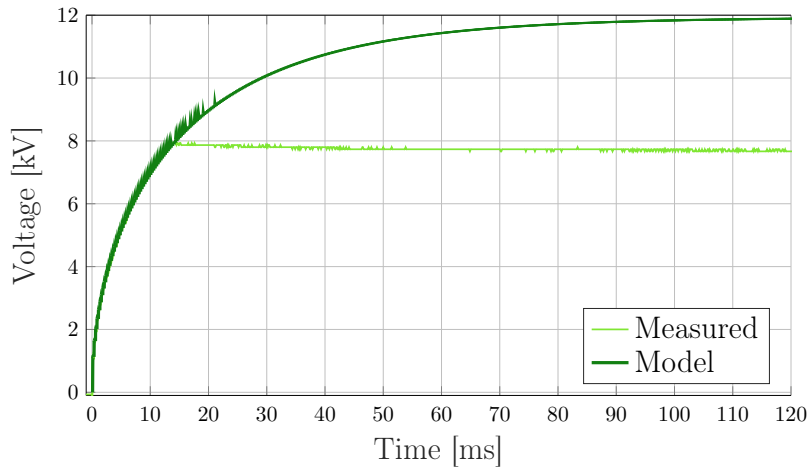


Figure 4.8: Evaluated analytical model over measurements of the output voltage. From the model, one can expect the converter to reach a plateau at around 12 kV.

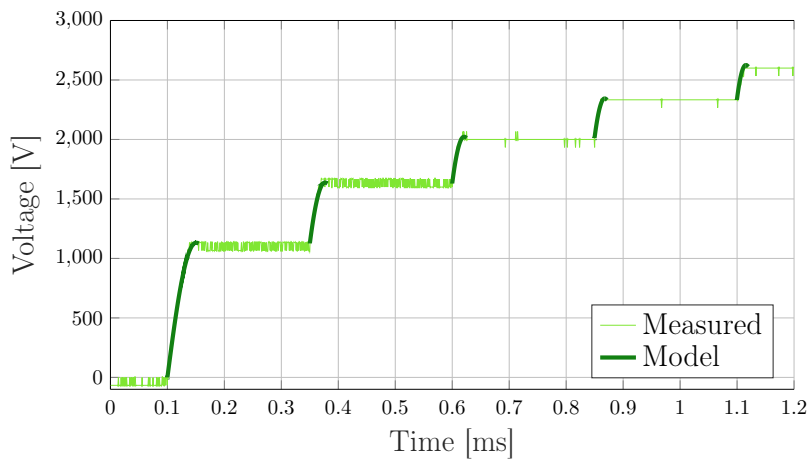


Figure 4.9: Zoom of the model superimposed over measurements over the duration of the first 5 pulses of energy.

4.8 Conclusion

This chapter presents the mathematical development undertaken to obtain the analytical equations depicting the transient input and output currents flowing through the ultra-high voltage flyback converter for each of the steps that compose an energy pulse when the flyback is used to charge an ideal capacitive load.

By superimposing the numerical evaluation of the equations using the characteristics of a given flyback over measurements obtained with said manufactured flyback, the validity of the model could be confirmed as it displayed an excellent fit between both waveforms. Additionally, thanks to this model, the theoretical absolute maximum voltage plateau that the tested flyback could supposedly reach was calculated and was determined to be of around 12 kV. Thus showing that the manufactured flyback has far from reached its full potential in regards to the output voltage it can supply.

Therefore, this means that the resulting analytical model not only confirms the assumptions made in the previous chapter that the capacitive parasitic elements C_D , C_s and C_W are the main culprits behind the flyback's limited ability to supply extremely high output voltages but it also provides a definitive way to estimate the influence of each one of them separately.

Ultimately, this model is the first stepping stone to enable further optimization of the converter to allow it to supply even higher voltages with enhanced efficiency. From the work presented here, several leads could be followed to improve the performances and reliability of the system. A first one could be the further development of this model including more complex models for the load to better represent Dielectric Elastomer Actuators which could help better understand their behaviors when faced with impulsive currents.

A second lead could be to make this model work in conjunction with optimization processes such as topology optimization applied to the winding of the coupled inductor to find the optimal minimum between the leakage inductances and the parasitic capacitances so that the output voltage is maximized with minimal amounts of losses due to the leakage.

And finally, the work made for this model could also help for the control aspect of the flyback by potentially removing the need for a voltage probe across the output providing feedback to the controller, thus reducing the complexity of the system and further losses.

Publications related to this chapter :

R. Mottet, A. Boegli and Y. Perriard, *"An Analytical Model for the Prediction of the Maximum Output Voltage Reachable with an Ultra-high Voltage Flyback Converter Driving Capacitive Actuators,"* in 2021 23rd IEEE European Conference on Power Electronics and Applications (EPE'21 ECCE Europe), 2021, pp. 1-9.

5 High voltage manipulation and energy recovery

5.1 Introduction

With the challenges due to the voltage amplification process now mastered, the purpose of this chapter is to delve more into the challenges of having to manipulate the high voltages necessary to actuate dielectric elastomer actuators as well as of having to remove and recover the energy ultimately stored in such a load.

The first section hereafter concerns a critical aspect necessary for the proper functioning of the system, namely the ability to measure the generated output voltages. Indeed, without it, very little is possible regarding the control or to check that the electronics operates correctly.

The second is about the method and resulting solution thanks to which the bidirectional behavior could be enabled. Indeed, due to nonexistent commercially available solutions, a custom-made HV switch had to be conceived.

And the third touches on the strategies tried and implemented to control this secondary switch in order to safely and efficiently reduce the output voltage as well as recover the charges stored in the capacitive load.

Finally, as done in Chapter 3, the energy efficiency of the discharge phase is estimated.

5.2 Integrated ultra-high impedance high voltage probe

One of the first issues that was quickly faced during the design process of the bidirectional converter was the necessity to be able to reliably measure the high voltages throughout the secondary side of the flyback, but most importantly across the load.

To satisfy the needs of the new electronics, the probe used must be capable to meet three major requirements. The first is, obviously, that it must be capable to withstand the targeted output voltage while including a safety margin.

The second is that it must be capable to measure precisely the dynamic variation of the voltage signals. As shown in the previous chapters, the voltages to measure can vary in as little as a few microseconds meaning that a bandwidth of at least several tens of megahertz is necessary.

And the third is that, because of the capacitive nature of the load, the probe must have an input resistance large enough so that the actuator does not lose all of its stored energy through the probe itself when actuated at max voltage. Indeed, knowing that the load is a capacitor of several nanofarads charged at 8 kV, one can determine the resistance necessary to ensure that the voltage across the load does not drop below a set percentage of the maximal value over the duration of the high voltage rest period using

$$V_f = V_i e^{-\frac{t}{R_{probe} C_L}} \iff R_{probe} = \frac{t}{C_L \left[\ln \left(\frac{V_i}{V_f} \right) \right]^{-1}} \quad (5.1)$$

where V_i and V_f are respectively the initial and final voltages across the capacitive load C_L and R_{probe} is the resistance of the probe. In our case, it was decided that at least 95 % of the voltage had to be left in the 2.4 nF load capacitor after 500 ms with an initial voltage of 8 kV. Therefore, the input resistance of the probe must be of at least 4 GΩ.

The combination of the two latter requirements makes the selection process for a commercially available device extremely challenging. Indeed, several high voltage probes and measuring systems do exist but none are capable to appropriately meet all three of the requirements. For example, electrostatic voltmeters such as the *Trek P0865* from *Advanced Energy* are capable to measure voltages well into the range necessary for our application with input resistances in the order of teraohms since they do not come into direct contact with the measured potential. However, they are designed to work with DC and up to 50 Hz signals and are therefore too slow for our targeted applications.

As for the best probe in regards to the bandwidth – which was the one ultimately obtained by the CAM – *Tektronix* offers the *P6015A* 20 kV oscilloscope probe with a bandwidth of 75 MHz. Unfortunately, it has an input resistance of only 100 MΩ. Using eq. (5.1), one can determine that the 2.4 nF load charged to 8 kV will empty itself by 95 % over 500 ms.

Therefore, a custom-made voltage probe had to be designed which would fit in between the two aforementioned types of probes.

5.2.1 Voltage divider design considerations

The designed probe makes use of the classical voltage divider layout using 5 surface mounted (SMD) resistors of 2 GΩ each put in series for a total of 10 GΩ with a 10 MΩ resistor to provide a 1000:1 dividing ratio as shown in Fig. 5.1. This total resistance value was selected because it allowed for fewer losses than the strict minimum calculated above while ensuring that the voltage across each resistor did not exceed their respective breakdown voltage and also due to the footprint sizes available to keep the probe as small as possible.

5.2 Integrated ultra-high impedance high voltage probe

To ensure proper operation of the probe, several design aspects had to be taken into account.

The first aspect being that, due to the way they are manufactured, resistors have an intrinsic parasitic capacitance which is conventionally modeled in parallel to the resistance. Since no two resistors are perfectly identical, this capacitance varies from component to component and if it is not taken into account in the design the behavior of the probe becomes hard to predict especially at high frequencies where their influence dominates. Thus, because the application for which the probe is destined to requires the probe to be able to accurately measure highly transient and fast signals, it was critical to balance the capacitive voltage divider with capacitors large enough to negate the parasitic capacitance of the resistors yet small enough to ensure that it steals as little energy as possible while the output voltage increases across the load.

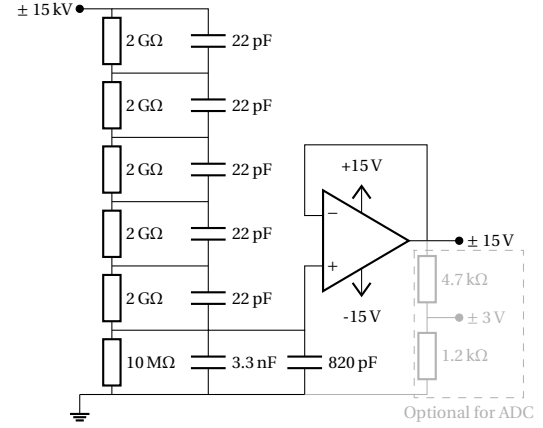


Figure 5.1: Schematic of the ultra-high impedance high voltage probe. An optional module can be added if necessary to use the probe with a microcontroller.

The balancing of the divider is achieved when the ratio of capacitances across the resistors is inversely proportional to the resistance ratio as shown by the equations below which are linked to the schematic of Fig. 5.2.

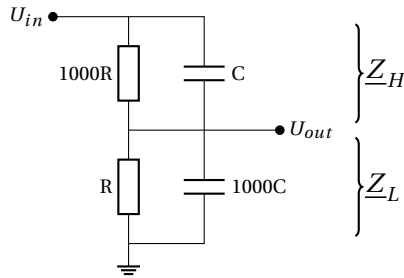


Figure 5.2: Simplified schematic of the high impedance voltage divider used to demonstrate the balancing of the capacitive divider.

$$\underline{Z}_H = \frac{1000R}{1 + j\omega 1000R \cdot C} \quad (5.2)$$

$$\underline{Z}_L = \frac{R}{1 + j\omega R \cdot 1000C} \quad (5.3)$$

$$\underline{Z}_{tot} = \underline{Z}_H + \underline{Z}_L = \frac{1001R}{1 + j\omega 1000RC} \quad (5.4)$$

$$\begin{aligned} \frac{U_{out}}{U_{in}} &= \frac{\underline{Z}_L}{\underline{Z}_{tot}} \\ &= \frac{R}{1 + j\omega 1000RC} \cdot \frac{1 + j\omega 1000RC}{1001R} \\ &= \frac{1}{1001} \end{aligned} \quad (5.5)$$

Figure 5.3 displays measurements of the output voltage generated by the flyback across a capacitive load. They were obtained simultaneously with voltage dividers of identical resistance but with two different sets of balancing capacitors, both theoretically meeting the aforementioned ratio requirement, and compared to *Tektronix's* P6015A probe which is used as reference. One can see that the divider with 5 pF capacitors across the 2 GΩ resistors performed worse than with 22 pF capacitors. It is believed that this is due to the smaller

capacitance value being too close to the value of the parasitic capacitance of the resistors for the latter to be negligible in comparison. Consequently, this influences negatively the capacitive ratio and thus the final ratio of the probe during the transient phase. Additionally, one can note in the left image a significant voltage drop during the resting phase. This drop is due to the reference probe discharging the capacitive load through itself because of its low input resistance as discussed previously.

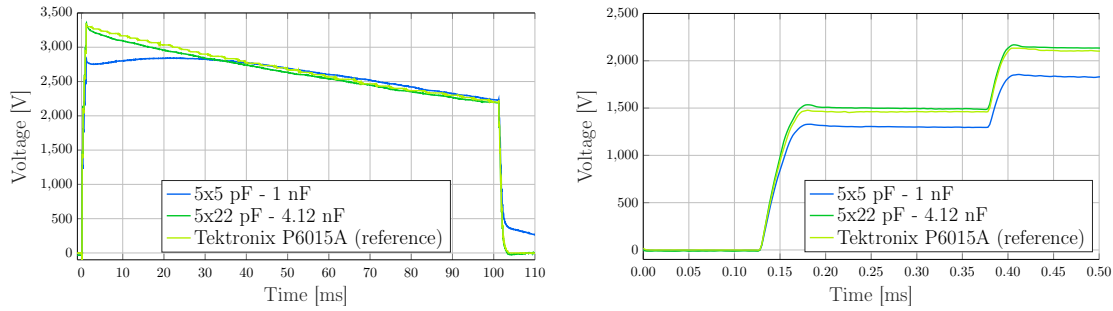


Figure 5.3: Comparison of measurements obtained simultaneously with two voltage dividers with adequate balancing capacitors (five 22 pF capacitors in series) and without (five 5 pF capacitors in series), and with *Tektronix's* P6015A probe used as reference for the tuning. The left image shows the evolution of the measured voltage across a long duration and the right image presents a zoom of the first two pulses. The significant voltage drop visible on the left is due to the reference probe emptying the load during the measurement process.

The second aspect concerns the monitoring of the voltage output across the low side of the probe. Indeed, because of the already large resistance value of 10 M Ω used, directly measuring the divided voltage with any kind of conventional probe – e.g. a typical oscilloscope probe with a input resistance of 1 M Ω – will greatly influence the dividing ratio and limit the performances of the voltage divider. Therefore, an additional operation amplifier (OpAmp) in voltage follower mode was integrated to make use of the extremely high – in the order of 10¹² Ω – input resistance of the device. This allows for any type of probe to be used or for further division of the voltage to be sent e.g. to a microcontroller for control purposes. Ultimately, the voltage range the probe is capable to measure is limited by the voltage supplied to the OpAmp which is, in our case, ± 15 V multiplied by the division ratio of 1000. Therefore, the new probe is theoretically capable to provide measurement of voltages of up to ± 15 kV.

And finally, due to the voltage levels manipulated and their speed, the last aspect is the footprint layout of the probe which is also critical to avoid any unwanted additional parasitic capacitance and inductance in the circuit as was discovered at our expense and shown in Figs. 5.4 and 5.5. Indeed, these figures present measurements of the output voltage with two probe prototypes with different PCB layouts. The faulty prototype was a tentative for a more compact design by having the components forming a U-shape. It is supposed that due to the difference in voltage between the various resistors the influence of the inter-components parasitic capacitances is increased which unbalanced the voltage divider. In addition to that, a parasitic inductance due to the layout's shape may also have made matters worse.

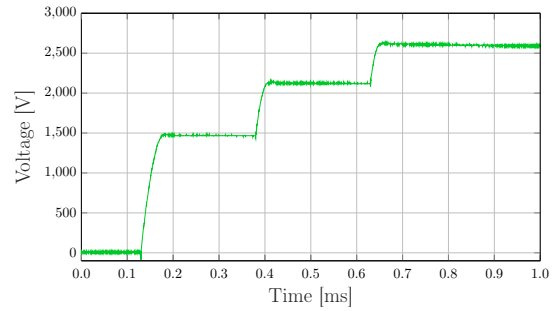
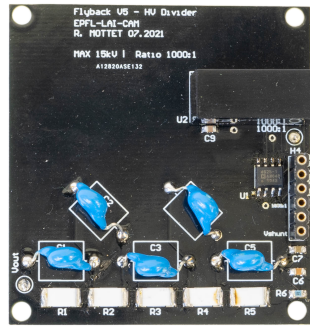


Figure 5.4: Left, linear probe prototype with, right, the corresponding measurement of the output voltage across a capacitive load. The signal is stable despite the large voltage jump experienced.

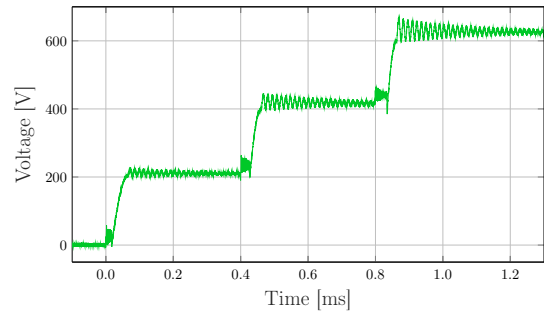
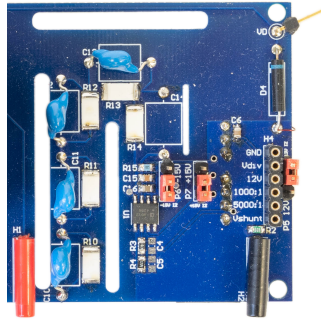


Figure 5.5: Left, U-shaped probe prototype with, right, the corresponding measurement of the output voltage across a capacitive load. Significant unwanted oscillations are visible during the resting state between pulses.

Ultimately, a comparison between the newly designed probe and *Tektronix's* P6015A oscilloscope probe was realized to make sure that the former achieves the performances required by the converter. Figure 5.6 shows the result of this comparison and one can see that, at least within the scope of this application, it clearly out-performs the latter as it follows very well the transient signals during the charge phase while having minimal influence on the voltage across the capacitive load during the rest phase.

5.3 Pulsed transformer gate drive switch

With the ability to supply as well as measure the required voltages achieved, the next major challenge was to enable the bidirectional flow of energy through the flyback to recover as much energy from the load as possible and send it back to the 12 V power supply while bringing the output voltage back down to 0V.

To do so, as previously discussed, a secondary switch M_s placed in parallel to the secondary diode as shown in Fig. 5.7 and capable to withstand at least 8kV and fast enough to avoid the saturation of the core was necessary.

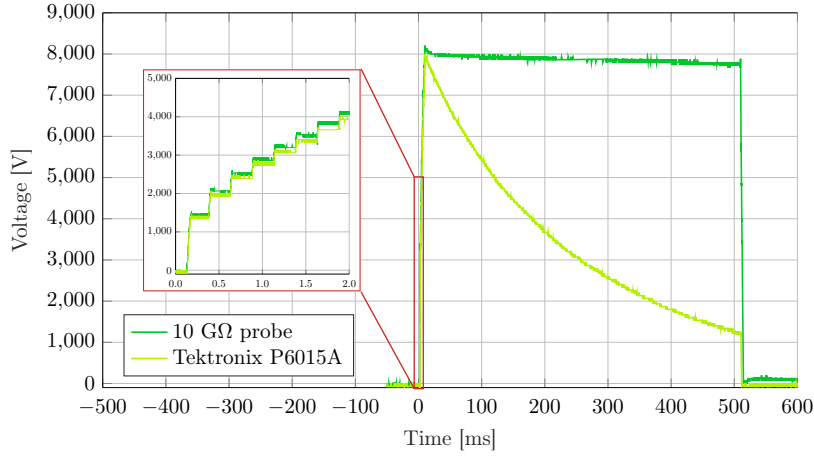


Figure 5.6: Comparison of the custom-made ± 15 kV, 10 G Ω voltage probe with *Tektronix's* P6015A 20 kV, 100 M Ω oscilloscope probe while measuring the output voltage across the capacitive load over the course of 500 ms.

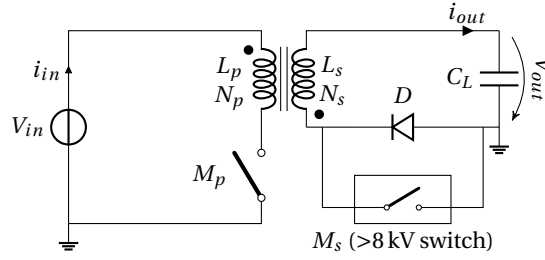


Figure 5.7: Basic model of the bidirectional flyback with the location of the HV switch displayed.

However currently, as mentioned in Chapter 2, commercially available switches that meet the necessary requirements for our application – high voltage breakdown, low current, high speed, and compactness – are scarce to non-existent. The best switches available are in *IXYS'* IXTx02N450 series [24] and are rated to hold up to 4.5 kV.

Nevertheless, *Wolfsped Inc.* (previously *Cree*) is reportedly working on the development of a new generation of SiC MOSFETs that are supposedly capable to withstand 10 to 15 kV [54] [55]. However, this technology is still in early development and the first MOSFET prototypes obtainable have a significantly high leakage current of about 1 mA in open state which is highly detrimental for our application.

This problematic led to the work of Pniak [56] in which he lays the groundwork for the implementation of the Pulsed Transformer Gate Drive (PTGD) topology which allows for several of those 4.5 kV MOSFETs to be put in series to effectively create much larger switches. In this work he managed to create two PTGD switches with each having 4 of those MOSFETs put in series and used them as part of a half bridge converter driving a voltage of 16 kV.

5.3.1 Working principle

The working principle of a PTGD switch is as follows. As shown in Fig. 5.8, the system consists of four main parts: the low voltage main driving circuit (MDC), a single or multiple (one for each HV MOSFETs) transformers, a secondary driving circuit (SDC) for each of the HV MOSFETs, and the HV MOSFETs themselves.

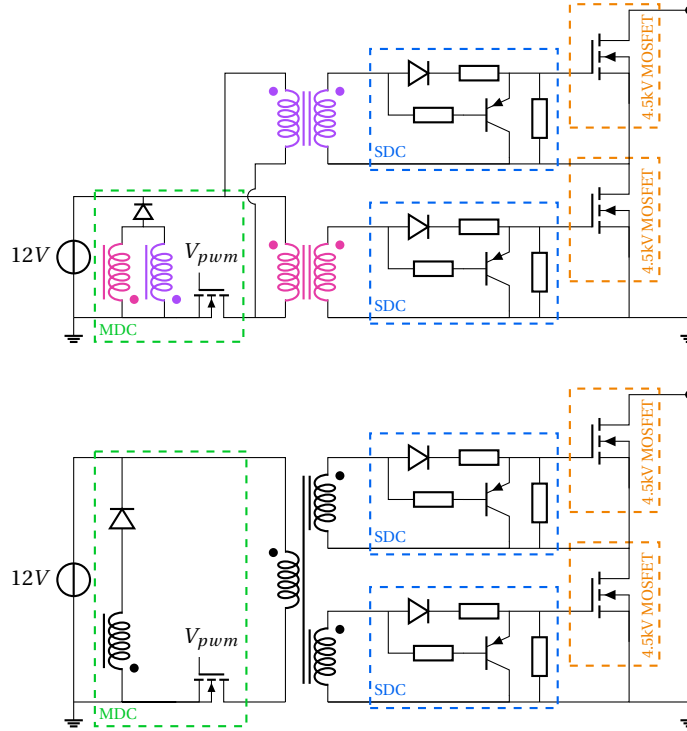


Figure 5.8: Basic schematics of a two MOSFETs pulsed transformer gate drive switch with, at the top, a transformer for each HV MOSFETs and, on the bottom, a single transformer with multiple windings.

The main driving circuit operates at low voltage – in our case 12 V – and consists of a primary MOSFET which is closed to instruct the HV MOSFETs to close as well by applying 12 V across the primary winding of the transformer(s). Consequently, a current linearly increases (similarly to the flyback itself) in the MDC through the primary winding(s) and the low input voltage is mirrored by the transformer on the secondary sides. Upon noticing the change in voltage, each of the SDCs allow their respective HV MOSFETs to close nearly perfectly in sync.

When the primary MOSFET reopens, the flow of current in the MDC stops and the process is essentially reversed with the auxiliary winding(s) demagnetizing the transformer(s) to increase the speed at which the HV MOSFETs reopen.

An important note is that it is critical to select the transformer core(s) with care by making sure that saturation is not reached while the PTGD switch is closed to avoid any risks of damage to the electronics. Indeed, smaller transformers can be used but reach saturation faster and thus the PTGD switch cannot remain closed for long periods of time.

5.3.2 The 13.5 kV switch

Taking inspiration from the work of Pniak, a 3 MOSFETs PTGD switch, of which a photography and its schematic are shown in Fig. 5.9, was fabricated for the bidirectional flyback. The reasoning behind the decision to create a 13.5 kV switch rather than a simpler two MOSFETs 9 kV one is because the potential V_D experiences voltage variations much larger – in the order of several kilovolts – than the output voltage across the load due to resonances in the circuit between the various inductances and parasitic capacitances. One can find its characteristics and components in Table 5.1

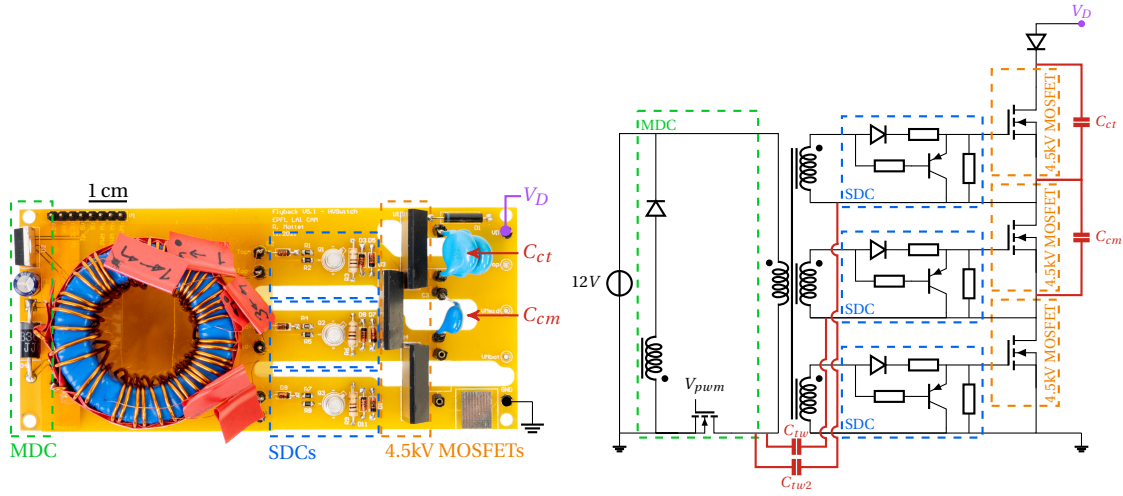


Figure 5.9: Photography and corresponding schematic of the 3 MOSFETs PTGD switch manufactured for the 8 kV bidirectional flyback. Highlighted are the locations of the various modules that compose the switch. C_{tw} and C_{tw2} are the parasitic inter-winding capacitances of the transformer and C_{ct} and C_{cm} are the compensation capacitors added to help balance the voltage across the top and middle MOSFETs respectively.

Parameter	Value
High voltage diode D_{HV}	12 kV, 20 mA [HVEF12P]
High voltage MOSFETs	4.5 kV, 200 mA [IXTF02N450]
PNP transistors	-60 V, -600 mA [2N2907A]
Driving MOSFET M_D	40 V, 3.6 A [IRLML0040TRPbF]
Compensation capacitor C_{cm}	33 pF
Compensation capacitor C_{ct}	150 pF (82+68 pF)

Transformer (5 identical windings)	
Material	Vitroperm 250 F
Geometry	Toroid (40x32x15 mm)
Nb of turns (all windings)	23
Inductance (all windings)	1.0 mH
Inter-winding capacitance C_{tw}	27.3 pF
Inter-winding capacitance C_{tw2}	~54 pF

Table 5.1: Characteristics and components of the PTGD switch

5.3.3 PTGD switch upgrades

However, two notable and critical differences were implemented in the switch of the flyback compared to the ones in the work of Pniak. Namely, where he used multiple transformers to drive the MOSFETs – one for each – the switch for the flyback was designed with only a single transformer with multiple windings to help reduce the overall size of the device. This modification revealed an unfortunately overlooked detail by Pniak concerning the selection of the voltage balancing capacitors put in parallel to each MOSFETs similarly to the previously discussed high impedance probe. Indeed, in his work he explains correctly that the inter-winding parasitic capacitances of his transformers have a detrimental influence on the voltage balancing between the HV MOSFETs and that one should place compensation capacitors of identical value to the inter-winding capacitance in parallel to the middle MOSFET and of three times this value across the top-most one to fix the issue.

However, the measurements of Fig. 5.10 realized on the flyback PTGD switch show that, if this recommendation were to be followed to the letter, the voltage across the MOSFETs would not be adequately distributed. Indeed, it was observed after several successive trials that the capacitance of the compensation capacitor across the top-most MOSFET must be approximately equal to three times the sum of **both** the inter-winding capacitance of the primary winding and the (in our case) identical inter-winding capacitance of the auxiliary demagnetizing winding. It is believed that this difference may be due to the fact that the auxiliary winding in Pniak's work is smaller and has fewer turns, and thus may have had a negligible parasitic capacitance. Therefore, for our device, the capacitance of C_{ct} had to be increased from approximately 75 pF to 150 pF to obtain a suitable voltage balance.

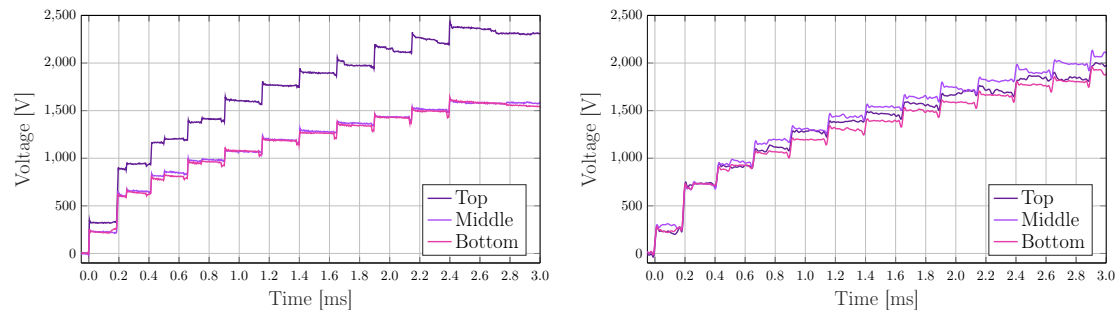


Figure 5.10: Comparison of the distribution of the voltage measured across the top, middle and bottom MOSFETs of the PTGD switch without (left) and with (right) proper balancing. One can clearly see on the left graph how the voltage across the top-most MOSFET is significantly larger than across the other two.

Finally, a diode was also added in series to the switch to negate the influence of the HV MOSFETs' body diodes during the charge phase to make sure that all of the current only passes through the main secondary diode thus limiting unnecessary losses and improve performances. An additional benefit of this diode is the help it provides to stop faster the current from flowing through the switch when it reopens.

5.4 Discharge control strategies

As previously mentioned in Chapter 3, the working principle of the discharge phase of a bidirectional flyback is essentially the same as that of the charge phase of a unidirectional flyback. The capacitive load is discharged by gradually removing chunks of stored energy and sending them back to the input power supply through the coupled inductor. To do so, the secondary PTGD switch M_s is periodically opened and closed to let a negative current I_{out} flow as shown Fig. 5.11.

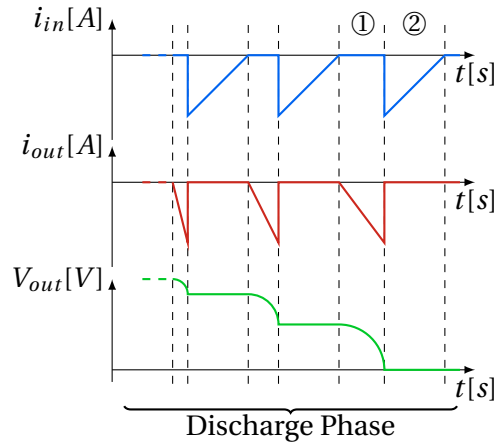


Figure 5.11: Ideal current and voltage waveforms during the discharge phase. By alternating steps ① (M_s closed) and ② (M_s open), the voltage across the load diminishes and the energy it stores is sent back to the input power supply.

In order to safely operate the PTGD switch and discharge the load back through the flyback without reaching the saturation of the coupled inductor's core, two control strategies were investigated. The first one makes use of a high-performance analog-to-digital converter (ADC) to monitor the current flowing through the coupled inductor, whereas the second one is a more passive solution in which a comparator circuit is set to trigger the reopening of the switch as soon as the monitored current exceeds a given threshold. At the end of this section, a comparison between the two solutions is provided where their respective pros and cons are discussed.

The challenge comes from the fact that the time t_{on} it takes for the current to reach saturation varies greatly as it is proportional to the voltage across the load and can thus become extremely short. This duration can be estimated using

$$t_{on} = \frac{L_s + L_{ls}}{V_{out}} \hat{i}_{out} \quad (5.6)$$

where \hat{i}_{out} is the peak value of the current i_{out} tolerated before the saturation of the core.

To give a concrete example of how fast the secondary switch must be controlled at high voltages, let us consider the custom made coupled inductor characterized in Chapter 3. With

the inductance value, the geometry and the material used, one can calculate that the peak current \hat{i}_{out} for which the core starts to saturate is of around 160 mA. To avoid the risk of crossing that threshold, let us consider a current value of 100 mA. This large safety margin was put in place because it was noticed that there was a small delay between the opening instruction and the effective reopening of the PTGD switch as shown further below, but large enough that the current could reach saturation if not kept in check. By using this safe threshold value in (5.6) as well as the values of the secondary inductances L_s and L_{ls} , and an output voltage of 7 kV, t_{on} is equal to $6.5\mu s$ which is approximately what is shown in Fig. 5.12.

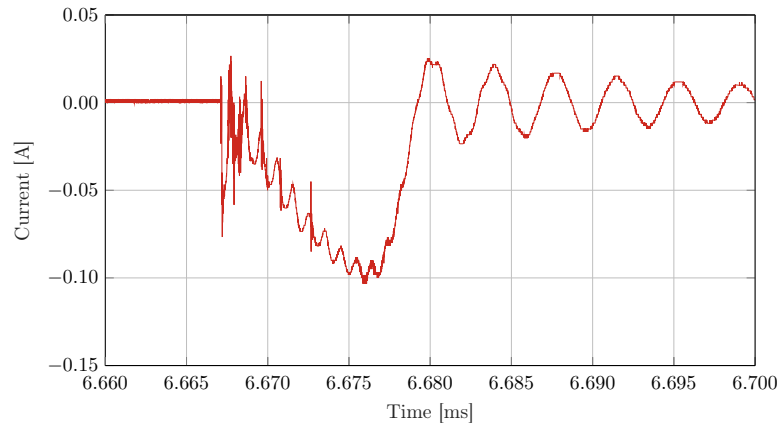


Figure 5.12: Output current measured during the discharge phase with an output voltage of 7 kV across the capacitive load. The current reaches 0.1 A in approximately $7\mu s$.

Conversely, during the latter pulses when the output voltage is nearing 0 V, t_{on} increases significantly as shown further below. It is therefore necessary to implement a control strategy which allows for a dynamic update of the conduction time t_{on} .

5.4.1 ADC-based control strategy

To do so, as mentioned earlier, the first strategy that was investigated is based around the high-performance ADC module of *Texas Instruments'* TMS320F28379D microcontroller to measure the output current. This module is capable to operate at up to 3.5 MSPS with a 12 bits resolution and single ended inputs. The high frequency capability is necessary to make enough measurements during the t_{on} time span to quickly and reliably make sure that i_{out} does not exceed the set security threshold of 100 mA.

Hardware implementation

To measure the current i_{out} which flows through the capacitive load, a 10Ω shunt resistor was used. However, during the discharge phase, i_{out} generates a negative voltage across the shunt resistor which means that the resulting voltage cannot be directly fed into the ADC as only single ended and positive inputs can be read. To overcome this, a voltage follower inverting

operational amplifier was added to the system as shown in Fig. 5.13. To influence as little as possible the measurement, the resistors used with the inverting OpAmp were selected to be 100 times larger than the shunt resistor.

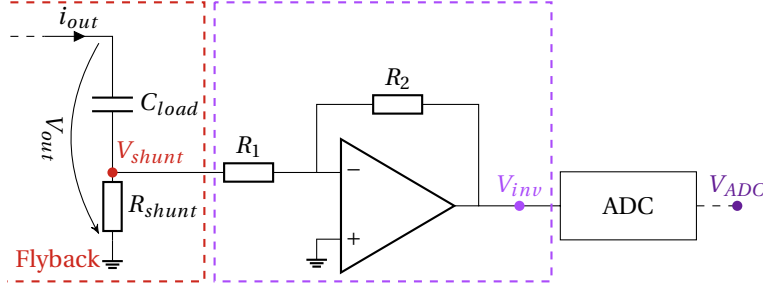


Figure 5.13: Circuit inverting the measured signal i_{out} to make it readable by the ADC of the microcontroller. Here, $C_{load} = 2.4\text{ nF}$, $R_{shunt} = 10\Omega$. R_1 and R_2 are identical and are $1\text{ k}\Omega$ resistors. V_{shunt} , V_{inv} and V_{ADC} are measuring points to obtain the image of the current in volts at various points in the circuit.

Software implementation

While the electronics circuit appears to be quite simple, the software is, however, more convoluted. Indeed, interactions between the PWM and ADC modules must be carefully managed through the use of interrupts to make sure that the switch is reopened in a timely manner.

The algorithm that was put in place works as follows and Fig. 5.14 gives a visual representation of the various timings of the interrupts :

1. When the command to discharge the load is sent, the PWM timer linked to the PTGD switch is enabled.
2. When the PWM counter passes a set compare value, the polarity of the control pin is set to high to close the switch and an interrupt is triggered.
3. This interrupt enables the ADC timer which is set to a sampling frequency of 2.8 MSPS to read the voltage coming out of the inverting operational amplifier. Each reading triggers an interrupt during which the measured value is compared to a manually fixed threshold value. The first 5 measurements are however ignored because of the large initial voltage spike visible in Fig. 5.12 which is due to the closing of the switch as it would cause a false positive to trigger the reopening of the switch.
4. Once the threshold value is reached or exceeded, the ADC timer is disabled and reset. The counter of the PWM is also set back to 0 which forces the polarity of the control pin to be set back to low, effectively telling the switch to reopen.
5. In the case where the output voltage has nearly reached 0 V and the current cannot rise above the threshold value due to the low amount of energy left in the load, the switch is automatically reopened after a set amount of time. This security is absolutely necessary to avoid the saturation of the PTGD transformer as explained earlier.

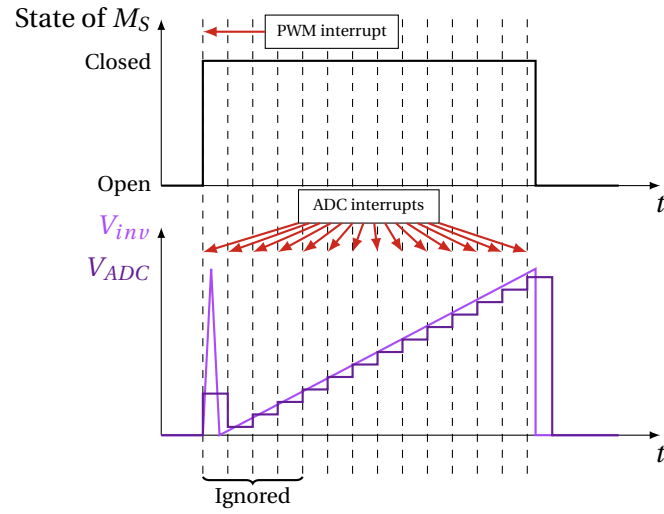


Figure 5.14: Visual representation of the various occurrences of the interrupts for the operation of the secondary switch during the discharge phase.

Experimental Results

By implementing the control strategy presented above, the PTGD switch of the bidirectional flyback can be reliably operated in such a way that the amount of energy removed from the capacitive load is controlled and, in this case, constant. This leads to a smooth and nearly symmetrical charge and discharge cycle to a high output voltage of 7kV as shown in Fig. 5.15.

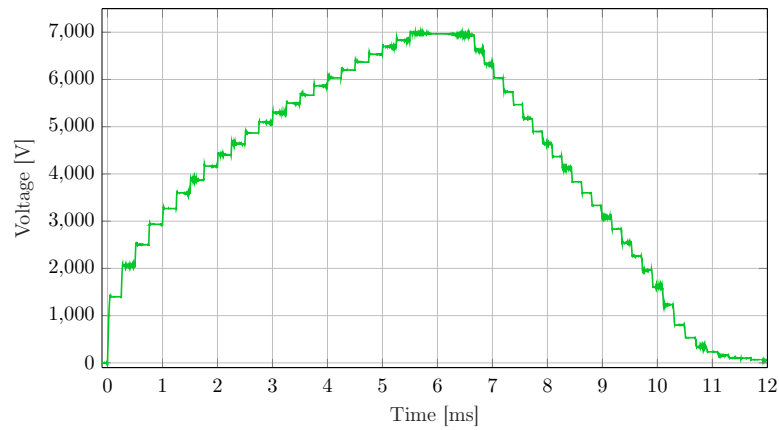


Figure 5.15: Output voltage across the capacitive load. Thanks to the constant pulses of energy during the charge and discharge phases, the voltage rises and falls nearly symmetrically.

As for the output current, Figs. 5.16 and 5.17 show an image of the actual negative current measured at the points indicated in Fig. 5.13, that is through the 10Ω shunt resistor, the current waveform after the inverting circuit and finally the current measured by the ADC module during the first pulse of the discharge phase when the output voltage is at 7kV and then when the output voltage is much lower at around 1.2kV.

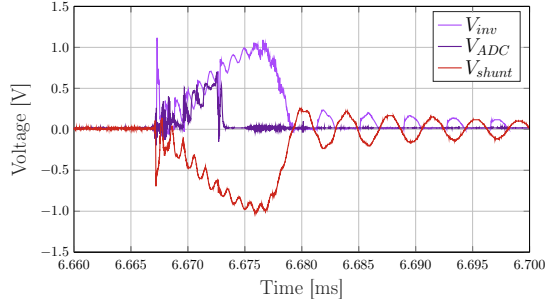


Figure 5.16: Measured voltage images of the output current taken when the output voltage is at 7kV. Once directly across the 10Ω shunt, once after the inverting circuit and finally the actual measured values obtained with the ADC (and output through a Digital-to-Analog Converter).

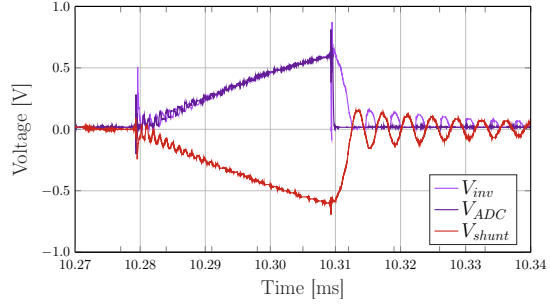


Figure 5.17: Measured voltage images of the output current made when the output voltage is at 1.2kV. This figure displays an occurrence of the automatic reopening of the switch after a set amount of time (here $30\mu\text{s}$) to protect it from the saturation of the transformer.

The aforementioned figures show that the control strategy works well and can reliably operate the bidirectional flyback at ultra-high voltage levels. However, Fig. 5.16 reveals several noticeable aspects that may need to be considered for future iterations.

First, at high voltage, the implemented strategy is close to the limit of what it is capable of as the sampling frequency is near the maximum available; the duration during which it must take measurements is extremely short; and the current during the first few microseconds is very noisy. Consequently, if the voltage increases further and the time span shortens, the measured current may end up being heavily dominated by noise which could in turn be falsely interpreted by the control system to reopen the switch.

Second, as mentioned above, there is a delay of a few microseconds particularly well visible in Fig. 5.16 between the moment the switch is ordered to reopen and the moment it actually starts opening. This confirms the necessity for the large safety margin defined earlier.

And finally, it was observed that the PTGD switch appears to be slow at reopening as shown by the slow fall of the current from its peak back down to 0A. While the exact reason behind this behavior was not yet investigated, it is believed that one of the first location for improvements should be the secondary driving circuit with a modification of the PNP bipolar transistor as well as a reduction of the resistor connected to its base. Ultimately, implementing these upgrades could potentially greatly reduce the commutation losses of the switch.

In Fig. 5.17, one can see the security procedure in effect where after a set amount of time (here $30\mu\text{s}$) the switch reopens regardless if the current reached the maximal tolerated peak value.

5.4.2 Schmitt trigger-based control strategy

A second strategy was investigated to look for possible ways to improve upon some of the aforementioned shortcomings of the ADC-based strategy. To do without the ADC module, a plan was devised to implement a circuit which would passively monitor the state of the current and trigger a signal which can be interpreted by the microcontroller as soon as it exceeds a set threshold to, once again, protect the electronics from the risk of saturation of the coupled inductor core.

Since the maximum peak current tolerated is constant throughout the discharge phase of the flyback, when the goal is to discharge the load as fast as possible one can turn oneself towards comparator circuits, and more specifically the Schmitt trigger variant to conduct this operation.

Hardware implementation

Indeed, the Schmitt trigger is a member of the comparator circuits family which can be designed in such way that it can operate with an asymmetrical power supply (e.g. GND and $V_{DD} = 3.3\text{ V}$) so that its output can be directly fed to a microcontroller. Additionally, this topology possesses an adjustable hysteresis meaning that its output can be toggled between its two possible states by two different input voltages as shown in Fig. 5.18. This characteristic is very valuable to allow the system to be more resilient against noise which is advantageous for our application as mentioned above. Indeed, noise could trigger a basic comparator repeatedly in an unwanted manner. Whereas with the Schmitt trigger, if both threshold voltages are sufficiently far apart its output can be more stable and reliable.

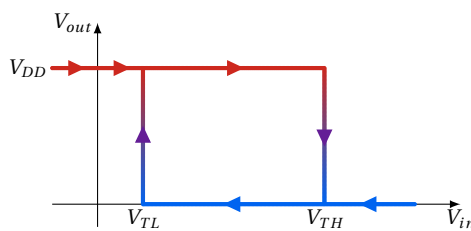


Figure 5.18: Hysteresis of an inverting asymmetric Schmitt trigger circuit.

For the bidirectional flyback, an inverting asymmetric Schmitt trigger was implemented and its circuit is shown in Fig. 5.19. However, to properly operate, an additional circuit is necessary and consists of an OpAmp voltage adder module. This necessity stems from the varying polarity of the output current i_{out} throughout the entire operation of the flyback. Indeed, during the charge phase the output current is defined as positive whereas, during the discharge phase, the current is reversed. Since the Schmitt trigger is destined to be used during the discharge phase but cannot be triggered by negative voltages if its output is to be read by an I/O port of a microcontroller, adding an offset voltage solves this issue and allows the Schmitt trigger to react to negative currents as well.

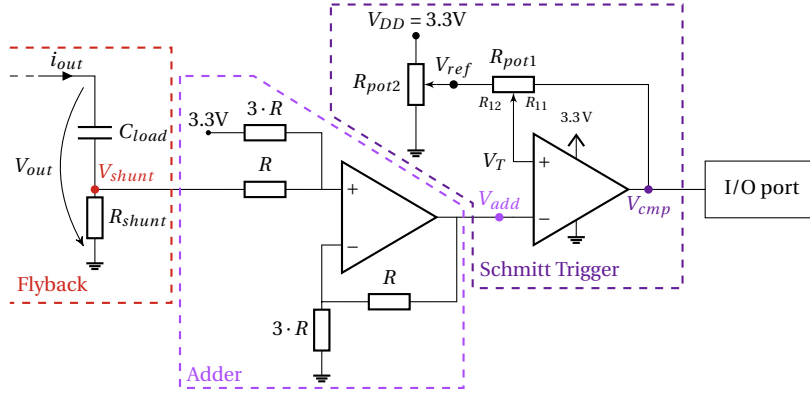


Figure 5.19: Basic schematic of the Schmitt Trigger-based electronics. Since the current i_{out} can be positive and negative during the operation of the flyback, it is necessary to add an offset voltage in order to stay in measuring range of the I/O port. V_{shunt} provides the voltage image of i_{out} , V_{add} is V_{shunt} with an offset, and V_{cmp} gives the state of the trigger.

Moreover, to tune the threshold voltages, two potentiometers are used. R_{pot2} tunes the reference voltage V_{ref} which allows to laterally shift the whole hysteresis whereas R_{pot1} tunes the threshold voltages themselves according to the following formulas:

$$V_{TL} = V_{ref} \left(1 - \frac{R_{12}}{R_{pot1}}\right) \quad (5.7)$$

$$V_{TH} = (V_{DD} - V_{ref}) \frac{R_{12}}{R_{pot1}} + V_{ref} \quad (5.8)$$

Where R_{12} represents a fraction of the total value of R_{pot1} , and V_{DD} is the power supply voltage of the Schmitt trigger and is, in our case, equal to 3.3 V.

Ultimately, Fig. 5.20 shows an ideal representation of the evolution of the three highlighted potentials of Fig. 5.19. For our application, the offset was set to approximately 1 V which corresponds to the maximum amplitude of the current i_{out} flowing through the 10 Ω shunt resistor. This offset is set by carefully selecting the resistance value R of the resistors in the adder module and it is, in our case, worth 1 k Ω so that the current drawn by the module is minimal.

Software implementation

Regarding the software, the control algorithm is much simpler than with the ADC alternative and works as follows:

1. The PWM timer is enabled as soon as the system is asked to start the discharge phase. Consequently, the switch M_s is closed.
2. After a short delay implemented to ignore initial voltages spikes due to the closing of the switch, an external interrupt is enabled. This interrupt is linked to the I/O port where the Schmitt trigger is connected to.

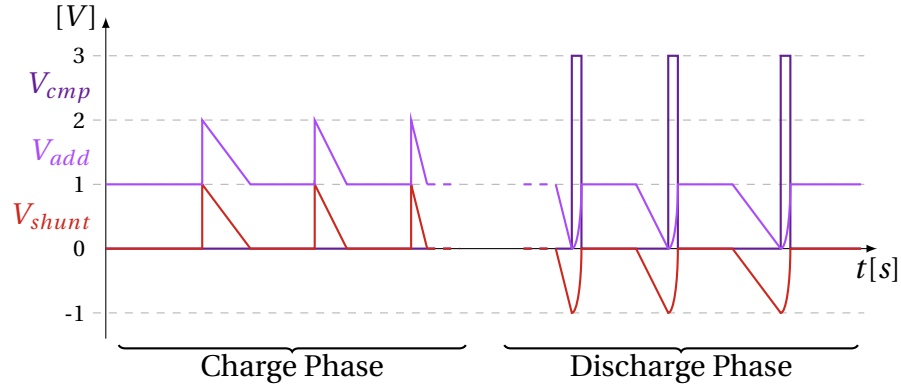


Figure 5.20: Ideal waveforms of the main voltages through the Schmitt trigger-based circuit. The threshold voltages of the comparator circuit are set in such a way that a triggering event can only happen during the discharge phase when the voltage measured across the shunt resistor falls below a given value.

3. As soon as the I/O port notices a change in polarity from Schmitt trigger, the external interrupt is triggered. This interrupt resets the PWM timer which forces the switch to reopen.
4. As a fail-safe security, the switch will automatically reopen after a set time interval regardless of the state of the Schmitt trigger. This is necessary to protect the PTGD switch against the saturation of its transformer as explained earlier.

Experimental Results

The implementation of the presented comparator topology as shown in Fig. 5.21 and corresponding control strategy permitted a reliable operation of the PTGD switch of the bidirectional flyback during its discharge phase. An output voltage of now at least 8 kV can be manipulated as shown in Fig. 5.22.

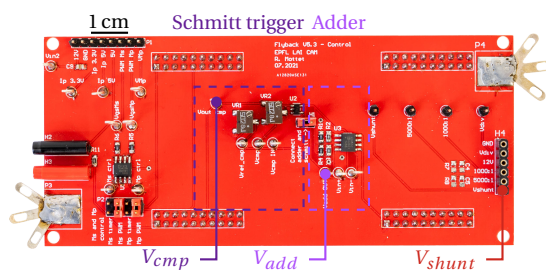


Figure 5.21: Photography of the circuit board on which is located the Schmitt trigger module used to drive the PTGD switch during the discharge phase of the bidirectional flyback.

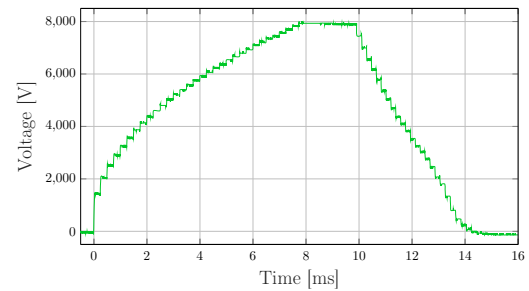


Figure 5.22: Output voltage measured during one cycle of operation of the flyback converter. The Schmitt trigger module was used to discharge the load.

Figure 5.23 presents actual measurements of the voltages analogous to their schematic representation shown in Fig. 5.20 made when the output voltage is once at 8 kV and then when it drops below 1 kV respectively.

On the left image, one can see that the output of the Schmitt trigger V_{cmp} changes when the image of the output current V_{add} falls below 0.2 V and is toggled back when it rises above 0.6 V.

The right one shows three pulses of current which happen during the transition time where the first pulse (on the left) still rises fast enough to trigger the comparator circuit whereas for the two following ones the maximum conduction time of 30 μ s is elapsed before and thus forces the switch to reopen. This shows that the algorithm put in place works well regardless of the output voltage currently on the load.

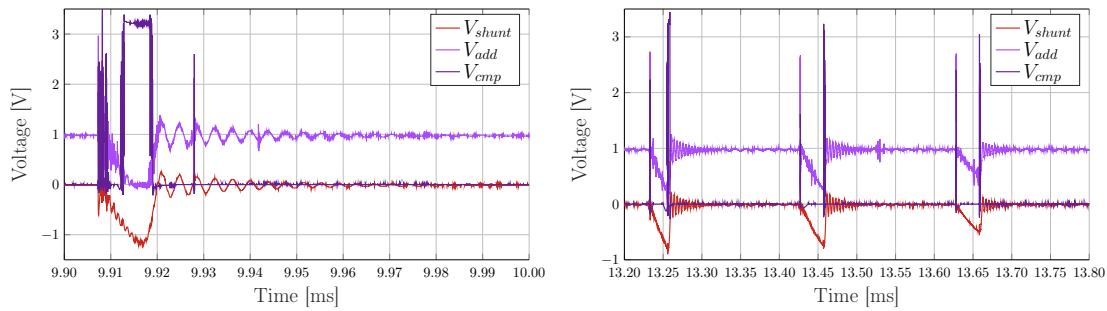


Figure 5.23: Actual measurements of the potentials mentioned in Fig. 5.20. The graph on the left displays the waveforms when the output voltage is at its maximum of 8 kV whereas the graph on the right shows the same waveforms but when the voltage has dropped below 1 kV.

Additionally, one can notice that, despite the noisy red and consequently blue waveforms, there is a clear toggling of the Schmitt trigger after only 4 μ s of current flowing. This figure also shows that this control strategy has the potential to be pushed a bit further to react to even faster and shorter conduction times. The slow reopening of the PTGD switch can here also be observed. This characteristic is essential to keep in mind when choosing the threshold voltage so that the residual current flowing despite the closing instruction does not push the coupled inductor to saturation.

5.4.3 Pros and cons

Naturally, both of these solutions have their own respective advantages and disadvantages.

Concerning the ADC-based solution, some of its main advantages are the size of the additional external circuit which is arguably smaller as it requires fewer components, and the possibility to easily control and change the threshold voltage which triggers the reopening of the switch since it is embedded in the code itself.

However, this solution requires a very high-performance ADC module and an adequate microcontroller which come at a larger monetary cost as well as high electrical and processing power consumptions.

Conversely, the Schmitt trigger-based solution is simpler in its working principle with a passive monitoring of the system which is done with a very basic set of cheap and low power consuming components. Additionally, this system is less sensitive to noise thanks to the asymmetrical threshold voltages and it can react faster to the crossing of the thresholds.

Nonetheless, the comparator system does, in its current form, occupy a larger footprint than its ADC-based counterpart. In addition to that, on-the-fly modifications of the threshold voltages are not possible because of the fact that they are physically set with an array of resistors.

Ultimately, it was decided that the latter solution would be kept mainly due to the processing power requirements in prevision of future modifications such as the substitution of TI's development board for an integrated, cheaper, and lower power consuming microcontroller.

5.5 Experimental results

With the aforementioned hardware and software upgrades added to the circuit as shown in Fig. 5.24, the latest iteration of the bidirectional flyback converter could be put in action. Similarly to what was done in Chapter 3, the measurements displayed hereafter were the ones used for the estimation of the energy efficiency performed in Section 5.5.3 below.

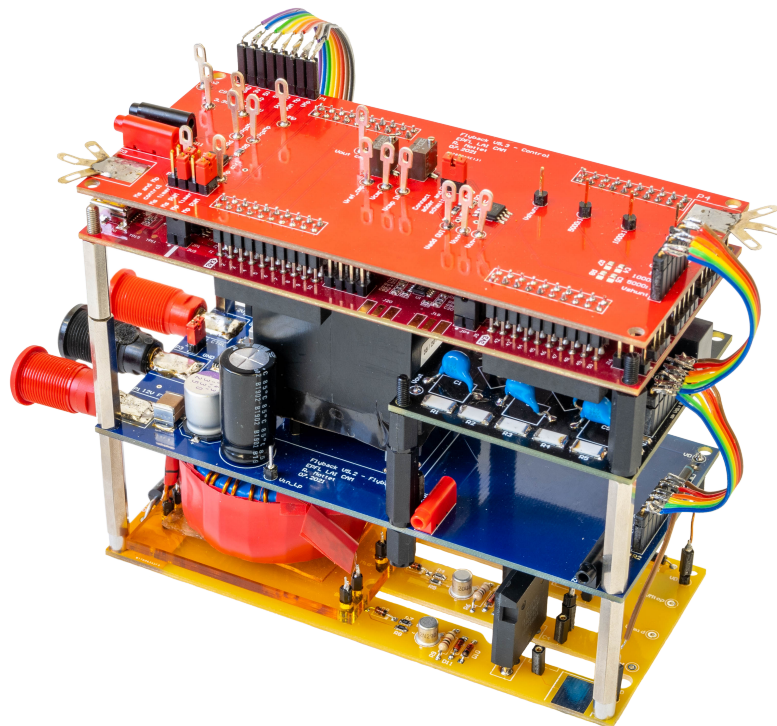


Figure 5.24: Photography of the latest ultra-high voltage bidirectional flyback converter prototype. An exploded view of the converter can be found in Annex C.

5.5.1 General measurements

With the complete system, it is now possible to not only charge a capacitive load to at least 8 kV, but also discharge it back down to 0 V as shown in Fig. 5.25 in which the output and input voltages are displayed. One can note that the input voltage actually increases during the discharge phase. This is due to the reverse flow of energy being recovered from the load. All measurements presented hereafter were obtained the same way as in Section 3.5.1 according to Fig. 3.18.

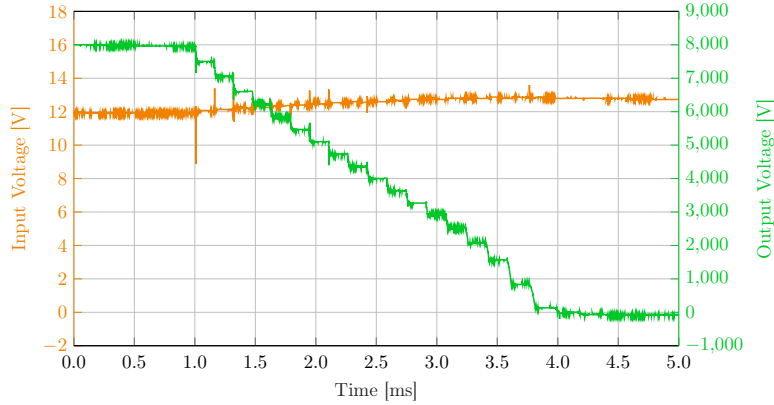


Figure 5.25: Measured output and input voltages during the discharging of a 2.4 nF capacitor from 8 kV down to 0 V in barely over 3 ms. The input voltage increases during this time because of the influx of energy from the load.

Figure 5.26 presents two graphs of the input and output currents flowing through the flyback over three successive pulses at both the beginning and end of the charge phase. In the first one, the output voltage is at its maximum of 8 kV and in the second one it nearly reached 0 V.

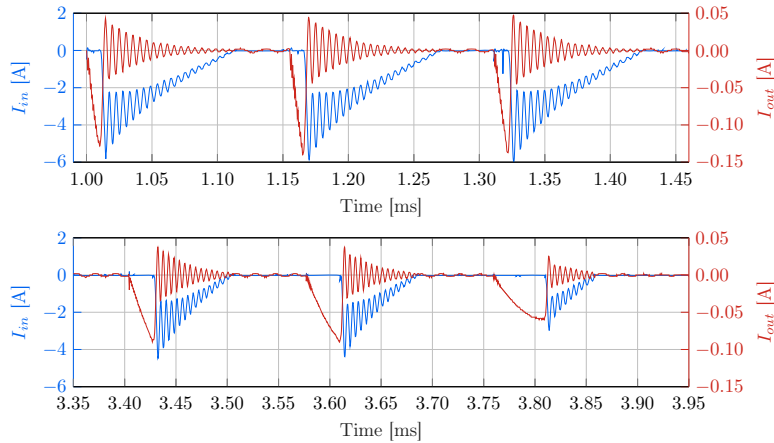


Figure 5.26: Measured output and input currents over the course of three successive pulses of energy at the beginning (top) and end (bottom) of the discharge phase.

Finally, Fig. 5.27 presents the evolution of the voltages V_{M_p} and V_D during the same three pulses of energy mentioned above. In the second graph from the top, one can see that the

voltage across the secondary switch experiences large oscillations reaching at least 10 kV. These are the reasons why it is necessary to have a least a 3-MOSFETs PTGD switch when the output voltage required is 8 kV or more.

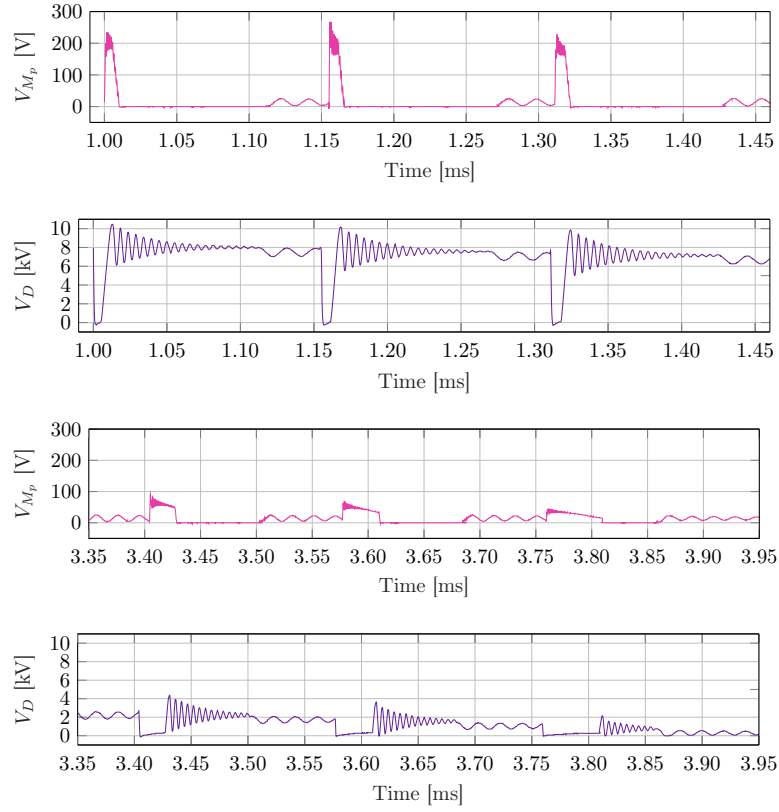


Figure 5.27: The first and second graphs show the waveforms of the voltage across the primary MOSFET and the PTGD switch respectively and measured during the first 3 pulses of the discharge phase. The third and fourth graphs are the same voltages but they show 3 of the last pulses as the output voltage drops below 1 kV.

5.5.2 Energy calculation procedure

The procedure followed to obtain the estimation of the energy efficiency is nearly identical to what was performed in Section 3.5.2. Namely, for a given pulse of energy, a period is divided in distinct steps which are directly related to the states in which the semiconductor components can be found. With a difference being that Steps ④ and ⑤ are irrelevant in the case of the discharge phase as shown in Fig. 5.28 and as discussed further below.

Regardless, the energy dissipated or stored in each component is obtained, when possible, by integrating the product of the current flowing through and the voltage across them. Otherwise, it is determined by calculating the difference of energy levels between the start and the end of each step using the relevant classical energy equation for each component. One must note that, because of the complexity of the PTGD switch and the subsequent difficulty of

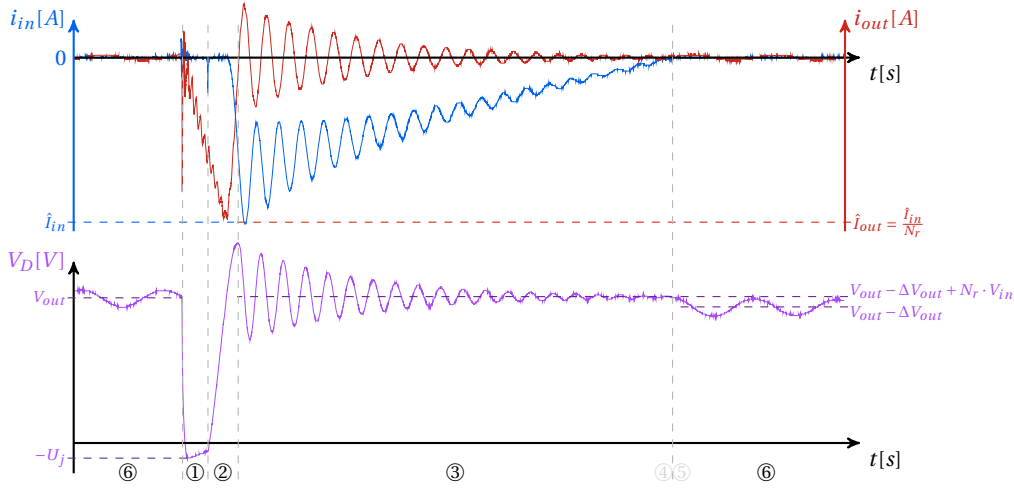


Figure 5.28: Measure of the evolution of the potential V_D in relation to the state of the semiconductor components which shows when the various steps of any given discharge pulse happen.

differentiating precisely the influence of its various parasitic elements during each step, the total amount of energy \mathcal{E}_{PTGD} dissipated because of its ON-resistance and the commutation losses, as well as what ends up stored in its parasitic capacitance was determined with the first method mentioned for a complete pulse. Nonetheless, for each relevant step the influence of each parasitic element is discussed when it is expected to take place.

The first step of the discharge phase – Step ① – starts as soon as the PTGD switch closes. Thus, the output current starts to flow back from the capacitive load through the coupled inductor to charge it with magnetic energy. This current flows through the winding resistance R_s , dissipating an amount of energy equal to $\mathcal{E}_{R_s} = \int R_s \cdot i_{out}^2 dt$ and the total ON-resistance of the PTGD switch. In addition to that, the secondary capacitance C_s captures a portion of energy calculated with $\mathcal{E}_{C_s} = \frac{1}{2} C_s (V_{out} - V_D)^2$. During this step, the secondary leakage inductance L_{ls} prevents a fraction of the energy to flow back to the primary side but it is not included in the final loss count because its energy remains in the secondary side and is later on captured by the other parasitic elements.

During Step ②, the PTGD switch reopens. This leads to commutation losses which are particularly high during the first pulses of the discharge phase because of the high voltage across it but gradually decrease with the voltage manipulated. Additionally, the parasitic capacitances of the coupled inductor's inter-winding C_W and of the PTGD switch capture a portion of energy following the rise of the potential V_D back up to the new value of V_{out} . The amount of energy stored is calculated using $\mathcal{E}_{C_W} = \frac{1}{2} C_W (V_D - V_{M_p})^2$.

Step ③ sees the primary current i_{in} flow through the primary winding resistance R_p and the body diode of the primary switch M_p which dissipate an amount of energy equal to $\mathcal{E}_{R_p} = \int R_p \cdot i_{in}^2 dt$ and $\mathcal{E}_{R_{M_p}} = \int R_{M_p} \cdot i_{in}^2 dt$ where R_{M_p} is here the forward resistance of the body diode.

Finally, as mentioned above, Steps ④ and ⑤ are irrelevant during the discharge phase because of the nonexistence of the back flow of, in this case, input current. Therefore, Step ⑥ comes right after as no more current flows throughout the system. At this point, one can determine how much energy left the load by using $\mathcal{E}_{C_L} = \frac{1}{2} C_L V_{out}^2$ and looking at the difference between the start and the end of the pulse.

Figures 5.29 and 5.30 show the evolution of the energy stored in the relevant elements of the circuit during the first pulse of the discharge phase and the pulse during which the output voltage drops below 1 kV respectively. The data presented in these two figures is the result of a numerical integration applied on the measurements shown previously.

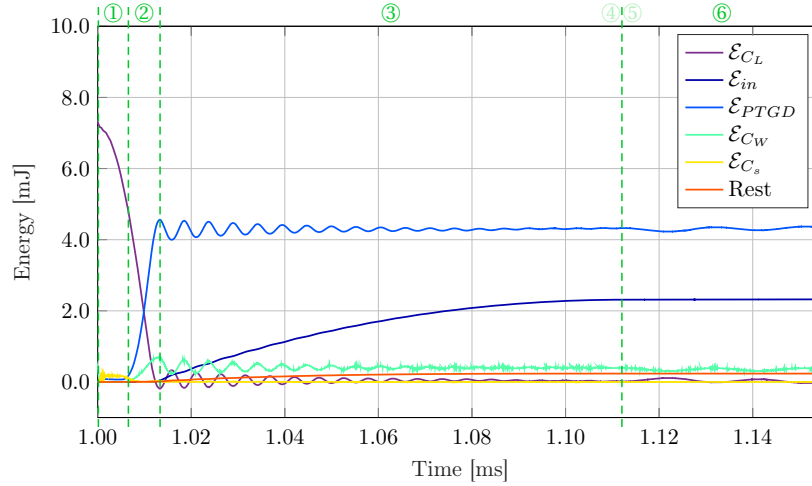


Figure 5.29: Evolution of the energy stored or dissipated by the various elements of the flyback during the first pulse of the discharge phase when the output voltage is at 8 kV. \mathcal{E}_{C_L} represents the difference of energy stored in the load between the beginning and end of the pulse, \mathcal{E}_{PTGD} is the total amount of energy lost due to the PTGD switch which includes its ON-resistance, commutation losses and parasitic capacitance, and the rest is here the sum of the energy stored or dissipated in R_p , R_{M_p} , R_s and the core losses.

5.5.3 Efficiency estimation

Figures 5.31 and 5.32 present an estimation of the distribution of where the energy originating from the load ends up being stored or dissipated during the first pulse of the discharge phase and during the pulse where the output voltage drops below 1 kV respectively.

One of the first things to note is that the vast majority of the energy not recovered is being dissipated and stolen by the PTGD switch. During the first pulse when the output voltage is high, the losses are dominated by commutation losses when the switch reopens because of said high voltage which is directly applied across it. But with the gradual fall of the output voltage those losses are also reduced and more energy is recovered.

For similar reasons, the capacitive elements are a large source of stolen energy during the early pulses at high voltage but they become almost negligible near the end of the discharge phase.

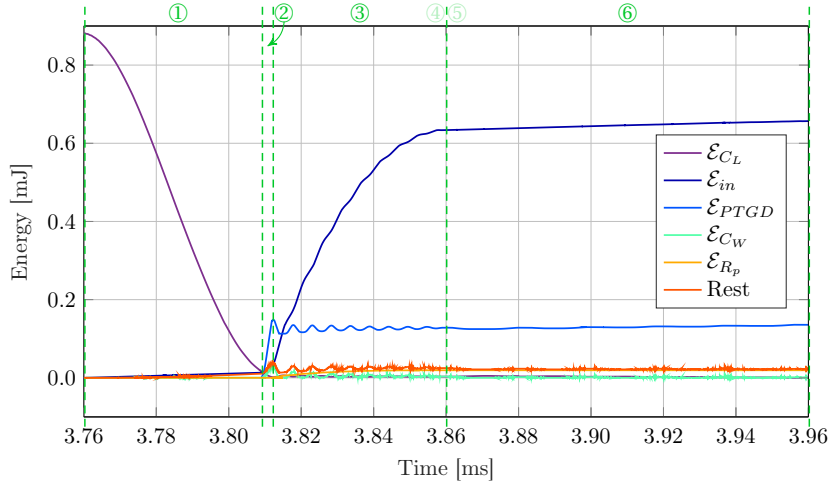


Figure 5.30: Evolution of the energy stored or dissipated by the various elements of the flyback during the pulse where the output voltage drops below 1 kV. The rest is here the sum of the energy stored or dissipated in C_s , R_{Mp} , R_s and the core losses.

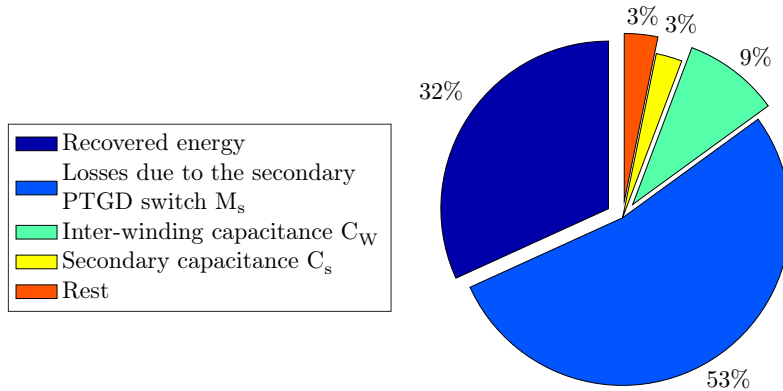


Figure 5.31: Distribution of the energy originating from the capacitive load spread throughout the system during the first pulse of the discharge phase. The rest includes the energy stored or dissipated in R_p , R_{Mp} , R_s and the core losses.

Conversely, with less energy stolen by the parasitic capacitances, the influence of the resistive elements grows because, while the energy they dissipate does not vary significantly in absolute terms throughout the discharge phase, it becomes proportionally larger since less energy is stolen or dissipated elsewhere.

Ultimately, over the course of the brief – only barely more than 3 ms – discharge phase, approximately 43 % of the energy initially stored in the load at the beginning of the discharge phase is recovered.

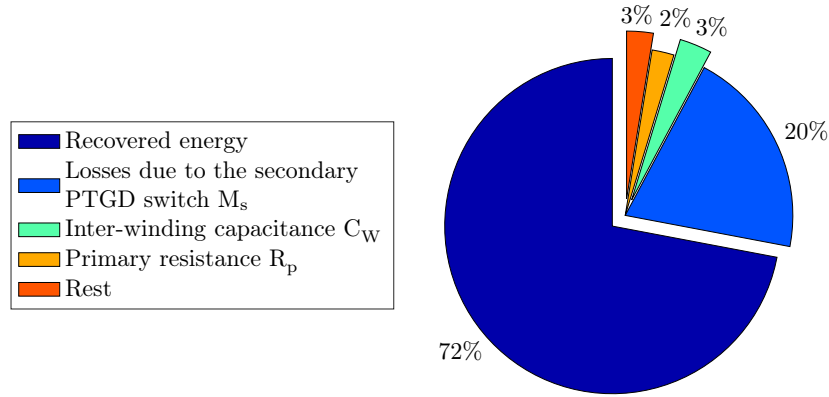


Figure 5.32: Distribution of the energy throughout the system during the pulse of the discharge phase where the output voltage drops below 1 kV. The rest includes the energy stored or dissipated in C_s , R_{M_p} , R_s and the core losses.

5.6 Conclusion

In this chapter, several aspects concerning the manipulation of the high voltages necessary to operate dielectric elastomer actuators were investigated and integrated into the ultra-high voltage flyback converter.

The first aspect concerned the necessity to measure the voltages which will be applied across the capacitive loads. For this purpose, a custom high voltage, high impedance, large bandwidth and compact probe was successfully designed and integrated into the electronics system. By using the well-known voltage divider topology with five $2\text{ G}\Omega$ resistors in series, voltages of at most $\pm 15\text{ kV} - 10\text{ kV}$ confirmed – can be measured with a bandwidth of approximately 7 MHz. A comparison realized with commercially available *Tektronix's* P6015A 20 kV, 100 M Ω oscilloscope probe revealed extremely good performances over the course of one charge-discharge cycle.

The second aspect is about the need for a switch capable to withstand the targeted high voltages in order to enable the bidirectional behavior of the flyback converter to actively discharge the capacitive loads. Indeed, because of the absence of adequate components in the market, a custom high voltage switch had to be designed and was subsequently implemented. The switch makes use of the Pulsed Transformer Gate Drive topology to simultaneously drive three 4.5 kV MOSFETs put in series, effectively creating a 13.5 kV switch. The critical need for a precise voltage balancing across the three switches is also heavily focused on to make sure that the reliability of the system is optimal.

The third aspect touches on the control aspect of the discharge process. Indeed, to safely discharge the capacitive load without risking to damage the electronics, two strategies were investigated. The first one made use of a high-performance ADC module to measure at high

frequency the current flowing through the coupled inductor of the flyback to trigger the reopening of the switch before the saturation of the core. The second is a passive solution consisting of a Schmitt trigger module designed to automatically trigger the reopening of the switch when the monitored current crosses a given threshold. Both solutions have respective pros and cons but ultimately the Schmitt trigger solution was implemented.

Finally, experimental measurements were presented to show how the complete system behaves in various situations throughout the operation of the bidirectional flyback. It was shown that, thanks to the implementation of the aforementioned design considerations, a capacitive load charged at 8 kV could be safely discharged back through the flyback converter itself thus recovering approximately 43 % of the energy initially stored at the beginning. However, it was revealed that the PTGD switch is the source of the vast majority of the losses of energy during any given discharge pulses. It should therefore be the focus of further research and development to improve the overall performances of the system.

Publications related to this chapter :

R. Mottet, M. Almanza, L. Pniak, A. Boegli and Y. Perriard, "*Ultra-High-Voltage (7-kV) Bidirectional Flyback Converter Used to Drive Capacitive Actuators*," in IEEE Transactions on Industry Applications, vol. 57, no. 5, pp. 5145-5156, Sept.-Oct. 2021, doi: 10.1109/TIA.2021.3094460.

R. Mottet, A. Boegli and Y. Perriard, "*Schmitt trigger-based control strategy for the discharge phase of an ultra-high-voltage bidirectional flyback*," in 2021 24th IEEE International Conference on Electrical Machines and Systems (ICEMS), 2021, pp. 232-235, doi: 10.23919/ICEMS52562.2021.9634195.

R. Mottet, A. Boegli and Y. Perriard, "*Control Strategy for the Discharge Phase of an Ultra-High Voltage (>7kV) Bi-Directional Flyback Converter Driving Capacitive Actuators*," in 2020 23rd IEEE International Conference on Electrical Machines and Systems (ICEMS), 2020, pp. 1326-1330, doi: 10.23919/ICEMS50442.2020.9290814.

6 Bidirectional flyback converter with dielectric elastomer actuators

6.1 Introduction

In this chapter, the bidirectional flyback is used to supply the voltages to and recover the energy from tubular dielectric elastomer actuators which are put in increasingly difficult conditions. Thanks to that, the challenges and behaviors originating from this type of load are studied and discussed in detail.

The first study consists of tubular DEAs simply connected to and powered by the flyback converter to investigate their behavior when faced with the impulsive nature of the currents supplied. Indeed, the access resistances of the electrodes play a major role in limiting the increase of the output voltage but also in generating very large voltage spikes across the load which increase the risks of damages to both the load itself and the electronics.

With the voltage spikes issue under control, a typical DEA tube was then sequentially put through increasingly demanding environments. At first, the actuator was initially powered as-is by the electronics to establish the basis for comparison. Then the same tube was put under an increasing amount of static pressure to give a first idea of the tube's behavior in conditions which resemble what can be found in a living body through the help of a water column system.

And finally, this tube was implemented into a flow-loop system which is a test bench designed not only to recreate the pressures varying over time found in the body but also to generate and control a flow a water analogous to the bloodstream in the body.

6.2 Large and variable access resistance capacitive loads

One of the main characteristics of DEAs which makes operating them with a flyback particularly challenging is the resistance of their electrodes. Indeed, due to the way DEAs are manufactured, the resistance of each electrode can range from several tens of kilohms to hundreds of megaohms depending on their carbon composition and geometry (thickness, surface, etc.). As a reminder, Fig. 6.1 displays the electrical model of a DEA with two resistors R_e representing the electrodes in series with a capacitor.

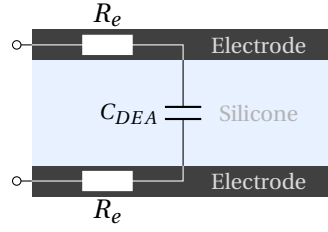


Figure 6.1: Basic electrical model of a Dielectric Elastomer Actuator where R_e is the resistance of the electrodes.

Naturally, it is very advantageous to have the smallest access resistances possible for two main reasons. First, the overall efficiency of the system will be severely impacted the larger these resistances are because of the Joule losses limiting how high the output voltage can reach across a DEA. But more importantly, the impulsive nature of the current supplied to the load has the unfortunate side-effect of generating very large voltage spikes at the output of the flyback across the load which would occasionally lead to voltage breakdowns through the DEA. Figure 6.2 presents a series of measurements obtained on a planar DEA directly connected to the flyback converter which show the behavior of the output voltage in relation to the output current for various amounts of energy stored in the coupled inductor. The energy is directly linked to the duration during which the input current is left flowing to charge the coupled inductor.

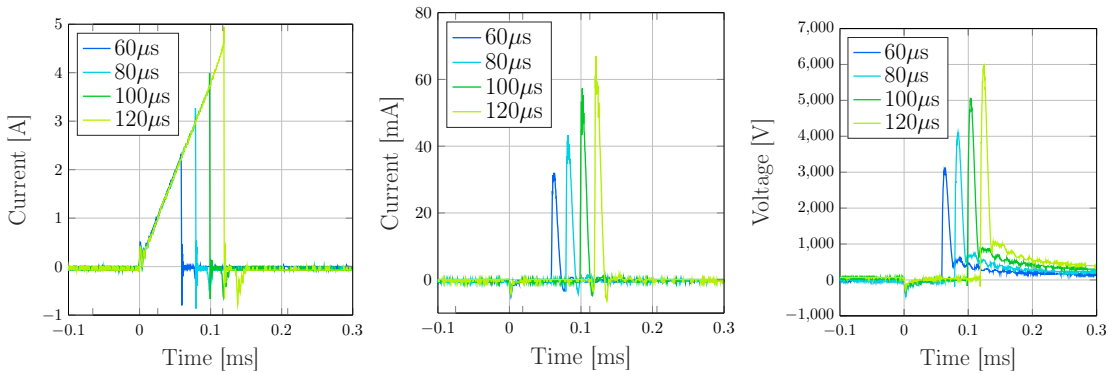


Figure 6.2: Measurements showing the voltage spikes (right) due to the impulsive output current (middle) for various amounts of energy stored in the coupled inductor. The energy is linked to the amount of time during which the input current (left) is allowed to flow to charge said coupled inductor.

Due to the physical nature and large resistance of the electrodes, when the energy is released from the coupled inductor the DEA briefly appears like an open circuit. The precise reason behind this behavior is not yet fully understood but it is believed that it may be due to the electric charges needing a non-negligible amount of time to move and evenly spread all over the electrodes.

Consequently, during this time, the charges can accumulate in the secondary parasitic capacitance of the coupled inductor as well as at local entry points of the electrodes. This, in turn, makes it so that the voltage can easily exceed the threshold tolerated by the dielectric material thus leading to a local breakdown.

To overcome this issue, an approach considered was to investigate if some steps of the manufacturing process could be changed to reduce these resistances. However, the options available were very limited. Indeed, modifying the geometry of the electrodes was not ideal because changing their surface would influence the active zone of a DEA tube and thus its volume variation, and therefore the amount of energy it could provide to the circulatory system. As for increasing their thickness, this would increase the overall rigidity of the actuator which would reduce its ability to deform itself. A modification of the recipe of the carbon ink to increase the carbon content was also out of bounds because of the potential stiffening of the DEA.

The remaining option ended up being making modifications to the silver access lines guiding the current from the converter to the carbon electrodes such that, rather than simply going across each electrode, an additional perpendicular line was added all along the electrodes to form T-shaped access lines as depicted in Fig. 6.3.

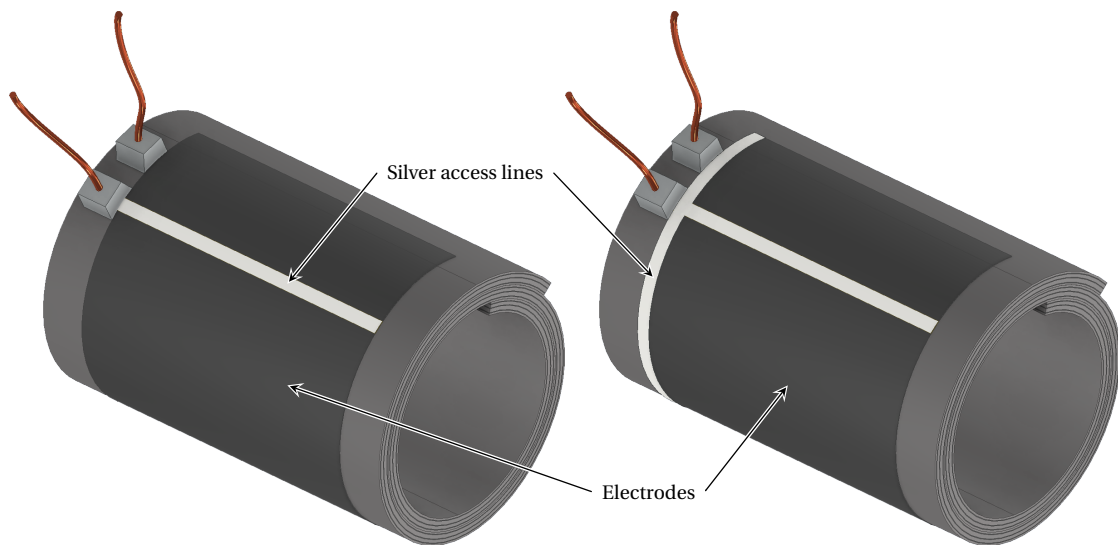


Figure 6.3: On the left, the original placement of the silver line and, on the right, the T-shaped silver access lines.

The idea was that it would help lower the resistance by giving additional entry points for the charges to enter into the electrodes, thus reducing the chance of local breakdowns. However, experiments showed that the resistance was not sufficiently reduced to have enough of an impact on the voltage spikes as shown in Fig. 6.4 and that new parasitic elements were added, amplifying unwanted oscillations.

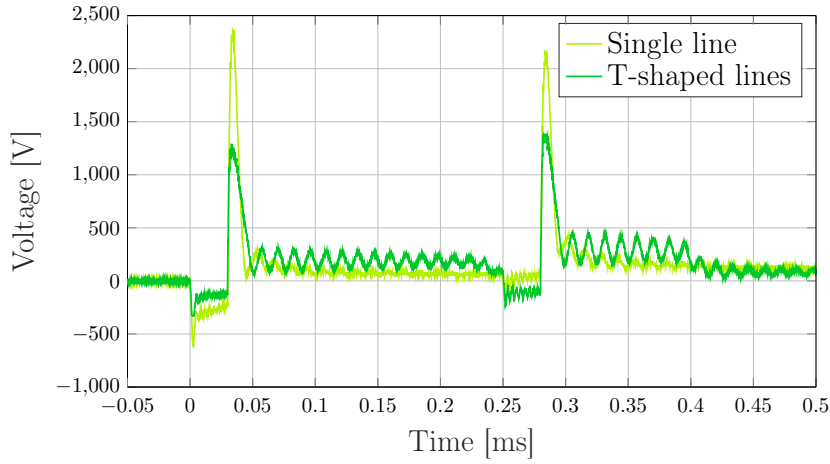


Figure 6.4: Comparison of the effect of the modification of the silver access lines on the output voltage spikes measured on two different DEA tubes. With T-shaped silver lines, the resistance is reduced but not enough to completely negate the voltage spikes experienced by a DEA tube.

Ultimately, a solution coming from the electronics was necessary but was revealed to be extremely simple. By adding a capacitor at the output of the flyback in parallel to the DEA load, it was observed that the bulk of the charges would be first absorbed by the capacitor effectively dampening the spike of current and thus leaving more time for the charges to spread around the electrodes. Figure 6.5 presents measurements of the voltage across and current flowing through a DEA tube connected to the flyback once without any parallel capacitor and once with a 2.4 nF capacitor. One can clearly see that the current and corresponding voltage spikes are drastically reduced after integrating the aforementioned capacitor.

Additionally, one can notice that, despite the fact that adding a capacitor in parallel to the DEA will reduce the ability of the flyback to reach high voltages (as discussed in Chapter 3), the benefits brought by it far outweigh this disadvantage because fewer Joule losses happen through the resistance of the electrodes thanks to the reduced current amplitude.

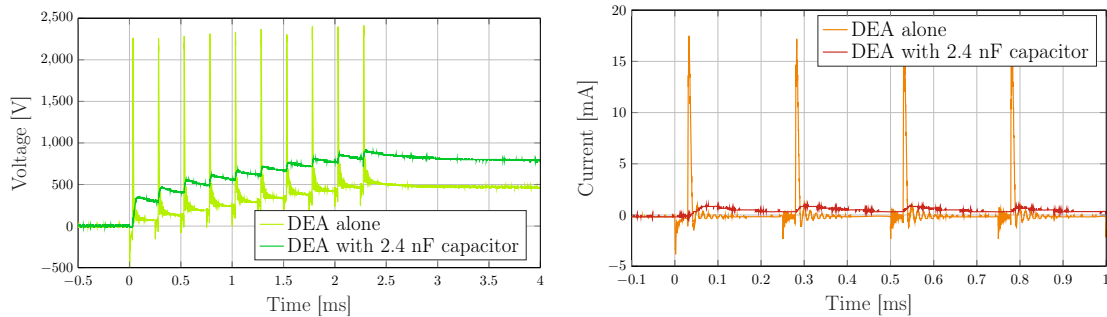


Figure 6.5: Measured voltage across (left) and current flowing through (right) a DEA tube connected to the flyback converter. Once without and once with a 2.4 nF capacitor placed in parallel to the DEA.

6.2 Large and variable access resistance capacitive loads

Naturally, a balance must be found regarding the capacitance of this parallel capacitor between the damping of the current spikes and the overall ability of the flyback to supply high voltages. Indeed, it was determined thanks to simulations done in LTSpice with the model in Fig. 6.6 that actually a smaller capacitance of around 1 nF than the 2.4 nF previously tested offered the best compromise with reasonable voltage spikes and a larger final output voltage. Figure 6.7 shows the results of three simulation runs during each of which a different capacitance value was tested: 2.4 nF, 1 nF and 0.1 nF.

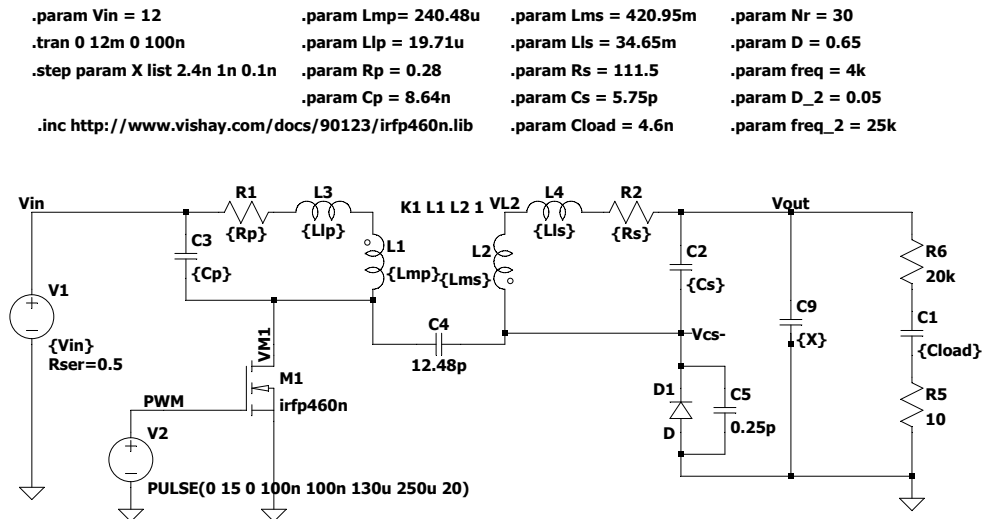


Figure 6.6: Model implemented in LTSpice to simulate the influence of various capacitance values put in parallel to a DEA to dampen current and their respective voltage spikes. Here, the capacitor C9 is consecutively worth 2.4 nF, 1 nF and 0.1 nF.

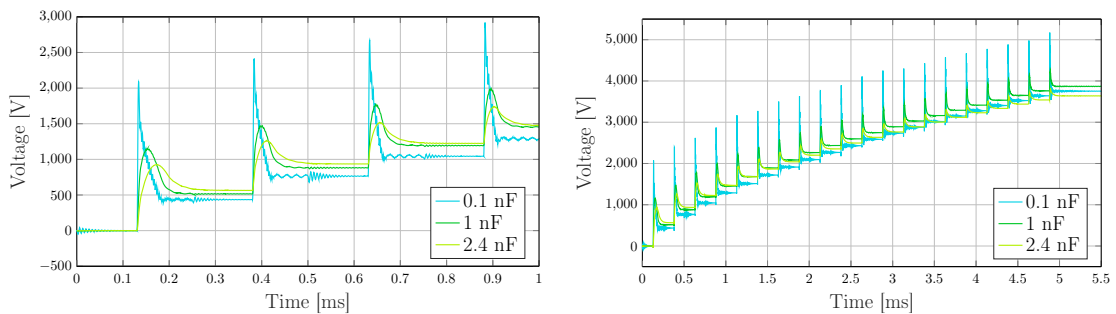


Figure 6.7: Output voltages resulting from the three consecutive simulation runs of the flyback connected to a DEA with capacitor C9 having a different value during each run.

These results were subsequently confirmed through actual measurements obtained with the flyback while it powered a DEA tube. Indeed, Fig. 6.8 displays two measurements for which two capacitance values – 1 nF and 2.4 nF – were used. One can see the same behavior as expected from the simulations which is that the DEA tube with the smaller capacitance of

1 nF experienced slightly larger voltage spikes but still performed better with a higher output voltage reached. In the end, the 1 nF capacitor was kept for the experiments of the following sections.

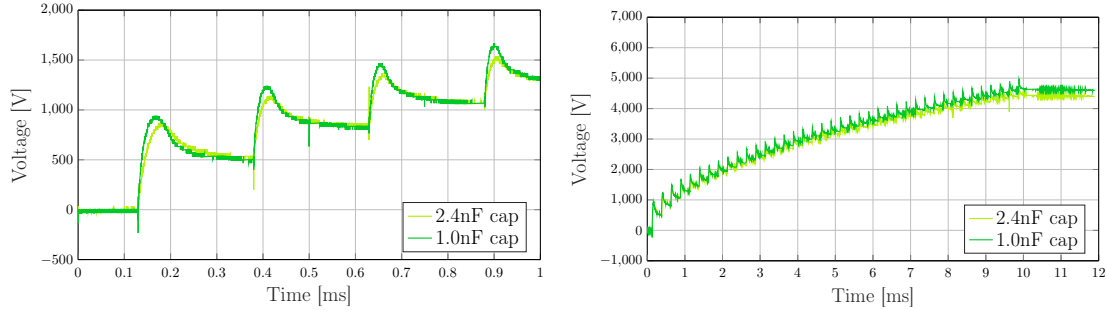


Figure 6.8: Measurements obtained with the flyback showing the effects of the capacitance value of the additional capacitor put in parallel to a DEA tube. A smaller capacitance means larger voltage spikes as shown on the left but also potential voltage gains due to the smaller capacitance as shown on the right.

One note, however, is that this capacitance value may not necessarily be the optimal value for every DEA and may have to be redetermined if the capacitance and resistances of a given DEA are significantly different to the values used here which correspond to those of the actuator used hereafter.

6.3 Pressurized DEA tubes

With the impulsive nature of the flyback and corresponding voltage spikes under control, DEA tubes such as the one of Fig. 6.9 could now be reliably and safely powered to voltage levels high enough for them to significantly deform and thus be put into increasingly more realistic situations. The first series of measurements were done with the water column setup shown in Fig. 6.10. The testing setup works as follows: a DEA tube laying horizontally to maintain a uniform pressure inside as much as possible is connected at the bottom of a structure on which a Plexiglas tube is located. This latter tube with an inner diameter of 18.5 mm is then filled with water to various heights to produce various pressures. The characteristics of the DEA tube used can be found in Table 6.1.

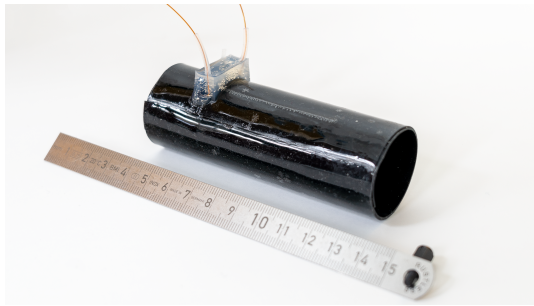


Figure 6.9: Photography of the DEA tube used in the pressure experiments.

Parameter	Value
Tube inner diameter	30 mm
Capacitance	~4.6 nF
Electrode resistance	~20 k Ω
Electrode surface	190 x 49 mm
Dielectric thickness	100 μ m
Dielectric material	Elastosil 2030
Dielectric strength	100 V/ μ m
Active layers	4

Table 6.1: Characteristics of the DEA used to obtain the measurements hereafter.

The purpose of this test system is to put DEA tubes under various levels of pressure ranging from 70 to 100 mmHg which are pressures they are expected to experience, for the moment, in the body of a pig. The interest behind this experiment is that it allows to study how DEAs and the electronics behave when put under constant pressures. This gives an initial idea of how much the voltage across the DEA will vary over the span of the aforementioned pressure range and thus can give valuable information e.g. for voltage control purposes in future iterations of the electronics.

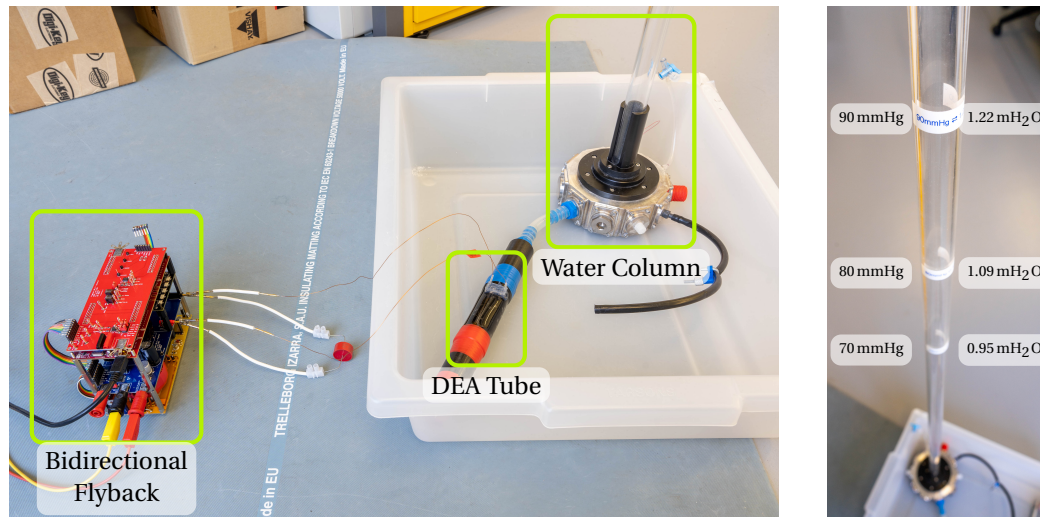


Figure 6.10: Setup for the water column experiment. On the left image are displayed the bidirectional flyback connected to a DEA tube. The latter is plugged to a water column system which allows to simulate inside the tube pressures which are expected to be found in a living body. The right image shows some of the labels indicating the equivalent water height necessary to apply a pressure given in millimeter of mercury with a water column 18.5 mm in diameter.

Indeed, this added pressure already deforms the DEA tube connected even before it is powered. As such, some of its electrical characteristics are affected but most notably its capacitance. The radial expansion of the tube due to the pressure means that the surface of the electrodes increases but also that the thickness of the DEA diminishes. It is therefore expected for the capacitance to increase with the pressure applied and thus that, for an equal amount of energy stored in the load, the output voltage reached across the load will be reduced as the pressure increases. Figure 6.11 shows the voltage measured across the same DEA tube under various pressures when the same amount of energy is supplied each time.

The results from this experiment confirm the previously discussed expectations that the capacitance varies with the pressure. Moreover, they also tell us that we can expect the voltage to vary by at least approximately 6 % from 4.6 kV to 4.3 kV if the pressure were to change from 70 mmHg to 100 mmHg during a single cycle. Additionally, one can notice that the voltage continues to decrease slightly during the resting phase at high voltage. This is due to the inertia of the water moved as the diameter of the tube increases.

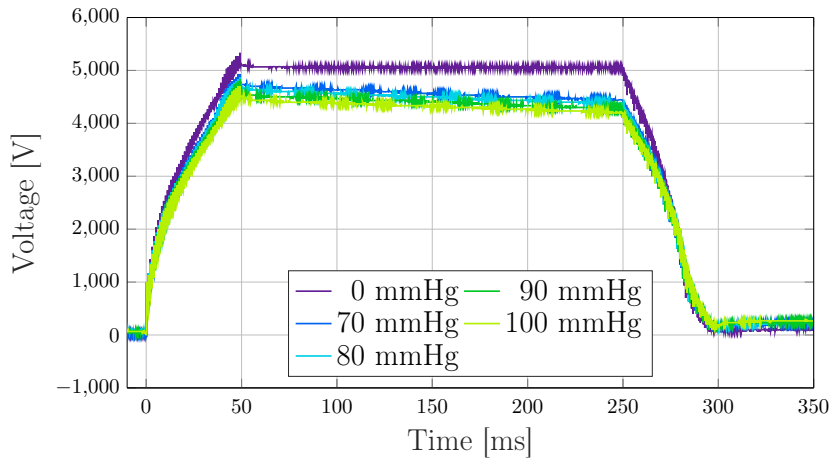


Figure 6.11: Measured output voltage across a DEA tube under pressures ranging from 70 to 100 mmHg compared to the voltage when the tube is empty with a constant input of energy. The voltage clearly drops as the pressure increases in the tube because of the radial expansion of the tube which increases the actuator's capacitance.

Finally, these measurements also reveal that, from an electronics control perspective, it will be necessary to finely tune the charge phase by increasing the amount of energy pulses as well as the frequency to make sure that the output targeted is reached within the allotted time span regardless of the pressure currently in the tube. This will be necessary to maximize the deformation of the tube and thus the amount of energy that the device can provide to the bloodstream.

6.4 DEA tubes under dynamic pressure

The next step to confirm that the electronics is capable to reliably power DEA tubes in the most challenging conditions is to put a DEA tube under dynamic pressure. Indeed, as mentioned earlier, the pressure measured in the aorta (the aortic pressure) right after the heart continuously varies depending on the phase of the heartbeat as shown in Fig. 6.12. One must note that the pressures indicated in this diagram correspond to those of a human body which are slightly higher than those mentioned throughout this chapter because the first targeted recipients of DEA tubes are pigs.

Since the DEA tube is destined to be located around the aorta right after the heart and because repeatedly testing in situ is not a realistic option, a test bench was designed to recreate the varying pressures and blood flow found in a human or pig's body by using water. Figure 6.13 presents a photograph of the so-called *flow-loop* which was used to obtain the measurements presented hereafter.

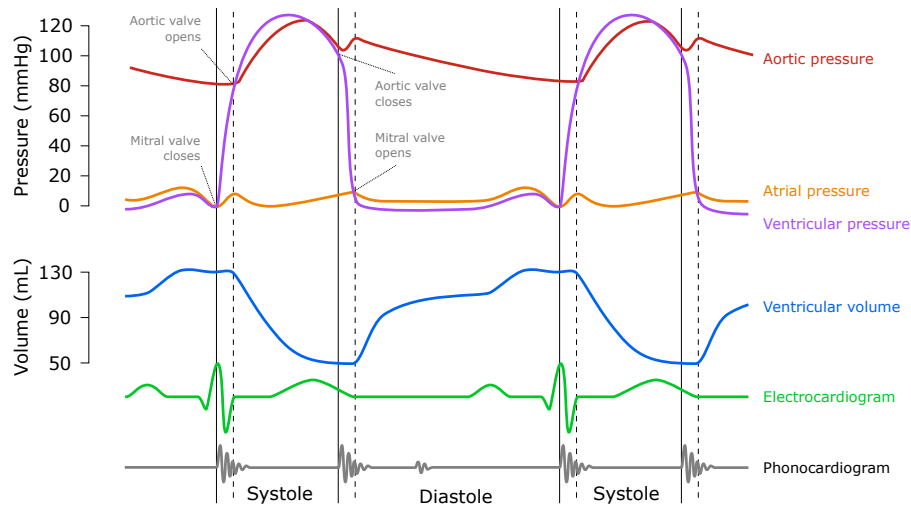


Figure 6.12: Wiggers diagram [57] of a typical human cardiac cycle but analogous to the a pig's one. During the systole phase the heart contracts to eject the blood stored in the ventricles into the circulatory system. At that moment the aortic valve opens and the pressure increases in the aorta. It is then followed by the diastole phase during which the heart relaxes which allows new blood to fill back up the ventricles and the aortic pressure slowly decreases .

This setup is composed of four main parts : the flow pump which generates the blood/water flow by moving a piston back-and-forth at a fixed frequency close to that of a heart (60 to 100 bpm); the left ventricle and atrium chamber in which the ventricular pressure is recreated thanks to valves limiting the flow of water and the pump pushing the water; the compliant chamber and flow resistor which are designed to simulate the behavior of the rest of a body's circulatory system; and finally, the DEA tube powered by the flyback converter located between the two pressure chambers where the aorta would be found to help push the water further down the system when synced with the beating of the heart/flow pump.

Figure 6.14 displays a simplified schematic of the system as seen from above to show more precisely the location of the various chambers and of the sensors used. Two pressure sensors were installed to measure the aortic and the ventricle pressure in their respective chambers, and a laser was setup to measure the deformation experienced by the DEA tube throughout the experiment. Additionally, the front view of the left ventricle and atrium chamber is also shown to indicate the location of both the aortic and mitral valves.

For this experiment, the pulsation generated by the flow pump was set to 100 bpm and the compliant chamber and flow resistor were adjusted so that during each cardiac cycle the pressure would constantly vary between 70 to 100 mmHg. Then, while the system was in motion, the DEA tube was powered and synchronized with the "heart" beats for 5 cycles after which the flow-loop continued to operate normally. The powering of the DEA was then repeated several times with different voltages to investigate the influence of this parameter on the system. Figure 6.15 shows the measurements obtained with the smallest (2.5 kV) as well as the largest (4.2 kV) voltages tested.

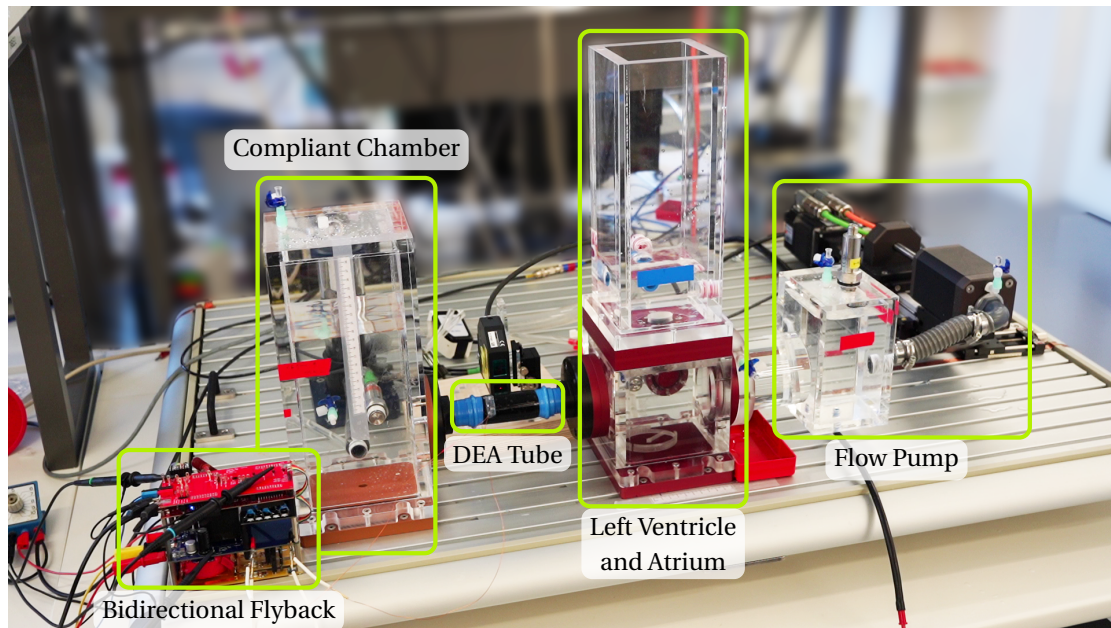


Figure 6.13: Setup for the flow-loop experiment. A tube powered by the bidirectional flyback is located between two chambers filled with water. The left ventricle and atrium chamber coupled with the flow pump are used to simulate the behavior of the left side of the heart. The compliant chamber and the flow resistor (see Fig. 6.14) recreate the pressure conditions in the rest of the circulatory system.

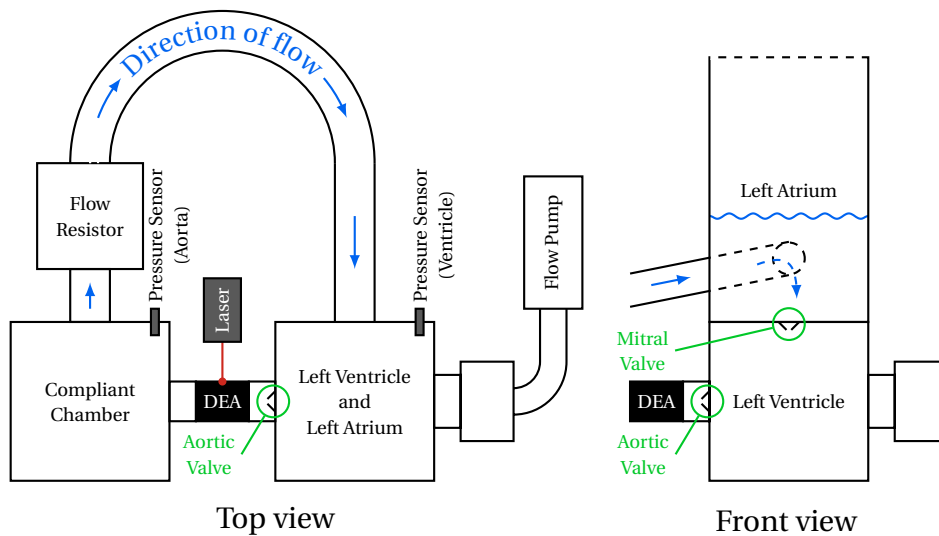


Figure 6.14: Schematic representation of the flow-loop test bench as seen from the top and from the front. The location of the various sensors used to obtain the measurements presented in this section is shown. The laser is used to measure the deformation of the DEA tube, the aortic pressure sensor measures the pressure in the compliant chamber, and the ventricle pressure sensor measures the pressure in the left ventricle chamber.

6.4 DEA tubes under dynamic pressure

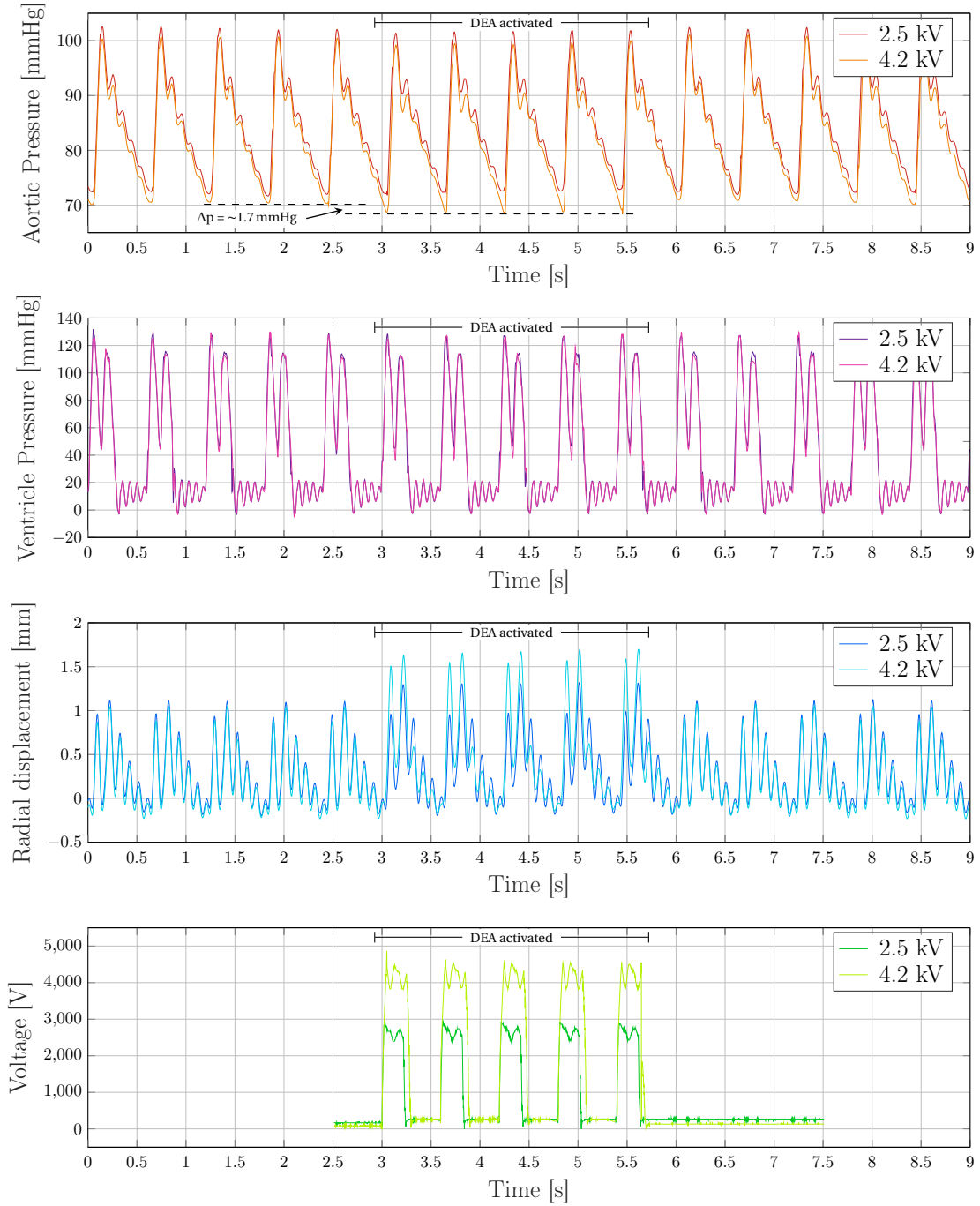


Figure 6.15: Measurements obtained on the flow-loop test bench. Two sets of measurements are displayed which correspond to two values of voltage applied to the DEA tube during operation. At 2.5 kV the tube does not deform itself sufficiently to have an impact on the aortic pressure as opposed to a voltage of 4.2 kV. At the latter voltage, the diameter of the tube increases by about 5 mm and thus the aortic pressure drops from 100.5/70.3 mmHg down to 99.3/68.6 mmHg.

The maximum voltage was kept low during this experiment to protect the tube from risks of voltage breakdown and the flow-loop system from potential short-circuits through the water. Nevertheless, the final goal is to supply at least 6 kV which the electronics is without a doubt capable of doing. The tube used is the same as in the water column experiment.

One can notice that, in the case of the lower voltage, almost no difference is perceptible between before and during the activation. This is expected because this voltage level remains too low to significantly deform the actuator. Whereas in the second set of measurements, the diameter of the tube increases by 5 more millimeters (approximately a 16 % increase of diameter) compared to when it is not powered. Consequently, this leads to a notable reduction of the aortic pressure range from 100.5/70.3 mmHg down to 99.3/68.6 mmHg or approximately a 2.2 % decrease. Considering that the voltage supplied is far from the 6 kV to even potentially 8 kV which such a tube can withstand, one can reasonably expect a much more significant reduction of pressure in the future.

Finally, when looking at the influence of the pressure on the voltage across the load into more details e.g. in the 4.2 kV case, one can notice that, compared to the results obtained in the water column experiment presented in Fig 6.11, the voltage variation is larger – dropping as low as 3.8 kV – despite working in the same pressure range of 70 to 100 mmHg. Indeed, the measurements shown in Fig. 6.16 reveal that there seems to be a significant influence of the dynamic pressure change on the voltage. This means that the pressure alone is not the only factor influencing the output voltage but it also appears that the speed at which this pressure varies may also be important and thus could warrant further investigation.

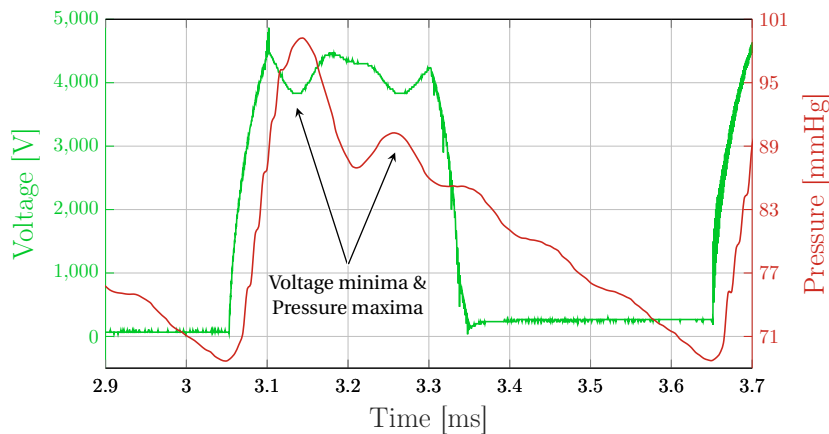


Figure 6.16: It was shown in Fig. 6.11 that with an increasing but constant pressure, the voltage across a DEA tube is dropping. However, the flow-loop experiments revealed that the dynamic pressure change also has a significant influence as shown here by the inverse relationship between the pressure change and the output voltage.

One can also observe that when the tube is brought back to its original shape as the voltage drops back down to 0 V, the pressure oscillations are damped. It would be interesting to investigate this behavior further to see if some of the pressure variations could be damped e.g. by adapting the voltage when the pressure increases with a dynamic control of the voltage.

6.5 Conclusion

In this chapter, the experiments were realized thanks to the bidirectional flyback actively charging DEAs in various shapes and forms, but also recovering some of the electrical energy stored in them at the end of their actuation cycle. These experiments thus show that the bidirectional flyback is capable to supply the voltage levels required. But most importantly, that DEA tubes destined to be used as part of the body circulatory system were reliably powered while said tubes were put in increasingly challenging environments.

The first series of experiments were centered around the need to make sure that DEAs could be reliably and safely operated with the flyback. Indeed, DEAs experience extremely large voltage spikes across their electrodes because of the impulsive nature of the current supplied by the flyback converter and because of their large access resistances. In the end, after numerous attempts at modifying the tube themselves, a simple yet ingenious solution consisting of adding a capacitor in parallel to the DEA to absorb the bulk of the current pulse was put in place. This allowed to significantly reduce those voltage spikes which in turn resulted not only in reduced risks of voltage breakdowns but also in improved performances with larger output voltages reached despite the additional capacitance added.

The second series of experiments consisted of studying the behavior of the flyback converter when powering DEA tubes put under constant but increasing amounts of pressure. Indeed, because the pressure within the bloodstream of a pig varies significantly between 70 to 100 mmHg depending on the state of the heart, it was necessary to investigate if and how the pressurization of a DEA tube would influence the behavior of the electronics. This was achieved by using a water column filled to various heights to apply pressure to a DEA connected at its bottom. It was showed that increasing the pressure was modifying the physical properties of the DEA tube and therefore its electrical ones as well. Namely the capacitance which increased with the pressure and thus reduced the output voltage measured across the actuator from 5 kV without pressure down to 4.3 kV with 100 mmHg when a constant amount of energy was supplied.

Finally, the bidirectional flyback was set to power a DEA tube implemented into a flow-loop system to investigate how dynamic variations of the pressure within a DEA tube would influence the electronics system. The flow-loop consists of a series of chambers filled with water pushed around by a piston pumping at a constant frequency similar to that of a heart. Thanks to a series of valves this complete system recreates the pressure conditions and blood flow found in a body. Through this experiment it was confirmed that the pressure was a significant factor influencing the voltage found across the actuator. But in addition to that it was observed that the speed at which the pressure varies may be an additional factor worth further investigation. It was also noticed that as the voltage fell back down to 0 V and the actuator came back to its original shape, the pressure oscillations in the circulatory system were damped. As such, it was suggested that a dynamic control of the voltage should be implemented not only to compensate for the voltage variations but also to try to dampen unwanted pressure oscillation.

7 Conclusion, contributions & outlook

7.1 Conclusion

The research undertaken in this thesis is centered around the technology of dielectric elastomer actuators but done from an electronics point of view. Indeed, DEAs belong to an emerging and promising technology which is capable to mimic some of the behaviors of natural muscles and as such they are of very high interest for medical applications such as in the form of the heart assisting device being designed in EPFL's Center for Artificial Muscles.

In the first part of the investigation for the state of the art, a description of DEAs is proposed to present in detail the challenges and needs this technology imposes upon the electronics. Namely that extremely high voltages ranging between 5 kV to 20 kV are necessary to operate such actuators to the maximum of their abilities, and that, due to their layered physical structure and thus capacitive nature, a large amount of electrical energy can end up stored in the actuators themselves. Energy which must be removed to complete an actuation cycle of a DEA. With common practices consisting of simply dissipating this energy through resistive elements in the form of heat which is problematic for applications destined to operate inside a living body, a new strategy was required to improve the efficiency of such a system. As such, the second part of the state of the art focuses on voltage amplifying power electronics topologies with the goal to determine which is the most suitable to face the aforementioned challenges. Ultimately, the DC/DC flyback converter was selected.

Following this selection process, the working principle of the flyback topology is studied in great details to uncover which factors are limiting its ability to supply the several thousands of volts necessary. It was concluded that the main culprits are the parasitic capacitive elements found mainly in the coupled inductor – the centerpiece of the topology – but also in some secondary components such as diodes and MOSFETs. Thus, several strategies and manufacturing techniques aiming at reducing these elements as much as possible are carefully investigated and listed. Strategies to choose the most adequate core to maximize the energy it stores while minimizing its size, and techniques to carefully select and implement the winding topology which minimizes the parasitic capacitances. These strategies are in the end put in

place and their influence analyzed through an energy efficiency estimation which reveals that approximately 60 % of the energy input into the flyback was transferred to the capacitive load with the latter being charged at 8 kV in less than 9 ms. This result also shows that there is room left for further improvements such as the need to find the optimal balance between the leakage inductance and the parasitic capacitance as they are inversely proportional and the former reduces the overall efficiency of the system.

With an effort to lay the groundwork to find this balance between the two latter parameters, an analytical model depicting the flyback converter during its charge phase – the phase during which the voltage increases across a capacitive load – is developed. Thanks to this early model, it is now not only possible to confirm that the parasitic capacitances are the main limiting factor for the voltage amplification with the flyback but also show how influential each distinct capacitance is in the complete system. Moreover, an estimation of the maximum theoretical output voltage reachable by the manufactured flyback is realized and thus, it was calculated that one could not expect the converter to supply more than 12 kV in its current form.

To meet the second requirement imposed by DEAs to recover the electrical energy stored in them at the end of an actuation cycle, the flyback was modified to work bidirectionally. Indeed, by integrating a switch on the secondary, high voltage side of the flyback it is now possible to send this stored energy back to the power source. However, due to the voltage levels to manipulate, no conventional and commercially available solutions currently exist. As such, through the implementation of the pulsed transformer gate drive topology, an ultra-high voltage switch could be created by placing three high voltage (4.5 kV) MOSFETs in series to one another. Additionally, two control strategies to drive this switch are investigated in order to safely and reliably discharge the load through the flyback. The first makes use of a high performance ADC module to monitor the currents flowing through the load and the second is based on the Schmitt-trigger topology. In the end, an efficiency analysis is also performed on the discharge phase of the load. This reveals that, on average, approximately 43 % of the energy could be recovered from the load in the power source. This low result is mostly due to the HV switch which is the source of a large amount of losses and thus should be the first component of the circuit to be worked on to further improve the efficiency of the system.

Ultimately, the complete ultra-high voltage bidirectional flyback converter is tasked to drive a tubular DEA pump put in various and increasingly challenging environments to confirm its ability to meet the requirements imposed by dielectric elastomer actuators. At first, DEAs are directly connected to the converter to study the influence such a load could have on the electronics. Indeed, due to the way they are manufactured, the electrodes have extremely large resistances which generate equally large voltage spikes when the impulsive current supplied by the current flows through them. After solving the issues this process revealed, a DEA tube is put under various constant amounts of pressure – from 70 mmHg to 100 mmHg – to give a first idea of how such an actuator would behave when faced with the pressure levels that it is bound to face inside a living body. Finally, this same tube is placed in a test bench – a *flow-loop* system – designed to recreate the dynamic variations of pressure found in the aorta

close to the heart by pumping water with an external piston through chambers separated by valves as is the case with a heart.

From this last experiment it is shown that not only the designed bidirectional flyback converter is capable to operate DEA tubes in as real-like conditions as possible, but also that the DEA tube is indeed capable to reduce the pressure inside the aorta as the CAM hoped. Indeed, an approximately 2.2 % decrease is achieved with voltages currently well below the breakdown limit (for the safety of the equipment) of the actuator.

7.2 Contributions

The main scientific contributions as they are described throughout this thesis can be summarized as follow :

Detailed study and modeling of the working principle of the flyback

The deep dive into the working principle of the flyback converter was a process not yet undertaken with a high voltage generation mindset in mind. Indeed, this revealed itself to be critical for the proper understanding of the limitations of the topology regarding the generation of high voltages.

Critical design consideration for the generation of high voltages

Thanks to this understanding of the working principle, design considerations could be listed which, when implemented, will have the effect of allowing the flyback converter to supply voltages to capacitive loads significantly higher than previously achieved with this topology.

Development of an analytical model of the charge phase

The development of the analytical model describing the charge phase of the actuation cycle of a DEA opens to the door to optimization processes to take place so that the efficiency of the system can be further improved and its overall physical size subsequently reduced.

Enabling of efficient controlled discharge of DEAs

As mentioned earlier, the most common way to discharge DEAs was done by dissipating the energy they store through resistive elements. Thanks to the implementation of a HV switch, the bidirectional nature of the flyback was enabled and allowed to work at much higher voltages than previously done. Thus, DEAs can now be controlled much more efficiently which is critical for portable and in-body medical applications.

Compact voltage amplifying electronics

Despite the large size of some of the components used in the bidirectional flyback converter, the sum of all the previous contributions results in an extremely compact and portable electronics considering the voltages it is capable to supply compared to what was previously available both in the market and in previous research works.

7.3 Outlook

While it is the dream of every Ph.D. student to be able to explore every nooks and crannies of one's thesis subject, it is unfortunately impossible to do so within a reasonable time span. As such, many new doors opened themselves during this thesis through which it was not possible to go to discover what laid behind. Thus, below are some of the research aspects which would be worth investigating further.

Coupled inductor miniaturization and optimization

Concerning the miniaturization, one must note that the custom made coupled inductor that was used in the last iteration of the electronics was designed to be capable to meet the needs of many different DEA tubes with ever-changing characteristics because of the continuous development undertaken to improve their performances. However, as soon as a final design will be selected, it should be possible to determine more precisely the actuator's energy and voltage needs and, thus, a dedicated and smaller coupled inductor could be designed and manufactured.

Nevertheless, the reduction of the parasitic capacitances of the coupled inductor will remain a critical design aspect which will also require further optimization. Indeed, it was noticed that the reduction of capacitance is achieved to the detriment of the leakage inductance. Despite the fact that this does not hinder the flyback's ability to supply high voltages, it significantly influences the efficiency of the system. Therefore, a detailed optimization of the inductor would be greatly valuable as it would not only allow to have fewer losses but also could help further reduce the physical size of this component. An option to consider to achieve this would be to implement topology optimization principles to design a winding topology as dense as possible which would both minimize the leakage inductances and the parasitic capacitances.

Improved analytical models

The model presented here only touches upon the charge phase of the actuation cycle of a DEA. It would thus be incredibly interesting to develop a similar model for the discharge phase as it could help locate potentially overlooked sources of losses during this time in order to improve the discharge efficiency. Additionally, integrating more complex DEA models could reveal and explain less well understood behaviors such as the interaction of the large and variable access resistances with the current and the rest of the flyback.

Development of a compact ultra-high voltage switch

This part of the electronics presented in this thesis is the one with the most potential for improvements and miniaturization. Indeed, while the PTGD topology used to drive three 4.5 kV MOSFETs in series works well, the volume it takes is probably its main downside. Therefore, two leads could be worth investigating.

The first would be to try to optimize the PTGD switch by reducing the size of its components. Namely, its transformer and the control electronics of the MOSFETs. Doing so would mean that the transformer would reach saturation faster but this could easily be taken into account in the control software to prevent the switch to remain closed for too long (as is already done). The consequence of this would just be more discharge pulses but, as it was shown, they can be quite fast. Changing the MOSFETs themselves might be difficult simply because of their package size. Indeed, working with smaller MOSFETs would mean more MOSFETs to put in series since their respective voltage breakdown would be lower as well. Other than increased risks of voltage imbalance across them, because of the available packages the total PCB footprint would probably remain as large as the current system.

To other much more technical and difficult but equally interesting solution oriented towards the field of micro and nanotechnologies would be to work on the development of SiC MOSFETs similar to those mentioned in Chapter 5. Indeed, it appears that they can be made to withstand tens of kilovolts in reasonably sized packages which would be a complete game changer. These new MOSFETs would however need to have very low leakage currents and be very fast at closing and opening.

Control for DEA applications

An aspect of the electronics only briefly touched upon in this thesis was its voltage control strategy. It was here quite rudimentary with pulses of energy sent at a fixed frequency during the charge phase. The implementation of a solution to dynamically adapt the period of these pulses could enable a significantly finer control of the voltage increase across the load. Additionally, the feedback about the output voltage offered by the HV probe designed in this work could be used to drive the voltage during the resting phase to counteract the dynamic pressure variations – and thus voltage variations – experienced by DEA tubes in a body.

Finally, other works in the literature showed that DEAs have self-sensing capabilities and as such it could be interesting to investigate this possibility to enable a dynamic synchronization of the electronics with the beating of the heart by sensing when the pressure in the DEA pump increases following the contraction of the heart to react accordingly.

Powering via wireless power transfer

Finally, the next step to complete the system destined to be implemented in a living body consists of making sure that the flyback converter can be powered via inductive wireless power transfer. Initial investigations and tests done within the CAM showed that it should not be a problem but this remains to be done appropriately.

A Bill of materials

The complete ultra-high voltage bidirectional flyback converter is composed of 4 different printed circuit board to make it as compact as possible. All of the boards have received nicknames related to their respective roles within the converter system: the *Flyback* board which contains the core elements of the flyback such as the coupled inductor, primary switch, etc.; the *Control* board which includes the MOSFET drivers, the Schmitt trigger module, etc.; the *HV divider* board which consists of the high voltage probe discussed in Section 5.2.1; and finally, the *HV switch* board which is the PTGD switch described in Section 5.3.

The following tables list the components used on each of these boards.

Designator	Type	Footprint	Parameter	Description	Quantity
GND, VD, Vin_Lp, Vout	Test Point	Header 1x1	Male	2.54mm, 1-pin header	4
C1	Capacitor	6050	22 μ F	MLCC	1
C2	Capacitor	SVP F12	330 μ F	ALU	1
C3	Capacitor	5-12.6	1000 μ F	Electrolytic	1
C4	Capacitor	0805	0.1 μ F	Standard	1
D1	Diode	HVEF12P	12 kV, 20 mA	HVEF12P	1
H1	Connector	Header 8x1	Male	2.54mm, 8-pin header	1
H2	Connector	Header 6x1	Male	2.54mm, 6-pin header	1
H3	Connector	Header 2x1	Male	2.54mm, 2-pin header	1
P1, P2, P3	Connector	Custom	Female	4 mm banana socket	3
P4, P5	Connector	PB 1101	Female	2 mm Test Jack	2
Q1	N-MOSFET	TO-220FP	650 V, 80 m Ω SiC FET	UJ3C065080T3S	1
R1	Resistor	0805	10 Ω	0.1 %	1
T1	Coupled Inductor	Custom	See Table 3.6	Custom made by Rotima AG	1
U1	Current Sensor	CQ-3201	Sensing range ± 10.1 A	SMD coreless Hall sensor	1

Table A.1: Bill of material of the *Flyback* board

Appendix A. Bill of materials

Designator	Type	Footprint	Parameter	Description	Quantity
1000:1, 5000:1, Vadd OUT, Vcmp, Vcmp IN, Vdiv, Vin2, Vin-, Vin+, Vout cmp, Vshunt, Vref cmp, VgsMp, VgsMs, VMp, Ip 3.3V, Ip 5V, Mp ctrl, Ms ctrl	Test Point	Header 1x1	Male	2.54mm, 1-pin header	19
C1	Capacitor	0805	1.2 μ F	Standard	1
C2	Capacitor	0805	4.7 μ F	Standard	1
C3	Capacitor	0805	1 μ F	Standard	1
H1	Connector	Header 8x1	Female	2.54mm, 8-pin header	1
H2	Connector	Header 6x1	Female	2.54mm, 6-pin header	1
H3	Connector	Header 2x1	Male	2.54mm, 2-pin header	1
H4	Connector	Header 4x2	Male	2.54mm, 4x2-pin header	1
LPXL	Pin Layout	Custom	External Board	Launchpad XL 28379D	1
P1, P2	Connector	PB 1101	Female	2 mm Test Jack	2
P3, P4	Connector	Custom	Female	4 mm banana socket	2
R1, R4	Resistor	0805	3.3 k Ω	Standard	2
R2, R3	Resistor	0805	1 k Ω	Standard	2
R5, R6	Resistor	0805	22 Ω	Standard	2
R7	Resistor	0805	4.7 k Ω	Standard	1
R8	Resistor	0805	1.2 k Ω	Standard	1
R9	Resistor	0805	1 k Ω	Standard	1
U1	Driver	SOIC8	Dual low-side	IX4427NTR	1
U2	Comparator	SOT-23-5	High speed, Rail-to-rail	TLV3201	1
U3	OpAmp	SOIC8	Low noise	AD8652	1
VR1, VR2	Variable Resistors	ST-5EW	5 k Ω	ST5ETW502	2

Table A.2: Bill of material of the *Control* board

Designator	Type	Footprint	Parameter	Description	Quantity
1000:1, Vout	Test Point	Header 1x1	Male	2.54mm, 1-pin header	2
C1, C2, C3, C4, C5	Capacitor	CC45	22 pF, 6 kV	CC45SL3JD220JYGNA	5
C6	Capacitor	0805	820 pF	Standard	1
C7	Capacitor	0805	3.3 nF	Standard	1
C8	Capacitor	0805	1 μ F	Standard	1
H1	Connector	Header 6x1	Female	2.54mm, 6-pin header	1
R1, R2, R3, R4, R5	Resistor	2512	5 G Ω , 10 kV	UHV B2512FCD2G00CT	5
R6	Resistor	0805	10 M Ω	Standard	1
U1	OpAmp	RD-8-1	Low noise, Wide bandwidth	ADA4625-1	1
U2	DC/DC Converter	IZ 8-pin	Input 12 V, Output \pm 15 V	IZ1215S	1

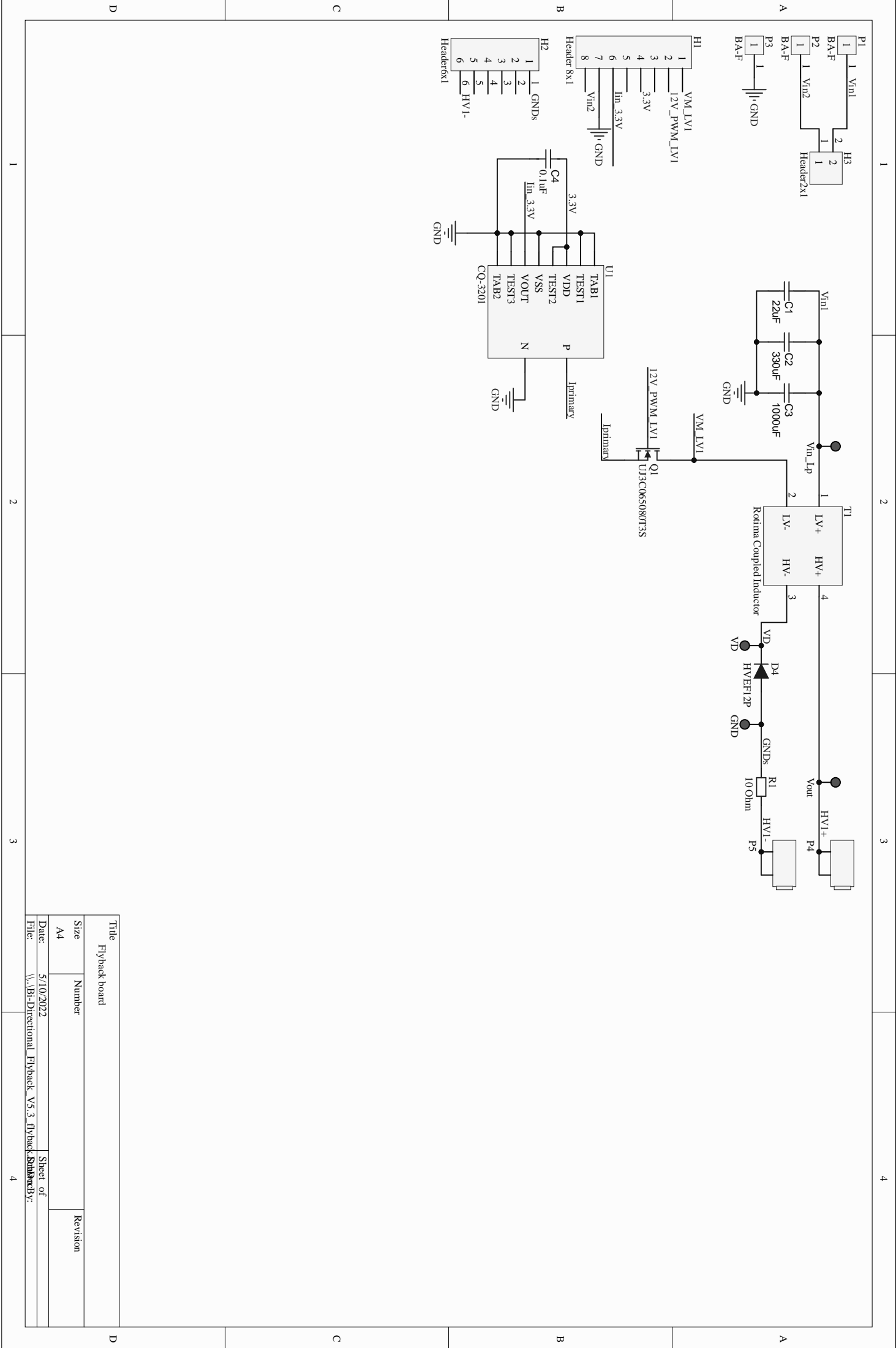
Table A.3: Bill of material of the *HV divider* board

Designator	Type	Footprint	Parameter	Description	Quantity
Top+, Top-, Mid+, Mid-, Bot+, Bot-, Demag+, Demag-, GND, VD, VMtop, VMmid, VMbot	Test Point	Header 1x1	Male	2.54mm, 1-pin header	2
C1, C2, C3	Capacitor	CC45	Variable, 6 kV	CC45SL3JD___JYGNA	3
C4	Capacitor	2.5-6	100 μ F	Standard	1
D1	Diode	HVEF12P	12 kV, 20 mA	HVEF12P	1
D2, D6, D9	Diode	DO-35	General purpose	1N914B	3
D3, D5, D7, D8, D10, D11	Diode	DO-35	Zener diode	BZX55	6
D4	Diode	DO-201AD	High surge current	SB360	1
H1	Connector	Header 8x1	Female	2.54mm, 8-pin header	1
P1	Connector	Custom	Female	4 mm banana socket	1
Q1, Q2, Q3	Transistor	TO-18	PNP Transistor	2N2907A	3
R1, R4, R7	Resistor	0805	10 Ω	Standard	3
R2, R5, R8	Resistor	0805	3.3 k Ω	Standard	3
R3, R6, R9	Resistor	AXIAL-0.4	100 Ω	Standard	3
U1, U2, U3	N-MOSFET	ISOPLUS i4-Pak	4.5 kV, 200 mA	IXTF02N450	3
U4	N-MOSFET	TO-220FP	650 V, 80 m Ω SiC FET	UJ3C065080T3S	1

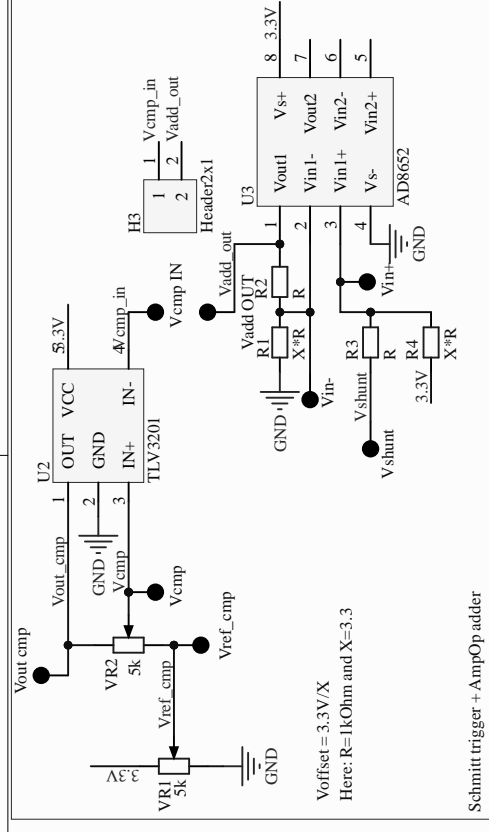
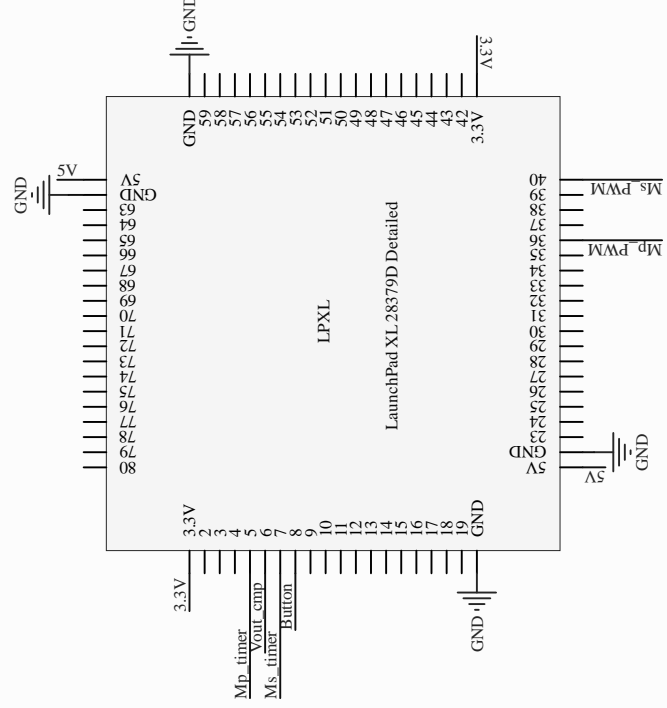
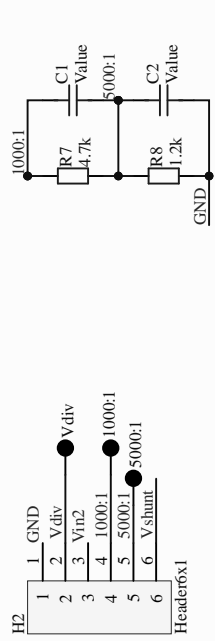
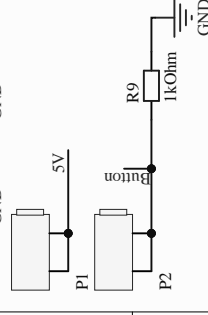
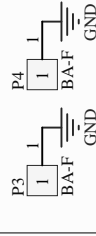
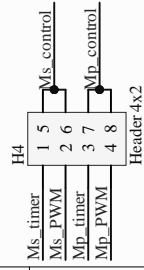
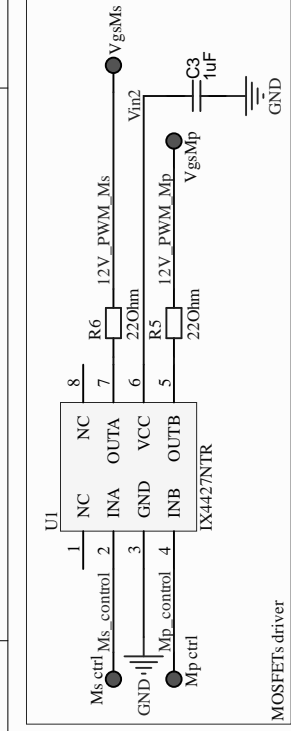
Table A.4: Bill of material of the *HV switch* board

B Electronics schematics

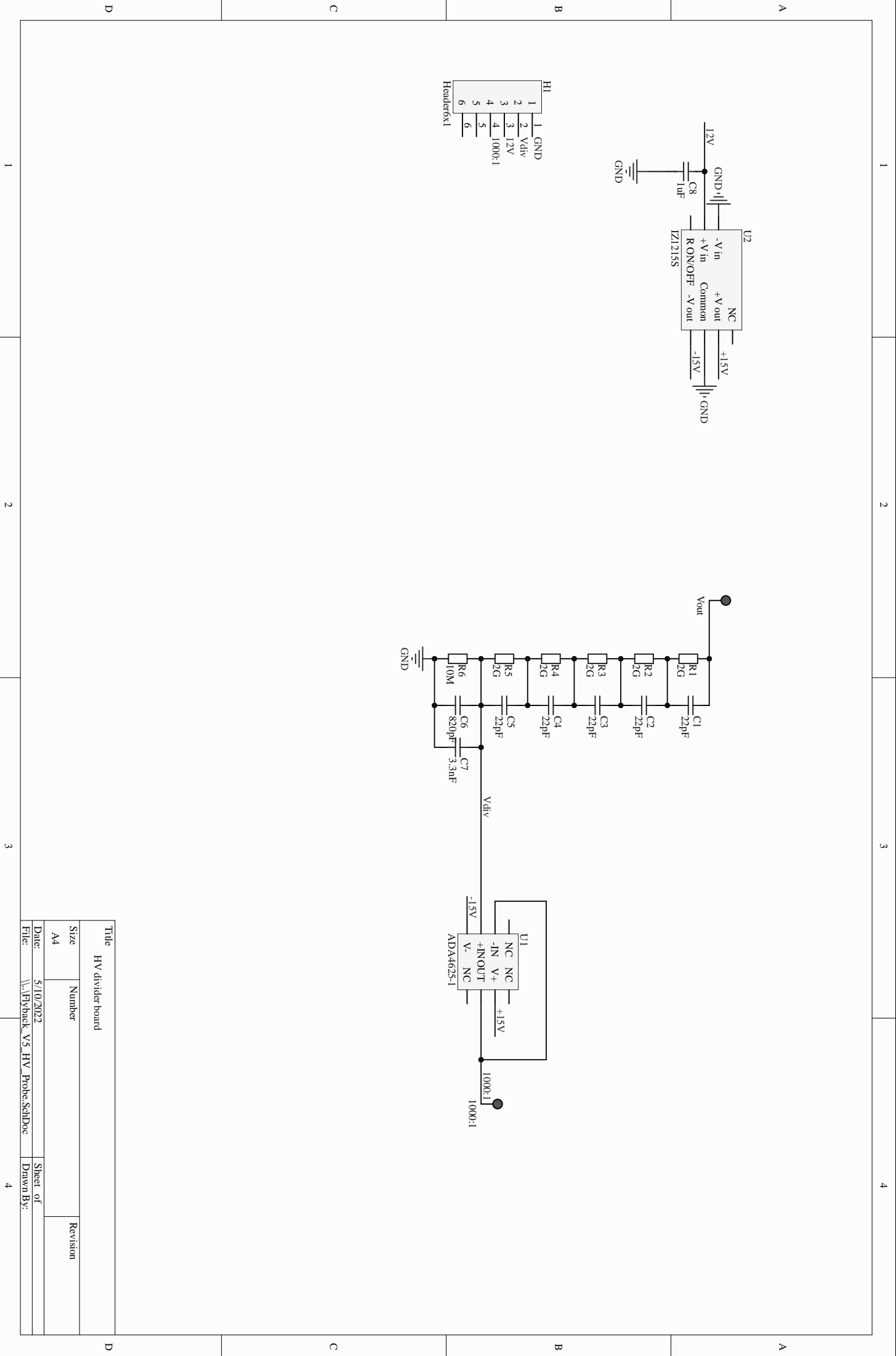
The schematics of each of the boards that are a part of the final bidirectional flyback converter can be found in the upcoming pages.



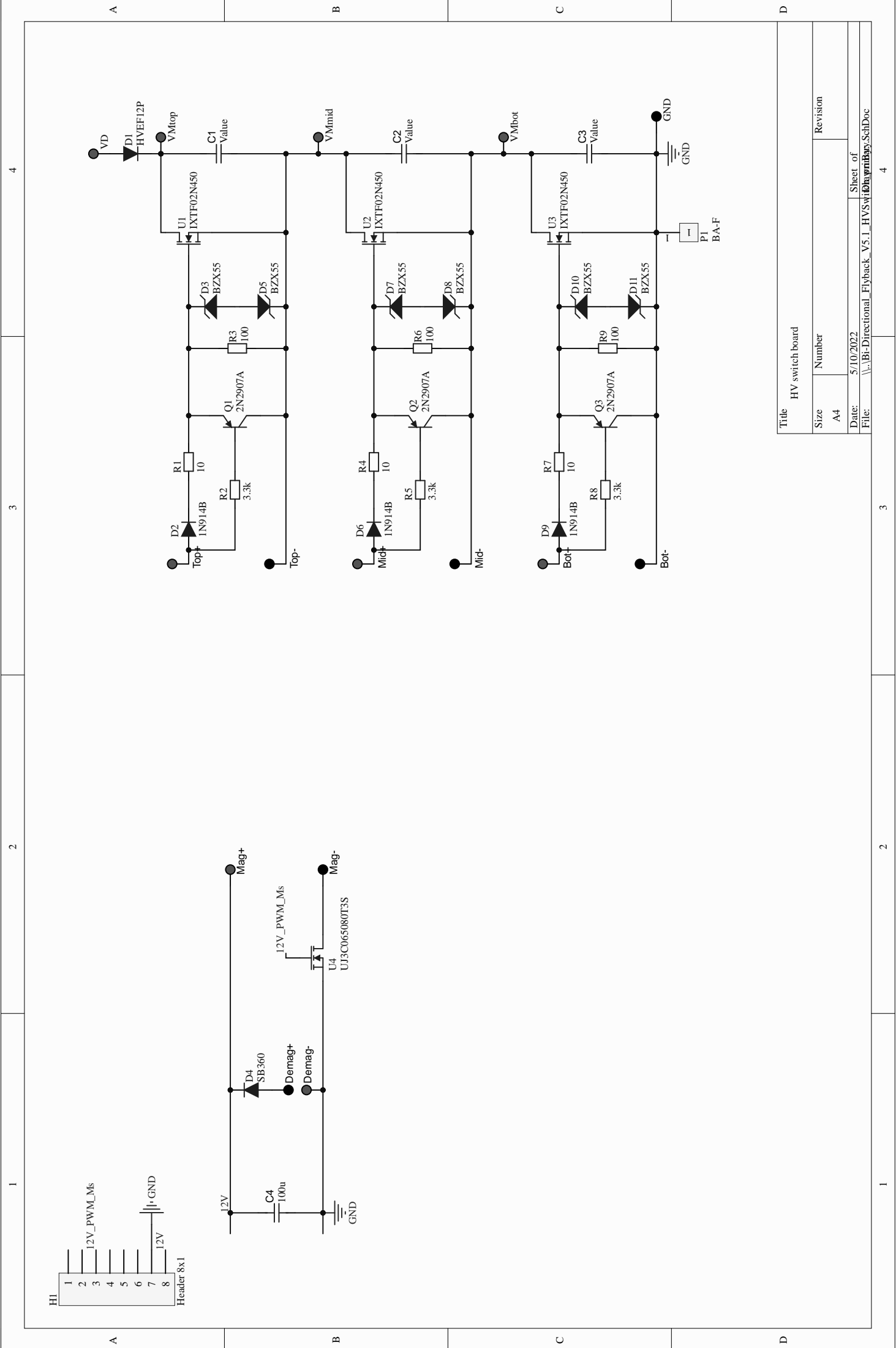
Title			
Flyback board			
Size	Number		Revision
A4			
Date:	5/10/2022	Sheet of	
Title:	\\.\B-D\Directional Flyback_V5.3_Flyback Board.Brd		



Control board		
Size	Number	Revision
A4		
Date:	5/10/2022	
File:	\\11-Bi-Directional Flyback_V5.3_control_board.dwg	
		Sheet of 3



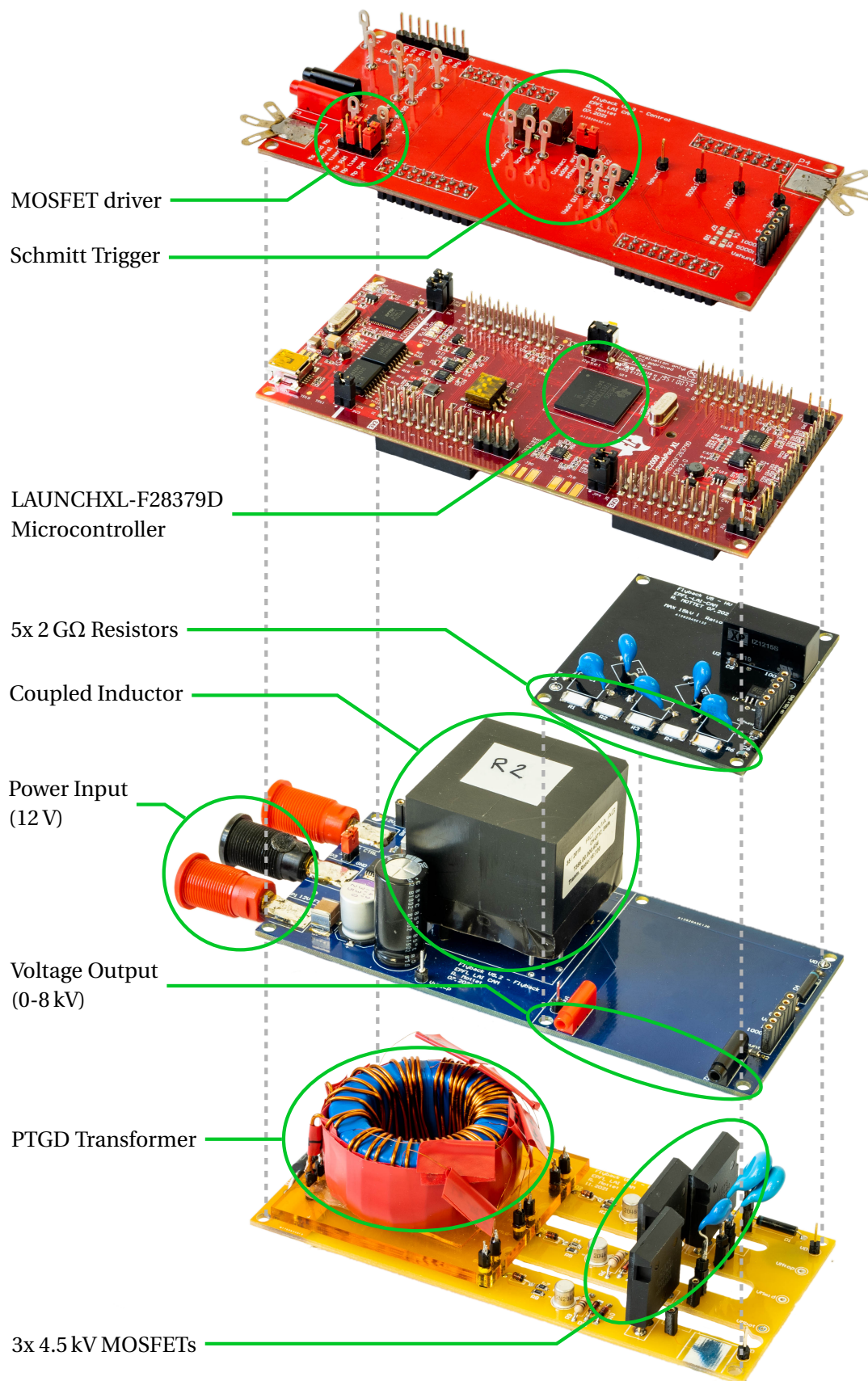
Title			Revision	
HV divider board				
Size	Number			
A4				
Date:	5/10/2022	Sheet of		
File:	\\.\Hyback_V5_HV_Probe.SchDoc	Drawn By:		



C Exploded view of the flyback converter

On the following page, an exploded view of the ultra-high voltage bidirectional flyback converter is presented. For each boards the location of their main components and modules is highlighted.

Appendix C. Exploded view of the flyback converter



Bibliography

- [1] World Health Organization. *Cardiovascular diseases (CVDs)*. June 2021. URL: [https://www.who.int/en/news-room/fact-sheets/detail/cardiovascular-diseases-\(cvds\)](https://www.who.int/en/news-room/fact-sheets/detail/cardiovascular-diseases-(cvds)) (visited on 05/04/2022).
- [2] European Heart Network. *Heart Failure and Cardiovascular Diseases*. Apr. 2019. URL: <https://ehnheart.org/publications-and-papers/publications/1202:.html> (visited on 05/04/2022).
- [3] Madhero88 for Wikipedia. *Ventricular assist device*. Licensed under CC BY-SA 3.0. Apr. 2010. URL: https://commons.wikimedia.org/wiki/File:Ventricular_assist_device.png (visited on 05/04/2022).
- [4] A. Sen et al. “Mechanical circulatory assist devices: a primer for critical care and emergency physicians”. In: *Critical care* 20.1 (2016), pp. 1–20.
- [5] C. Heilmann et al. “Haemolysis in patients with ventricular assist devices: major differences between systems”. In: *European journal of cardio-thoracic surgery* 36.3 (2009), pp. 580–584.
- [6] T. Martinez et al. “A novel soft cardiac assist device based on a dielectric elastomer augmented aorta: an in vivo study”. In: *Bioengineering & Translational Medicine* (Under review).
- [7] J. B. Young. “Healing the heart with ventricular assist device therapy: mechanisms of cardiac recovery”. en. In: *The Annals of Thoracic Surgery* 71.3, Supplement 1 (Mar. 2001), S210–S219.
- [8] R. Pelrine et al. “High-field deformation of elastomeric dielectrics for actuators”. In: *Materials Science and Engineering: C* 11.2 (2000), pp. 89–100.
- [9] R. Pelrine et al. “High-Speed Electrically Actuated Elastomers with Strain Greater Than 100%”. In: *Science* 287.5454 (Feb. 2000), pp. 836–839.
- [10] R. D. Kornbluh et al. “Electroelastomers: applications of dielectric elastomer transducers for actuation, generation, and smart structures”. In: *Smart Structures and Materials 2002: Industrial and Commercial Applications of Smart Structures Technologies*. Vol. 4698. International Society for Optics and Photonics, July 2002, pp. 254–270.

Bibliography

- [11] Q. Pei et al. “Multifunctional electroelastomer rolls and their application for biomimetic walking robots”. In: *Smart Structures and Materials 2002: Industrial and Commercial Applications of Smart Structures Technologies*. Vol. 4698. International Society for Optics and Photonics, July 2002, pp. 246–253.
- [12] J. Shintake et al. “Versatile Soft Grippers with Intrinsic Electroadhesion Based on Multifunctional Polymer Actuators”. In: *Advanced Materials* 28.2 (2016), pp. 231–238.
- [13] P. Thummala et al. “A high voltage DC-DC converter driving a Dielectric Electro Active Polymer actuator for wind turbine flaps”. In: *2012 47th International Universities Power Engineering Conference (UPEC)*. Sept. 2012, pp. 1–7.
- [14] G. Mao et al. “Design and Characterization of a Soft Dielectric Elastomer Peristaltic Pump Driven by Electromechanical Load”. In: *IEEE/ASME Transactions on Mechatronics* 23.5 (Oct. 2018), pp. 2132–2143.
- [15] I. A. Anderson et al. “Multi-functional dielectric elastomer artificial muscles for soft and smart machines”. In: *Journal of Applied Physics* 112.4 (Aug. 2012).
- [16] Wacker. *ELASTOSIL Film 2030*. datasheet. URL: <https://www.wacker.com/h/en-us/c/elastosil-film-2030/p/000038005> (visited on 05/04/2022).
- [17] Z. Suo. “Theory of dielectric elastomers”. In: *Acta Mechanica Sinica* 23.6 (Dec. 2010), pp. 549–578.
- [18] B. Rechenbach, M. Willatzen, and B. Lassen. “Theoretical study of the electromechanical efficiency of a loaded tubular dielectric elastomer actuator”. In: *Applied Mathematical Modelling* 40.2 (Jan. 2016), pp. 1232–1246.
- [19] M. Almanza et al. “Towards the material limit and field concentration smoothing in multilayer dielectric elastomer actuators”. In: *Smart Materials and Structures* 29.4 (Mar. 2020), p. 045044.
- [20] X. Ji et al. “Stretchable composite monolayer electrodes for low voltage dielectric elastomer actuators”. In: *Sensors and Actuators B: Chemical* 261 (May 2018), pp. 135–143.
- [21] I. Aghabali et al. “800-V Electric Vehicle Powertrains: Review and Analysis of Benefits, Challenges, and Future Trends”. In: *IEEE Transactions on Transportation Electrification* 7.3 (Sept. 2021), pp. 927–948.
- [22] N. Shibata, T. Tanaka, and M. Kinoshita. “Development of a 3.2MW Photovoltaic Inverter for Large-Scale PV Power Plants”. In: *2018 International Power Electronics Conference (IPEC-Niigata 2018 -ECCE Asia)*. May 2018, pp. 3929–3933.
- [23] Z. Čorba et al. “Future of high power PV plants — 1500V inverters”. In: *2017 International Symposium on Power Electronics (Ee)*. Oct. 2017, pp. 1–5.
- [24] IXYS. *4.5kV MOSFET. IXTH02N450HV* datasheet. URL: https://www.mouser.ch/datasheet/2/240/ixys_s_a0001274125_1-2272693.pdf (visited on 05/04/2022).
- [25] Advanced Energy. *High Voltage Amplifiers*. Trek 20/20C-HS overview. URL: <https://www.advancedenergy.com/products/high-voltage-products/high-voltage-amplifiers/standard-high-speed-amplifiers/trek-2020C-hs/> (visited on 05/04/2022).

-
- [26] G. Palumbo and D. Pappalardo. "Charge Pump Circuits: An Overview on Design Strategies and Topologies". In: *IEEE Circuits and Systems Magazine* 10.1 (2010), pp. 31–45.
- [27] W. Qian et al. "A Switched-Capacitor DC–DC Converter With High Voltage Gain and Reduced Component Rating and Count". In: *IEEE Transactions on Industry Applications* 48.4 (July 2012), pp. 1397–1406.
- [28] C.-S. Chan, W.-H. Ki, and C.-Y. Tsui. "Bi-directional integrated charge pumps". In: *2002 IEEE International Symposium on Circuits and Systems*. Vol. 3. May 2002, pp. III–III.
- [29] Voltage Multipliers Inc. *7kV Surface Mount Multiplier*. VM1566 datasheet. URL: <https://www.voltagemultipliers.com/wp-content/uploads/2018/10/VM1566.pdf> (visited on 05/04/2022).
- [30] L. Eitzen, T. Hoffstadt, and J. Maas. "Power electronics concepts for driving EAP actuators". In: *Electroactive Polymer Actuators and Devices (EAPAD) 2013*. Vol. 8687. International Society for Optics and Photonics, Apr. 2013, p. 86870D.
- [31] M. Almanza et al. *Adaptation of a Solid State Marx Modulator for Electroactive Polymer*. Under review.
- [32] J. Sabate et al. "Design considerations for high-voltage high-power full-bridge zero-voltage-switched PWM converter". In: *Fifth Annual Proceedings on Applied Power Electronics Conference and Exposition*. Mar. 1990, pp. 275–284.
- [33] S. Inoue and H. Akagi. "A Bidirectional Isolated DC–DC Converter as a Core Circuit of the Next-Generation Medium-Voltage Power Conversion System". In: *IEEE Transactions on Power Electronics* 22.2 (Mar. 2007), pp. 535–542.
- [34] B. Yang et al. "Design and Analysis of a Grid-Connected Photovoltaic Power System". In: *IEEE Transactions on Power Electronics* 25.4 (Apr. 2010). Conference Name: IEEE Transactions on Power Electronics, pp. 992–1000.
- [35] N. M. L. Tan, T. Abe, and H. Akagi. "Design and Performance of a Bidirectional Isolated DC–DC Converter for a Battery Energy Storage System". In: *IEEE Transactions on Power Electronics* 27.3 (Mar. 2012), pp. 1237–1248.
- [36] F. L. Tofoli et al. "Survey on non-isolated high-voltage step-up dc–dc topologies based on the boost converter". In: *IET Power Electronics* 8.10 (2015), pp. 2044–2057.
- [37] D. R. Northcott, S. Filizadeh, and A. R. Chevretils. "Design of a bidirectional buck-boost dc/dc converter for a series hybrid electric vehicle using PSCAD/EMTDC". In: *2009 IEEE Vehicle Power and Propulsion Conference*. Sept. 2009, pp. 1561–1566.
- [38] P. Thummala et al. "Digital Control of a High-Voltage (2.5 kV) Bidirectional DC-DC Flyback Converter for Driving a Capacitive Incremental Actuator". In: *IEEE Transactions on Power Electronics* 31.12 (Dec. 2016), pp. 8500–8516.
- [39] P. Thummala et al. "Efficiency Optimization by Considering the High-Voltage Flyback Transformer Parasitics Using an Automatic Winding Layout Technique". In: *IEEE Transactions on Power Electronics* 30.10 (Oct. 2015), pp. 5755–5768.

- [40] T. Hoffstadt and J. Maas. "Comparison of Bidirectional Power Electronics with Unidirectional Topologies Using Active Discharging Circuits for Feeding DEAP Transducer". In: *Electroactive Polymer Actuators and Devices (EAPAD) 2015*. Vol. 9430. International Society for Optics and Photonics, Apr. 2015.
- [41] H. Owen et al. "A computer-aided design procedure for flyback step-up DC-to-DC converters". In: *IEEE Transactions on Magnetics* 8.3 (Sept. 1972), pp. 289–291.
- [42] A. G. Deshpande. "Novel regulation method for low-current, high-voltage-output flyback DC-DC converter with isolation". In: *Journal of Physics E: Scientific Instruments* 11.3 (Mar. 1978), pp. 194–195.
- [43] Y. Shimada et al. "A beam-index TV receiver for consumer application". In: *IEEE Transactions on Consumer Electronics* 35.3 (Aug. 1989), pp. 334–342.
- [44] T. Marchesan et al. "An electronic ballast to supply automotive HID lamps in a low frequency square waveform". In: *Fourtieth IAS Annual Meeting. Conference Record of the 2005 Industry Applications Conference, 2005*. Vol. 3. Oct. 2005, 1598–1602 Vol. 3.
- [45] R. Mottet et al. "Critical Parasitic Elements of Coupled Inductors for Ultra-High Voltage Flyback Converters Used to Drive Capacitive Actuators". In: *2019 22nd International Conference on Electrical Machines and Systems (ICEMS)*. Aug. 2019, pp. 1–5.
- [46] J. Ferrieux and F. Forest. *Alimentations à Découpage, Convertisseurs à Résonance*. pp. 254–258. Paris: Dunod, 2006.
- [47] J. Biela and J. W. Kolar. "Using Transformer Parasitics for Resonant Converters - A Review of the Calculation of the Stray Capacitance of Transformers". In: *IEEE Transactions on Industry Applications* 44.1 (Jan. 2008), pp. 223–233.
- [48] TDK Electronics AG. *Product catalog: Ferrite materials*. URL: <https://www.tdk-electronics.tdk.com/en/529404/products/product-catalog/ferrites-and-accessories/ferrite-materials> (visited on 05/04/2022).
- [49] Magnetics. *MPP powder core*. C055926A2 datasheet. URL: <https://www.mag-inc.com/Media/Magnetics/Datasheets/C055926A2.pdf> (visited on 05/04/2022).
- [50] Magnetics. *High Flux powder core*. C058928A2 datasheet. URL: <https://www.mag-inc.com/Media/Magnetics/Datasheets/C058928A2.pdf> (visited on 05/04/2022).
- [51] Magnetics. *XFlux powder core*. 0078930A7 datasheet. URL: <https://www.mag-inc.com/Media/Magnetics/Datasheets/0078930A7.pdf> (visited on 05/04/2022).
- [52] Rectron Semiconductor. *High Voltage Fast Recovery Rectifier*. R5000F datasheet. URL: https://www.rectron.com/data_sheets/r2500f-r5000f.pdf (visited on 05/04/2022).
- [53] Dean Technology. *HVEF Diode Series*. HVEF12P datasheet. URL: https://assets.deantechnology.com/resources/31265/attachments/original/D-HVEF_Series_REV_1.0.pdf?1645986350 (visited on 05/04/2022).
- [54] L. Wang. "Medium Voltage Medium Frequency Isolated DC-DC Converter Based on 15 kV SiC MOSFETs". PhD thesis. North Carolina State University, 2017.

- [55] J. Wang et al. “Characterization, Modeling, and Application of 10-kV SiC MOSFET”. In: *IEEE Transactions on Electron Devices* 55.8 (Aug. 2008), pp. 1798–1806.
- [56] L. Pniak et al. “Ultrahigh-Voltage Switch for Bidirectional DC–DC Converter Driving Dielectric Elastomer Actuator”. In: *IEEE Transactions on Power Electronics* 35.12 (Dec. 2020), pp. 13172–13181.
- [57] adh30 for Wikipedia. *Wiggers Diagram*. Licensed under CC BY-SA 4.0. July 2016.

Raphaël Mottet
Lutry, Switzerland
raphael.mottet@proton.me

Education

- | | |
|-------------|---|
| 2018 - 2022 | Ph.D. in Robotics, Control and Intelligent Systems
<i>Integrated Actuators Laboratory, EPFL, Switzerland</i> |
| 2016 - 2017 | Master thesis: "Study and optimization of a linear drive system"
<i>Akribis Systems, Shanghai, China</i> |
| 2014 - 2017 | Master of Science in Robotics and Autonomous Systems
<i>École Polytechnique Fédérale de Lausanne, Switzerland</i> |
| 2013 - 2014 | Exchange student in the department of Electrical Engineering
<i>Polytechnique Montréal, Canada</i> |
| 2010 - 2014 | Bachelor of Science in Microengineering
<i>École Polytechnique Fédérale de Lausanne, Switzerland</i> |

Publications

Journal Articles

R. Mottet, M. Almanza, L. Pniak, A. Boegli and Y. Perriard, "*Ultra-High-Voltage (7-kV) Bidirectional Flyback Converter Used to Drive Capacitive Actuators*," in IEEE Transactions on Industry Applications, vol. 57, no. 5, pp. 5145-5156, Sept.-Oct. 2021.

Conference Papers and Proceedings

A. Walter, **R. Mottet**, T. Martinez, J. Chavanne, Y. Civet, Y. Perriard, "Improved electrical behavior of dielectric elastomer actuators," 2022 25th International Conference on Electrical Machines and Systems (ICEMS), 2022, (*Under review*)

R. Mottet, A. Boegli and Y. Perriard, "An Analytical Model for the Prediction of the Maximum Output Voltage Reachable with an Ultra-high Voltage Flyback Converter Driving Capacitive Actuators," 2021 23rd European Conference on Power Electronics and Applications (EPE'21 ECCE Europe), 2021.

R. Mottet, A. Boegli and Y. Perriard, "Schmitt trigger-based control strategy for the discharge phase of an ultra-high-voltage bidirectional flyback," 2021 24th International Conference on Electrical Machines and Systems (ICEMS), 2021.

S. Konstantinidi, T. Martinez, **R. Mottet**, Y. Civet and Y. Perriard, "DEA Self-discharge Characterization for Low Duty Cycle Applications," 2021 24th International Conference on Electrical Machines and Systems (ICEMS), 2021.

R. Mottet, A. Boegli, and Y. Perriard. "Ultra-high voltage, compact and energy recovering electronics for dielectric elastomer actuators." In Proceedings of the 10th international conference on Electromechanically Active Polymer (EAP) transducers & artificial muscles (EuroEAP), 2021.

R. Mottet, A. Boegli and Y. Perriard, "Control Strategy for the Discharge Phase of an Ultra-High Voltage (>7kV) Bi-Directional Flyback Converter Driving Capacitive Actuators," 2020 23rd International Conference on Electrical Machines and Systems (ICEMS), 2020.

R. Mottet, M. Almanza, A. Boegli and Y. Perriard, "Critical Parasitic Elements of Coupled Inductors for Ultra-High Voltage Flyback Converters Used to Drive Capacitive Actuators," 2019 22nd International Conference on Electrical Machines and Systems (ICEMS), 2019.

R. Mottet, M. Almanza, A. Boegli, and Y. Perriard. "Towards an ultra-high voltage gain, compact, and energy recovering Flyback DC/DC Converter." In Proceedings of the 9th international conference on Electromechanically Active Polymer (EAP) transducers & artificial muscles (EuroEAP), 2019.

L. Pniak, M. Almanza, **R. Mottet**, Y. Civet, and Y. Perriard. "High voltage switch for compact bidirectional dc-dc converter driving dielectric electroactive polymer actuators." In Proceedings of the 9th international conference on Electromechanically Active Polymer (EAP) transducers & artificial muscles (EuroEAP), 2019.

R. Mottet, J. Chavanne, A. Boegli and Y. Perriard, "Electric Charge Transfer Between Cascading Dielectric Electroactive Polymer Actuators," 2018 21st International Conference on Electrical Machines and Systems (ICEMS), 2018.

S. Thomas, P. Peralta, **R. Mottet**, M. Lehmann, Y. Civet and Y. Perriard, "Analysis and Reduction of Time Response in Thermally Activated Shape Memory Alloys," 2018 21st International Conference on Electrical Machines and Systems (ICEMS), 2018.

Student Projects Supervised

2021 **High voltage power supply system for tethered drone - Part II**

Clément Bongini, Bachelor Project

2020 **High voltage power supply for tethered drones**

Shadi Naguib, Semester Project

2019 **Control of a micro-robot via infrared communication**

Marc Uran, Semester Project

2019 **Transcutaneous Wireless Power & Data Transfer for Medical Applications**

Xavier Bailly, Semester Project